CarbonTracker Documentation
CT2022 release

Originally published Feb 17, 2023
Revised, March 3, 2023

Andrew R. Jacobson[1,2], Kenneth N. Schuldt[1,2], Pieter Tans[3], Arlyn Andrews[2], John B. Miller[2], Tomohiro Oda[4,5,6], Sourish Basu[7,8], John Mund[1,2], Brad Weir[9,7], Lesley Ott[7], Tuula Aalto[10], James Brice Abshire[11], Ken Aikin[12], Shuji Aoki[13], Francesco Apadula[14], Sabrina Arnold[15], Bianca Baier[2], Jakub Bartyzel[16], Andreas Beyersdorf[17], Tobias Biermann[18], Sebastien C. Biraud[19], Harald Boenisch[20], Gordon Brailsford[21], Willi A. Brand[22], Gao Chen[23], Huilin Chen[24], Lukasz Chmura[16], Shane Clark[25], Aurelie Colomb[26], Roisin Commane[27], Sébastien Conil[28], Cédric Couret[29], Adam Cox[25], Paolo Cristofanelli[30], Emilio Cuevas[31], Roger Curcoll[32], Bruce Daube[27], Kenneth J. Davis[33], Stephan De Wekker[34], Julian Della Coletta[35], Marc Delmotte[36], Elizabeth DiGangi[37], Joshua P. DiGangi[23], Alcide Giorgio di Sarra[38], Ed Dlugokencky[2], James W. Elkins[2], Lukas Emmenegger[39], Shuangxi Fang[40], Marc L. Fischer[41], Grant Forster[42,43], Arnoud Frumau[44], Michal Galkowski[16], Luciana V. Gatti[45], Torsten Gehrlein[20], Christoph Gerbig[22], Francois Gheusi[46], Emanuel Gloor[47], Vanessa Gomez-Trueba[48,31], Daisuke Goto[49], Tim Griffis[50], Samuel Hammer[35], Chad Hanson[51], László Haszpra[52], Juha Hatakka[10], Martin Heimann[22], Michal Heliasz[18], Arjan Hensen[44], Ove Hermansen[53], Eric Hintsa[2], Jutta Holst[54], Viktor Ivakhov[55], Daniel A. Jaffe[56], Armin Jordan[22], Warren Joubert[57], Anna Karion[58], Stephan Randolph Kawa[11], Victor Kazan[36], Ralph F. Keeling[25], Petri Keronen[59], Tobias Kneuer[60], Pasi Kolari[59], Kateřina Komínková[61], Eric Kort[62], Elena Kozlova[63], Paul Krummel[64], Dagmar Kubistin[60], Casper Labuschagne[57], David H.Y. Lam[65], Xin Lan[1,2], Ray L. Langenfelds[64], Olivier Laurent[66], Tuomas Laurila[10], Thomas Lauvaux[67,33], Jost Lavric[22], Beverly E. Law[51], John Lee[68], Olivia S.M. Lee[65], Irene Lehner[18], Kari Lehtinen[10], Reimo Leppert[22], Ari Leskinen[69,70], Markus Leuenberger[71], Ingeborg Levin[35], Janne Levula[59], John Lin[72], Matthias Lindauer[60], Zoe Loh[64], Morgan Lopez[36], Ingrid T. Luijkx[73,74], Chris René Lunder[53], Toshinobu Machida[75], Ivan Mammarella[76], Giovanni Manca[77], Alistair Manning[78], Andrew Manning[43], Michal V. Marek[61], Melissa Yang Martin[23], Hidekazu Matsueda[79], Kathryn McKain[2], Harro Meijer[24], Frank Meinhardt[80], Lynne Merchant[25], N. Mihalopoulos[81], Natasha L. Miles[33], Charles E. Miller[82], Logan Mitchell[72], Meelis Mölder[54], Stephen Montzka[2], Fred Moore[2], Heiko Moossen[22], Eric Morgan[25], Josep-Anton Morgui[32], Shinji Morimoto[13], Jennifer Müller-Williams[60], J. William Munger[27], David Munro[2], Cathrine Lund Myhre[53], Shin-Ichiro Nakaoka[75], Jaroslaw Necki[16], Sally Newman[83], Sylvia Nichol[21], Yosuke Niwa[75], Florian Obersteiner[20], Simon O'Doherty[84], Bill Paplawsky[25], Jeff Peischl[1,12], Olli Peltola[59], Salvatore Piacentino[38], Jean-Marc Pichon[26], Penelope Pickers[43], Steve Piper[25], Joseph Pitt[84], Christian Plass-Dülmer[60], Stephen Matthew Platt[53], Steve Prinzivalli[37], Michel Ramonet[36], Ramon Ramos[31], Enrique Reyes-Sanchez[31], Scott J. Richardson[33], Haris Riris[11], Pedro P. Rivas[31], Thomas Ryerson[12], Kazuyuki Saito[85], Maryann Sargent[27],

Motoki Sasakawa[75], Bert Scheeren[24], Tanja Schuck[86], Marcus Schumacher[22], Thomas Seifert[22], Mahesh Kumar Sha[87], Paul Shepson[88], Michael Shook[23], Christopher D. Sloop[37], Paul Smith[89], Kieran Stanley[84], Martin Steinbacher[39], Britton Stephens[90], Colm Sweeney[2], Kirk Thoning[2], Helder Timas[91], Margaret Torn[41], Kjetil Tørseth[53], Pamela Trisolino[30], Jocelyn Turnbull[92,1], Pim van den Bulk[44], Danielle van Dinther[44], Alex Vermeulen[54], Brian Viner[93], Gabriela Vitkova[61], Stephen Walker[25], Andrew Watson[63], Steven C. Wofsy[27], Justin Worsey[63], Doug Worthy[94], Dickon Young[84], Sönke Zaehle[22], Andreas Zahn[20] and Miroslaw Zimnoch[16]

[1]*CIRES, University of Colorado, Boulder, Colorado, USA*
[2]*NOAA Global Monitoring Laboratory, Boulder, Colorado, USA*
[3]*Institute of Arctic and Alpine Research,University of Colorado, Boulder, Colorado, USA*
[4]*Earth from Space Institute, Universities Space Research Association, Washington, DC, USA*
[5]*Department of Atmospheric and Oceanic Science, University of Maryland, College Park, Maryland, USA*
[6]*Graduate School of Engineering, Osaka University, Suita, Osaka, Japan*
[7]*Global Modeling and Assimilation Office, NASA Goddard Space Flight Center, Greenbelt, Maryland, USA*
[8]*Earth System Science Interdisciplinary Center, University of Maryland, College Park, Maryland, USA*
[9]*Morgan State University, Baltimore, Maryland, USA*
[10]*Finnish Meteorological Institute, Climate System Research, Helsinki, Finland*
[11]*NASA Goddard Space Flight Center, Greenbelt, Maryland, USA*
[12]*NOAA Chemical Sciences Laboratory, Boulder, Colorado, USA*
[13]*Tohoku University, Sendai, Japan*
[14]*Ricerca sul Sistema Energetico RSE S.p.A., Milano, Italy*
[15]*Deutsches Zentrum für Luft- und Raumfahrt (DLR), Institut für Physik der Atmosphäre, Oberpfaffenhofen, Germany*
[16]*AGH University of Science and Technology, Krakow, Poland*
[17]*California State University, San Bernardino, California, USA*
[18]*Lund University, Centre for Environmental and Climate Science, Lund, Sweden*
[19]*ARM Carbon Project, Lawrence Berkeley National Laboratory, Berkeley, California, USA*
[20]*Institute for Meteorology and Climate Research (IMK), Karlsruhe Institute of Technology (KIT), Karlsruhe, Germany*
[21]*National Institute of Water and Atmospheric Research, Wellington, New Zealand*
[22]*Max Planck Institute for Biogeochemistry, Jena, Germany*
[23]*NASA Langley Research Center, Hampton, Virginia, USA*
[24]*Centre for Isotope Research, University of Groningen, Groningen, Netherlands*
[25]*Scripps Institution of Oceanography, University of California, La Jolla, California, USA*
[26]*Observatoire de Physique du Globe de Clermont Ferrand, Aubiere, France*
[27]*Harvard University, School of Engineering and Applied Sciences, Cambridge, Massachusetts, USA*
[28]*Agence Nationale pour la Gestion des Déchets Radioactifs, France*
[29]*Umweltbundesamt, Zugspitze, Germany*
[30]*Institute of Atmospheric Sciences and Climate (CNR-ISAC), Bologna, Italy*
[31]*Agencia Estatal Meteorologia, Santa Cruz de Tenerife, Spain*
[32]*Institut de Ciencia i Tecnologia Ambientals, Universitat Autonoma de Barcelona, Barcelona, Spain*
[33]*The Pennsylvania State University, Department of Meteorology and Atmospheric Science, University Park, Pennsylvania, USA*
[34]*University of Virginia, Charlottesville, Virginia, USA*
[35]*Universität Heidelberg, Institut für Umweltphysik, Heidelberg, Germany*
[36]*Laboratoire des Sciences du Climat et de l'Environnement, LSCE/IPSL, CEA-CNRS-UVSQ, Université Paris-Saclay, Gif-sur-Yvette, France*
[37]*Earth Networks, Inc., an AEM company, Germantown, Maryland, USA*
[38]*Italian National Agency for New Technologies, Energy and Sustainable Economic Development, UTMEA-TER*

Earth Observations and Analyses Laboratory, Rome, Italy
[39]*Empa, Swiss Federal Laboratories for Materials Science and Technology, Laboratory for Air Pollution/Environmental Technology, Dübendorf, Switzerland*
[40]*Meteorological Observation Centre, Chinese Meteorological Administration, Beijing, China*
[41]*Lawrence Berkeley National Laboratory, Berkeley, California, USA*
[42]*National Centre for Atmospheric Sciences, University of East Anglia, Norwich, Norfolk, United Kingdom*
[43]*Centre for Ocean and Atmospheric Sciences, University of East Anglia, Norfolk, United Kingdom*
[44]*Netherlands Organisation for Applied Scientific Research (TNO), Petten, The Netherlands*
[45]*National Institute for Space Research (INPE), Sao Paulo, Brazil*
[46]*Observatoire Midi-Pyrénées, Toulouse, France*
[47]*University of Leeds,School of Geography, Leeds, United Kingdom*
[48]*Air Liquide España, Madrid, Spain*
[49]*National Institute of Polar Research, Tokyo, Japan*
[50]*University of Minnesota,Department of Soil, Water, and Climate, St. Paul, Minnesota, USA*
[51]*Oregon State University, Corvallis, Oregon, USA*
[52]*Institute for Nuclear Research, Debrecen, Hungary*
[53]*NILU, Kjeller, Norway*
[54]*Lund University, Dept. Phys. Geography and Ecosystem Science, Lund, Sweden*
[55]*Voeikov Main Geophysical Observatory,Saint Petersburg, Russia*
[56]*University of Washington, Seattle, Washington, USA*
[57]*South African Weather Service, Cape Point, South Africa*
[58]*National Institute of Standards and Technology, Gaithersburg, Maryland, USA*
[59]*University of Helsinki, Helsinki, Finland*
[60]*Deutscher Wetterdienst, Hohenpeißenberg Meteorological Observatory, Hohenpeißenberg, Germany*
[61]*Global Change Research Institute of the Czech Academy of Sciences, Brno, Czech Republic*
[62]*University of Michigan, Ann Arbor, Michigan, USA*
[63]*University of Exeter, Centre for Environmental Data Analysis, Exeter, Devon, United Kingdom*
[64]*Commonwealth Scientific and Industrial Research Organisation, Environment, Aspendale, Victoria, Australia*
[65]*Hong Kong Observatory, Hong Kong, China*
[66]*ICOS Atmospheric Thematic Centre, Gif-sur-Yvette, France*
[67]*University of Reims Champagne-Ardenne, CNRS, Reims, France*
[68]*University of Maine, Orono, Maine, USA*
[69]*University of Eastern Finland, Department of Technical Physics, Kuopio, Finland*
[70]*Finnish Meteorological Institute, Kuopio, Finland*
[71]*Climate and Environmental Physics, University of Bern, Bern, Switzerland*
[72]*Department of Atmospheric Sciences, University of Utah, Salt Lake City, Utah, USA*
[73]*Wageningen University, Wageningen, Netherlands*
[74] *ICOS Carbon Portal, Lund University, Lund, Sweden*
[75]*National Instiute for Environmental Studies, Tsukuba, Japan*
[76]*Institute for Atmospheric and Earth System Research/Physics, Faculty of Sciences, University of Helsinki, Finland*
[77]*European Commission, Joint Research Centre, Ispra, Italy*
[78]*Met Office Exeter, Devon, United Kingdom*
[79]*Meteorological Research Institute, Tsukuba, Japan*
[80]*Umweltbundesamt, Oberried-Hofsgrund, Germany*
[81]*Environmental and Chemical Processes Laboratory, University of Crete, Crete, Greece*
[82]*Jet Propulsion Laboratory, California Institute of Technology, Pasadena California, USA*
[83]*California Institute of Technology, Pasadena, California, USA*
[84]*University of Bristol, Bristol, United Kingdom*
[85]*Japan Meteorological Agency, Tokyo, Japan*
[86]*Institute for Atmospheric and Environmental Sciences, University of Frankfurt, Frankfurt, Germany*
[87]*Royal Belgian Institute for Space Aeronomy, Brussels, Belgium*
[88]*Purdue University, West Lafayette, Indiana, USA*
[89]*Svartberget Field Research Station, Swedish University of Agricultural Sciences, Vindeln, Sweden*
[90]*National Center for Atmospheric Research, Boulder, Colorado, USA*

[91]*Instituto Nacional de Meteorologia e Geofisica, Cidade de Espargos, Ilha do Sal, República de Cabo Verde*
[92]*GNS Science,National Isotope Centre, Lower Hutt, New Zealand*
[93]*Savannah River National Laboratory, Aiken, South Carolina, USA*
[94]*Environment and Climate Change Canado, Ontario, Canada*

Contents

1 Introduction

The goal of the CarbonTracker program is to produce quantitative estimates of atmospheric carbon uptake and release at the Earth's surface that are consistent with observed patterns of CO_2 in the atmosphere. CarbonTracker is an *inverse* model of atmospheric CO_2, which means that it attempts to model atmospheric CO_2 measurements by adjusting inputs and removals of CO_2 at the Earth surface until they best agree with those observational constraints. CarbonTracker is updated on a approximately-annual basis. The current release, CT2022, provides results from 2000 through the end of 2020. A "near-real" time model product, CT-NRT, extends these results through 2022 and later.

1.1 A tool for science, and for policy

CarbonTracker is made possible by the long-term monitoring of atmospheric CO_2 conducted by many academic and governmental programs around the world (see Sec. 7). These data help improve our understanding of how the land and ocean are responding to Earth's changing climate. The uptake and release of CO_2 by these ecosystems is changing due to chemical and physical responses to increased atmospheric CO_2 concentrations, to human management of lands and oceans, and to changes in temperature, precipitation, and winds.

CarbonTracker is a completely open product. All results, including graphics and tabular data, may be freely used without restriction, although we do request the favor of appropriate acknowledgment (see Sec. 1.5 and https://gml.noaa.gov/ccgg/carbontracker/citation.php).

The unrestricted access to all CarbonTracker results means that anyone can scrutinize our work, suggest improvements, and profit from our efforts. We hope this scrutiny will help guide further development of our methods, and improve our ability to monitor, diagnose, and possibly predict the behavior of the global carbon cycle.

CarbonTracker also can be relevant for helping to inform carbon policy. Its ability to accurately quantify natural and anthropogenic emissions and uptake at regional scales is currently limited by a sparse observational network. With enough observations however, CarbonTracker and systems like it will be able to monitor regional emissions, including those from fossil fuel use. This will provide an independent check on emissions accounting, including estimates of fossil fuel use based on economic inventories. It can thus provide feedback to policies aimed at limiting greenhouse gas emissions. This independent evaluation of the effectiveness of carbon policy is the bottom line in any mitigation strategy. It has the added advantage of being a constraint provided by the atmosphere itself, where CO_2 levels matter most.

1.2 A community effort

CarbonTracker is intended to be a tool for the community, and we welcome feedback and collaboration from anyone interested. Our ability to accurately track carbon with more spatial and temporal detail is fundamentally dependent on our collective ability to make enough measurements to characterize variability present in the atmosphere. For example, estimates suggest that observations from tall communication towers (taller than 200m) can tell us about carbon uptake and emission over a radius of only several hundred kilometers. The map of observation sites (Fig. 14) shows how sparse the current network is. One way to join this effort is by contributing measurements to the GLOBALVIEW+ project. Regular air samples collected from the surface, towers or aircraft are needed. It would also be very fruitful to expand use of continuous measurements like the ones now being made on very tall (more than 200m) communications towers. Another way to join this effort is by volunteering flux estimates from your own work, to be run through CarbonTracker and assessed against atmospheric CO_2 measurements. We also encourage collaborations focused on use of the CarbonTracker model as a tool for scientific analysis. Please contact us if you would like to get involved and collaborate with us.

1.3 The role of other atmospheric species in constraining the atmospheric carbon budget

Many laboratories making high accuracy CO_2 observations also make many other measurements of the same air, typically other greenhouse gases such as methane (CH_4), nitrous oxide (N_2O), sulfur hexafluoride (SF_6), as well as carbon monoxide (CO) and isotopic ratios of CO_2 and CH_4. These measurements are usually made as mole fractions, for reasons explained here.

These trace gases are relevant for the study of climate change and interesting in their own right, but the additional measurements can also help in identifying sources and sinks of carbon or in understanding carbon cycle processes. For this reason, many air samples are now analyzed for a suite of halocompounds and hydrocarbons. Several of these species can be useful for monitoring air quality, but they can also help with better source apportionment of the greenhouse gases. In addition, the estimation of the source strengths of a number of pollutants could be greatly improved if we were able to quantify fossil fuel CO_2 emissions from air measurements for specified regions.

The best tracer for quantifying the component of atmospheric CO_2 that has been recently added to an air mass through the burning of fossil fuels is the decrease of the carbon-14 (^{14}C) content of CO_2. Cosmic rays produce ^{14}C, a radioactive form of carbon, in the higher regions of the atmosphere. It is present in the atmosphere and oceans and in all living organisms and their remains, but coal, oil, and natural gas contain no ^{14}C because it has long decayed away. Currently, $^{14}CO_2$ measurements are made on only a small subset of the air samples because of higher analysis costs. None of these other data and their relationships have been used directly in this release of CarbonTracker. We expect them to be incorporated gradually at later stages.

CarbonTracker is a NOAA contribution to the North American Carbon Program.

1.4 Updates

CarbonTracker is updated about once per year to include new data and model improvements. CT2022 provides results from 2000 through 2020. Previous versions of CarbonTracker and our CT-NRT (CarbonTracker Near-Real Time) releases are available at the CarbonTracker website.

Important revisions of our methods for CT2022 include the following:

- Use of ERA5 reanalysis, including increased vertical resolution,
- Extension through the end of 2020,
- Revision of fossil fuel emissions to include COVID pandemic effect,

- New land and wildfire priors,
- Cross-evaluation using withheld assimilation data, and
- Revised model-data mismatch errors on GLOBALVIEW+ measurements

1.5 Citation and usage policy

1.5.1 Usage Policy

CarbonTracker is an open product of NOAA's Global Monitoring Laboratory using data from the NOAA Global Modeling Laboratory greenhouse gas observational network and collaborating institutions. Results, including figures and tabular material found on the CarbonTracker website may be used for non-commercial purposes without restriction. We kindly ask you to acknowledge, cite, and/or reference CarbonTracker as described below.

1.5.2 Citing our results

- We ask that scientific work that relies heavily on CarbonTracker products is discussed with us before publication, to ensure proper representation of our work and co-authorship if appropriate.
- Please cite as Jacobson et al. [2023]
- The DOI for CT2022 and all its associated products and results is http://dx.doi.org/10.25925/z1gj-3254.
- Please use "CT2022" as the shorthand to refer to our product, not "CT". This identifies both the product and the release version. It is vital to identify the version of the product you are using.
- Note that the product is called "CarbonTracker" without a space character, not "Carbon Tracker".
- Please include our suggested acknowledgment text in your acknowledgments section.
- Boilerplate model description text provided upon request.

Example ...we compare our results to NOAA's CarbonTracker, version CT2022 [Jacobson et al., 2023]. In this work, CT2022 is ...

Acknowledgments CarbonTracker CT2022 results provided by NOAA GML, Boulder, Colorado, USA from the website at http://carbontracker.noaa.gov.

Reference Andrew R. Jacobson, Kenneth N. Schuldt, Pieter Tans, Arlyn Andrews, John B. Miller, Tomohiro Oda, Sourish Basu, John Mund, Brad Weir, Lesley Ott, Tuula Aalto, James Brice Abshire, Ken Aikin, Shuji Aoki, Francesco Apadula, Sabrina Arnold, Bianca Baier, Jakub Bartyzel, Andreas Beyersdorf, Tobias Biermann, Sebastien C. Biraud, Harald Boenisch, Gordon Brailsford, Willi A. Brand, Gao Chen, Huilin Chen, Lukasz Chmura, Shane Clark, Aurelie Colomb, Roisin Commane, Sbastien Conil, Cdric Couret, Adam Cox, Paolo Cristofanelli, Emilio Cuevas, Roger Curcoll, Bruce Daube, Kenneth J. Davis, Stephan De Wekker, Julian Della Coletta, Marc Delmotte, Elizabeth DiGangi, Joshua P. DiGangi, Alcide Giorgio di Sarra, Ed Dlugokencky, James W. Elkins, Lukas Emmenegger, Shuangxi Fang, Marc L. Fischer, Grant Forster, Arnoud Frumau, Michal Galkowski, Luciana V. Gatti, Torsten Gehrlein, Christoph Gerbig, Francois Gheusi, Emanuel Gloor, Vanessa Gomez-Trueba, Daisuke Goto, Tim Griffis, Samuel Hammer,

Chad Hanson, Lszl Haszpra, Juha Hatakka, Martin Heimann, Michal Heliasz, Arjan Hensen, Ove Hermansen, Eric Hintsa, Jutta Holst, Viktor Ivakhov, Daniel A. Jaffe, Armin Jordan, Warren Joubert, Anna Karion, Stephan Randolph Kawa, Victor Kazan, Ralph F. Keeling, Petri Keronen, Tobias Kneuer, Pasi Kolari, Kateina Komnkov, Eric Kort, Elena Kozlova, Paul Krummel, Dagmar Kubistin, Casper Labuschagne, David H.Y. Lam, Xin Lan, Ray L. Langenfelds, Olivier Laurent, Tuomas Laurila, Thomas Lauvaux, Jost Lavric, Beverly E. Law, John Lee, Olivia S.M. Lee, Irene Lehner, Kari Lehtinen, Reimo Leppert, Ari Leskinen, Markus Leuenberger, Ingeborg Levin, Janne Levula, John Lin, Matthias Lindauer, Zoe Loh, Morgan Lopez, Ingrid T. Luijkx, Chris Ren Lunder, Toshinobu Machida, Ivan Mammarella, Giovanni Manca, Alistair Manning, Andrew Manning, Michal V. Marek, Melissa Yang Martin, Hidekazu Matsueda, Kathryn McKain, Harro Meijer, Frank Meinhardt, Lynne Merchant, N. Mihalopoulos, Natasha L. Miles, Charles E. Miller, Logan Mitchell, Meelis Mlder, Stephen Montzka, Fred Moore, Heiko Moossen, Eric Morgan, Josep-Anton Morgui, Shinji Morimoto, Jennifer Mller-Williams, J. William Munger, David Munro, Cathrine Lund Myhre, Shin-Ichiro Nakaoka, Jaroslaw Necki, Sally Newman, Sylvia Nichol, Yosuke Niwa, Florian Obersteiner, Simon OĎoherty, Bill Paplawsky, Jeff Peischl, Olli Peltola, Salvatore Piacentino, Jean-Marc Pichon, Penelope Pickers, Steve Piper, Joseph Pitt, Christian Plass-Dlmer, Stephen Matthew Platt, Steve Prinzivalli, Michel Ramonet, Ramon Ramos, Enrique Reyes-Sanchez, Scott J. Richardson, Haris Riris, Pedro P. Rivas, Thomas Ryerson, Kazuyuki Saito, Maryann Sargent, Motoki Sasakawa, Bert Scheeren, Tanja Schuck, Marcus Schumacher, Thomas Seifert, Mahesh Kumar Sha, Paul Shepson, Michael Shook, Christopher D. Sloop, Paul Smith, Kieran Stanley, Martin Steinbacher, Britton Stephens, Colm Sweeney, Kirk Thoning, Helder Timas, Margaret Torn, Kjetil Trseth, Pamela Trisolino, Jocelyn Turnbull, Pim van den Bulk, Danielle van Dinther, Alex Vermeulen, Brian Viner, Gabriela Vitkova, Stephen Walker, Andrew Watson, Steven C. Wofsy, Justin Worsey, Doug Worthy, Dickon Young, Snke Zaehle, Andreas Zahn, Miroslaw Zimnoch. CarbonTracker CT2022, 2023.DOI: 10.25925/z1gj-3254

Acknowledgment text "CarbonTracker CT2022 results provided by NOAA GML, Boulder, Colorado, USA from the website at http://carbontracker.noaa.gov."

Suggested Website Citation "CarbonTracker CT2022, http://carbontracker.noaa.gov"

2 Terrestrial biosphere module

The biospheric component of the terrestrial carbon cycle consists of all the carbon stored in 'biomass' around us. This includes trees, shrubs, grasses, carbon within soils, dead wood, and leaf litter. Such reservoirs of carbon can exchange CO_2 with the atmosphere. Exchange starts when plants take up CO_2 during their growing season through the process of photosynthesis. Most of this carbon is released back to the atmosphere throughout the year through the process of respiration. This process includes both the decay of dead wood and litter and the metabolic respiration of living plants. Of course, plants can also return carbon to the atmosphere when they burn, as described in Section 3. Even though the yearly sum of uptake and release of carbon amounts to a relatively small number, a few petagrams (one Pg=10^{15} g)) of carbon per year), the flow of carbon each way is as large as 120 Pg C each year. This is why the net result of these flows needs to be monitored in a system such as ours. It is also the reason we need a good physical description–a model–of these flows of carbon. After all, from the atmospheric measurements of CO_2 we can see only the relatively small net sum of the much larger two-way streams, or gross fluxes. Information on what the biospheric fluxes are doing in each season, and in every location on Earth is derived from specialized biosphere models, and fed into our system as a first guess, to be refined by our assimilation procedure.

2.1 CASA model

Two biosphere models currently provide first-guess terrestrial fluxes for CT2022. Both models are versions of the Carnegie-Ames Stanford Approach (CASA) biogeochemical model introduced by Potter et al. [1993]. CASA calculates global carbon fluxes using input from weather models to drive biophysical processes, and satellite observed Normalized Difference Vegetation Index (NDVI) to track plant phenology. The models are driven by year-specific weather and satellite observations, and include the effects of fires on photosynthesis and respiration [van der Werf et al., 2003, 2006; Giglio et al., 2006]. Both simulations provide $0.5^\circ \times 0.5^\circ$ global fluxes with a monthly time resolution.

CASA models directly simulate monthly-mean Net Primary Production (NPP) and heteotrophic respiration (R_H) for each terrestrial grid cell being simulated. NPP is the difference in photosynthetic carbon uptake (Gross Primary Production, GPP) and the carbon release by the same plants due to "maintenance respiration", which is also called autotrophic respiration, R_A. The carbon uptake represented by NPP and carbon release represented by R_H can be differenced to provide Net Ecosystem Exchange (NEE) of CO_2. Throughout this discussion, we use the convention that fluxes carry algebraic signs and we adopt the "atmospheric perspective" for those signs. Thus carbon uptake by the terrestrial biosphere is a negative flux to the atmosphere, and release of CO_2 back to the atmosphere is a positive flux. This means that we represent all respiration fluxes as positive and GPP as negative, so NEE $=$ NPP $+ R_H$. This stands in contrast to convention in the terrestrial carbon community, where all fluxes are generally non-negative.

2.2 Temporal downscaling

Use of monthly-mean terrestrial fluxes to simulate atmospheric CO_2 is not sufficient to resolve the variability observed at measurement sites. Instead, higher-frequency variations, including the diurnal cycle and effects of passing weather systems must be imposed on the CASA monthly fluxes. Following the logic laid out by Olsen and Randerson [2004], we transform the CASA-supplied monthly-mean NPP and R_H fluxes into GPP and total ecosystem respiration, $R_E = R_A + R_H$.

To estimate sub-monthly variations, including diurnal and synoptic variability, the Olsen and Randerson [2004] strategy is to model GPP as a linear function of incoming surface solar radiation and total ecosystem respiration as a function of near-surface temperature.

The fundamental assumption needed to apply this scheme is that we can resolve CASA-simulated NPP into GPP and R_A. We apply the assumption that GPP is twice NPP, which further implies that R_A is the same size as NPP (but of opposite sign):

$$\text{GPP} = 2 * \text{NPP}, \tag{1}$$

$$\text{NPP} = \text{GPP} + R_A, \tag{2}$$

and

$$R_A = -1 * \text{NPP}. \tag{3}$$

We use meteorological fields from the European Centre for Medium-Range Weather Forecasts (ECMWF) ERA5 reanalysis to supply temperature and shortwave radiation. Fluxes are generated with 90-minute variability using a simple temperature Q_{10} relationship for respiration, assuming a global Q_{10} value of 1.5, and a linear scaling of photosynthesis with solar radiation. The procedure is very similar, but **NOT** identical to the procedure in Olsen and Randerson [2004]. Note that the introduction of 90-minute variability conserves the monthly mean NEE from the CASA model. Instantaneous NEE for each 90-minute interval is created as:

$$\text{NEE}(t) = \text{GPP}(t) + R_E(t), \tag{4}$$

where

$$\text{GPP}(t) = \text{GPP}_{\text{mean}}(I(t)/I_{\text{mean}}) \tag{5}$$

$$R_E(t) = R_{E,\text{mean}}(Q_{10}(t)/Q_{10,\text{mean}}), \tag{6}$$

and Q_{10} is computed as

$$Q_{10}(t) = 1.5^{(T_{2m}(t)-273.15)/10.0}, \tag{7}$$

where T_{2m} is temperature at 2 meters above the land surface in Kelvin, I is surface incoming solar radiation, t is time in 90-minute intervals, and x_{mean} represents the monthly mean of quantity x, including the monthly-mean fluxes derived from the CASA model.

2.2.1 Smooth month-to-month variations

While the scheme outlined above imposes realistic diurnal- and synoptic-scale variations on monthly-mean GPP and R_E, it still allows for abrupt changes from one month to the next. For CT2022, we add a further processing step designed to remove such unrealistic step changes. We fit smooth curves to the monthly GPP and R_E using the piecewise integral quadratic splines (PIQS) of Rasmussen [1991]. These PIQS fits are continuous in the first and second derivatives, and have the property of preserving monthly mean flux. We use a similar scheme to smooth over year-to-year step changes in fossil fuel emissions. The final smoothed GPP is

$$\text{GPP}_F(t) = \text{GPP}(t) - \text{GPP}_{\text{mean}} + \text{GPP}_{\text{PIQS}}(t), \tag{8}$$

and the final smoothed ecosystem respiration is

$$R_{E,F}(t) = R_E(t) - R_{E,\text{mean}} + R_{E,\text{PIQS}}(t). \tag{9}$$

Together, these form the terrestrial NEE imposed as a first-guess flux in CT2022:

$$\text{NEE}_F(t) = \text{GPP}_F(t) + R_{E,F}(t). \tag{10}$$

2.3 GFED4.1s and GFED_CMS

CarbonTracker uses fluxes from CASA runs from two models associated with the GFED project as its first guess for terrestrial biosphere fluxes. We have found a significantly better match to observations when using this output compared to the fluxes from a neutral biosphere simulation. Both of the CASA simulations used in CT2022 (GFED 4.1s and GFED_CMS) are driven by AVHRR NDVI. This satellite driver tends to produce a larger-amplitude annual cycle of NEE compared to the alternative driver, MODIS fPAR. As one of the robust results of atmospheric inversions is a deeper annual cycle of terrestrial NEE, inversions using NDVI-driven first-guess fluxes perform slightly better than those with a MODIS fPAR driver.

The record of atmospheric CO_2 calls for a deeper terrestrial biosphere sink than that generally simulated by terrestrial biosphere models like CASA. Inverse models manifesting such a sink generally simulate a larger annual cycle of terrestrial biosphere fluxes, and in particular a deeper boreal summer uptake of carbon dioxide, in the posterior optimized fluxes compared to the prior models (See Fig. 2). We call upon the

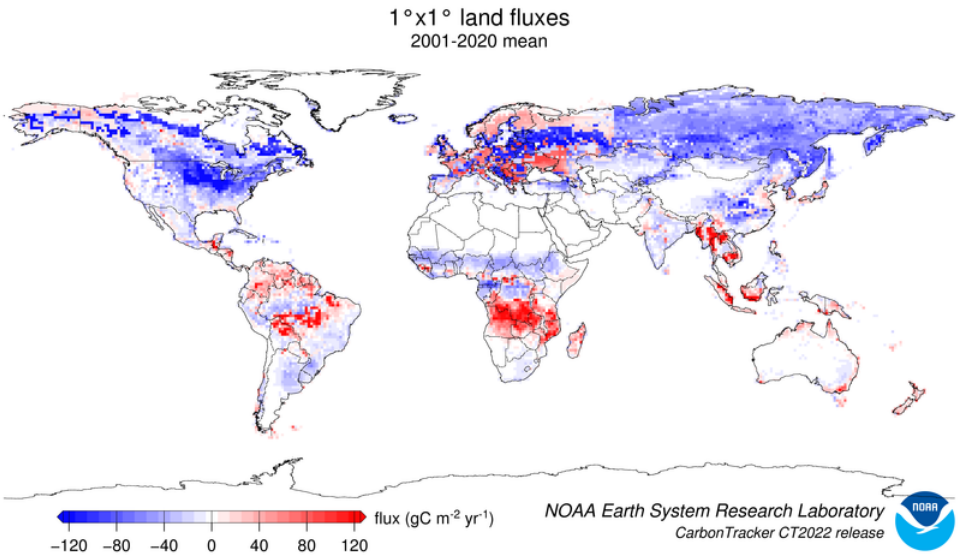

Figure 1: Map of optimized global biosphere fluxes. The pattern of net ecosystem exchange (NEE) of CO_2 of the land biosphere averaged over the time period indicated, as estimated by CarbonTracker. This NEE represents land-to-atmosphere carbon exchange from photosynthesis and respiration in terrestrial ecosystems, and a contribution from fires. It does not include fossil fuel emissions. Negative fluxes (blue colors) represent CO_2 uptake by the land biosphere, whereas positive fluxes (red colors) indicate regions in which the land biosphere is a net source of CO_2 to the atmosphere. Units are g C m^{-2} yr^{-1}.

atmospheric CO_2 observations to make this change, and in order to handle these prior model differences the ensemble Kalman filter's prior covariance model has to be appropriately tuned. In short, this prior uncertainty needs to comfortably span differences among the terrestrial biosphere priors, the fossil fuel emissions estimates, and adjustments to fluxes required to bring model predictions into agreement with observations. CT2022 prior covariances have been adjusted compared to prior releases, and details on this adjustment can be found in Section 8.

CarbonTracker CT2022 is a full reanalysis of the 2000-20w0 period using new fossil fuel emissions, CASA-GFED v4.1s and GFED_CMS fire emissions, and first-guess biosphere model fluxes derived from CASA-GFED v4.1s for the first of our inversions, and from CASA GFED_CMS for the second inversion.

Due to the inclusion of fires, inter-annual variability in weather and NDVI, the fluxes for North America start with a small net flux even before optimizing the fluxes. This first-guess flux ranges from neutral exchange to about 0.5 Pg C yr^{-1} of uptake.

3 Fire module

Vegetation fires are an important part of the carbon cycle and have been so for many millennia. Even before human civilization began to use fires to clear land for agricultural purposes, most ecosystems were subject to natural wildfires that would rejuvenate old forests and bring important minerals to the soils. When fires consume part of the landscape in either controlled or natural burning, carbon dioxide (among many other gases and aerosols) is released in large quantities. Each year, vegetation fires emit around 2 Pg C as CO_2 into the atmosphere, mostly in the tropics. Currently, a large fraction of wildfire is started by humans. This is mostly intentional to clear land for agriculture, or to re-fertilize soils before a new growing season. This important component of the carbon cycle is monitored mostly from space, while sophisticated 'biomass

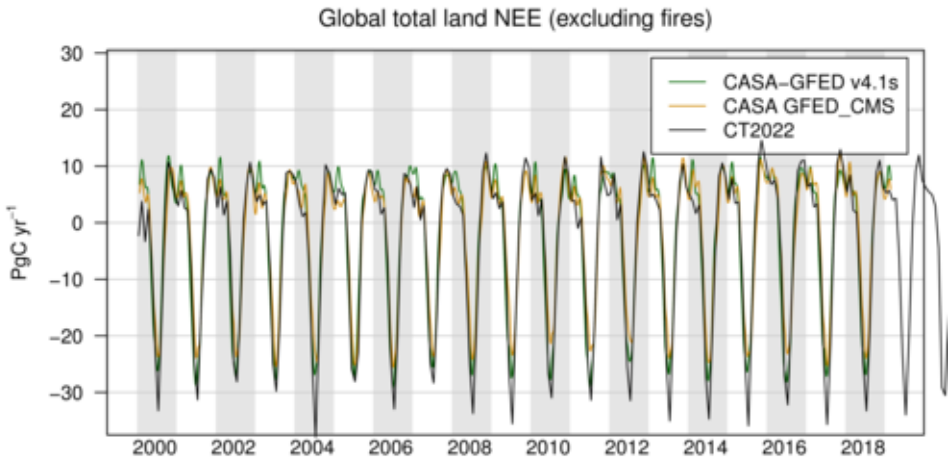

Figure 2: Time series of global-total terrestrial biosphere flux between the two priors and the CT2022 posterior. Global CO_2 uptake by the land biosphere, expressed in Pg C yr^{-1}, excluding emissions by wildfire. Positive flux represents emission of CO_2 to the atmosphere, and the negative fluxes indicate times when the land biosphere is a sink of CO_2. Optimization against atmospheric CO_2 data requires a larger land sink than in either prior, which effectively requires a deeper annual cycle. This is shown by the CT2022 posterior (black).

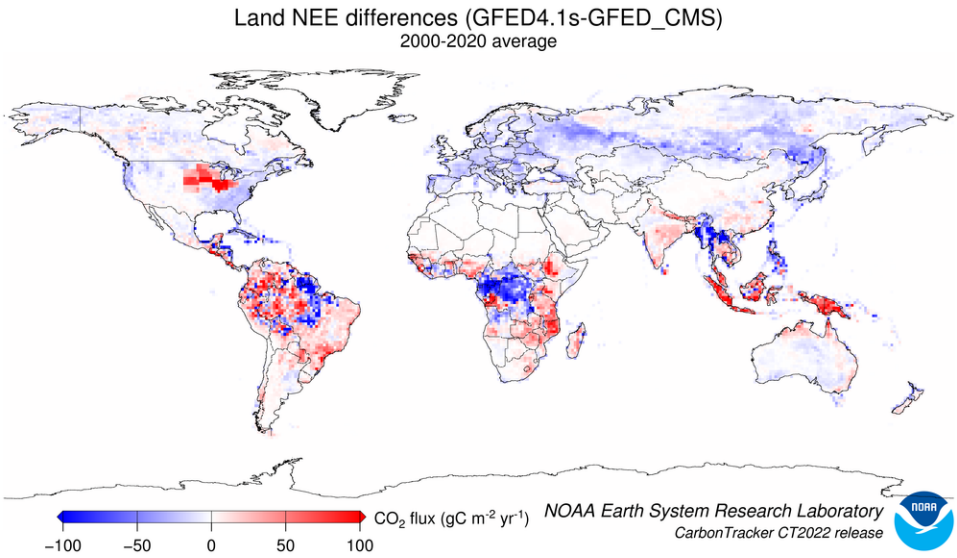

Figure 3: Differences in long-term mean terrestrial biosphere fluxes between the two priors. Red indicates areas where the GFED4.1s prior has less terrestrial uptake (or more outgassing to the atmosphere) than the GFED_CMS prior, and blue represents the opposite. Units are g C m^{-2} yr^{-1}.

burning' models are used to estimate the amount of CO_2 emitted by each fire. Such estimates are then used in CarbonTracker to prescribe the emissions. These emissions are not modified in the optimization (inverse modeling) process.

In CT2022 we use two fire emissions datasets, each with at least daily temporal resolution. The GFED4.1s emissions are modeled at 3-hourly intervals, and GFED_CMS emissions are available at daily resolution.

3.1 Global Fire Emissions Database (GFED)

CT2022 uses GFED4.1s [Giglio et al., 2013; van der Werf et al., 2017] as one of the fire modules to estimate biomass burning. GFED4.1s is a variant of the CASA biogeochemical model as described in the terrestrial biosphere model documentation to estimate the carbon fuel in various biomass pools. The dataset consists of $1^\circ \times 1^\circ$ gridded monthly burned area, fuel loads, combustion completeness, and fire emissions (Carbon, CO_2, CO, CH_4, NMHC, H_2, NO_x, N_2O, PM2.5, Total Particulate Matter, Total Carbon, Organic Carbon, Black Carbon) for the time period spanning January 1997 - December 2021, of which we currently only use CO_2.

The GFED burned area is based on MODIS satellite observations of fire counts. These, together with detailed vegetation cover information and a set of vegetation specific scaling factors, allow predictions of burned area over the time span that active fire counts from MODIS are available. The relationship between fire counts and burned area is derived, for the specific vegetation types, from a 'calibration' subset of 500m resolution burned area from MODIS in the period 2001-2004.

Once burned area has been estimated globally, emissions of trace gases are calculated using the CASA biosphere model. The seasonally changing vegetation and soil biomass stocks in the CASA model are combusted based on the burned area estimate, and converted to atmospheric trace gases using estimates of fuel loads, combustion completeness, and burning efficiency.

For CT2022, we also apply temporal scaling factors updated from Mu et al. [2011] to downscale the GFED4.1s CO_2 emissions from monthly averages to emissions with 3-hourly resolution.

3.2 GFED_CMS: Fluxes from the NASA Carbon Monitoring System

The NASA GFED_CMS team uses a variant of the GFED4 system to produce alternative fire emissions. This model uses GIMSS NDVI, the GFEDv3 fire model and GFEDv4 burned area. Fire emissions are available on a daily basis from 2003-2017. For 2000-2002, and for 2018-2020, we apply the climatology of GFED_CMS fire emissions, computed from its 2003-2017 mean.

Note that the GFED_CMS team produces temporally-downscaled GPP, heterotrophic respiration, and fires with 3-hourly resolution. This is done using MERRA meteorology using a scheme similar to Olsen and Randerson [2004]. We do not use this downscaled product, in part because the MERRA meteorology is different from the ECMWF meteorology, and in part because the spatial resolution of the MERRA meteorology is different from our $1^\circ \times 1^\circ$ flux grid. This means that we are limited to daily resolution of GFED_CMS fire emissions: unlike the GFED4.1s fire emissions, these have no diurnal cycle.

4 Fossil fuel module

Human beings first influenced the carbon cycle through land-use change. Early humans used fire to control animals and later cleared forests for agriculture. Over the last two centuries, following the industrial and technical revolutions and continuing global population increase, fossil fuel combustion has become the largest anthropogenic source of CO_2. Coal, oil and natural gas combustion are the most common energy sources in both developed and developing countries. Global cement production is also significant,

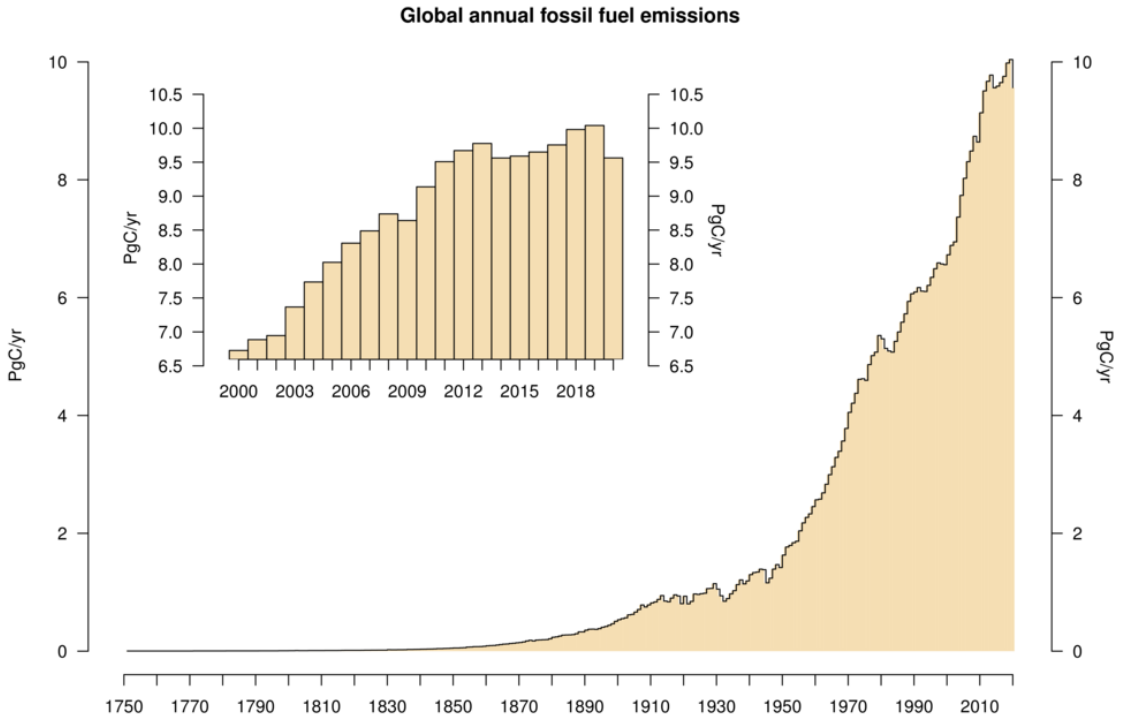

Figure 4: Time series of annual global fossil fuel emissions, in units of Pg C yr^{-1} (billion metric tons of C per year). Values from 1751 to 2014 are from Boden et al. [2017], and later values are extrapolated using consumption growth rate data of British Petroleum [2019]. Inset figure shows the CT2022 period of analysis, 2000-2020.

contributing about 5% of total fossil CO_2 emissions. Important sectors of the economy–power generation, transportation, residential & commercial building heating, and industrial processes–rely on fossil fuels. The continued growth of fossil fuel combustion has led to a steady increase of global CO_2 emissions to the atmosphere (Fig. 4). According to Boden et al. [2017], global emissions of CO_2 from fossil fuel burning, cement manufacturing, and flaring reached 5 billion metric tons of carbon per year (Pg C yr^{-1}) in the decade of the 1970s. Updated emissions products indicate that global total emissions exceeded 10 Pg C yr^{-1} for the first time in 2018. One petagram of carbon, Pg C, is equal to 10^{15} grams of carbon, or one billion metric tons of carbon. To convert to mass of CO_2 emitted, one would multiply by the factor $\frac{44}{12}$, representing the molecular weight of CO_2 compared to the atomic weight of carbon.

U.S. input of CO_2 to the atmosphere from fossil fuel burning in 2020 was 1.3 Pg C, representing 13% of the global total. North American emissions remained nearly constant from 2000-2018, and decreased slightly during the 2020 COVID pandemic year. On the other hand, emissions from developing economies such as the People's Republic of China have been increasing. Emissions from China in 2020 were 2.8 Pg C yr^{-1}, representing 30% of the global total.

In almost all global and regional carbon flux estimation systems, including CarbonTracker, fossil fuel CO_2 emissions are not optimized. Instead, these emissions are imposed and are not subject to revision by the inverse modeling framework. Global mass balance requires that any errors in fossil fuel emissions be compensated by opposing errors in land and ocean CO_2 exchange. Thus it is vital that fossil fuel CO_2 emissions are prescribed accurately, so that flux estimates for the land biosphere and oceans are robust. The fossil fuel emissions source data we use are available on an annually-integrated global and national basis. This aggregate information needs to be gridded before being incorporated into CarbonTracker. The major uncertainty in this process is distributing the national-annual emissions spatially across a nation and

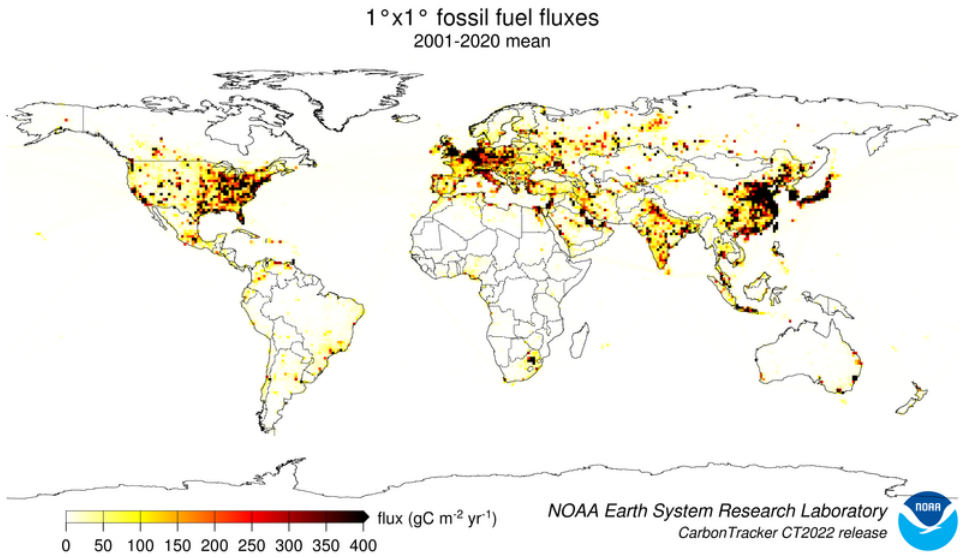

Figure 5: Spatial distribution of fossil fuel emissions. This is a spatial average of the Miller and ODIAC emissions inventories.

temporally into hourly contributions. In CT2022, two different fossil fuel CO_2 emissions datasets were used to help assess the uncertainty in this mapping process. These two emissions products are called the "Miller" and "ODIAC" emissions datasets. These two datasets have very similar global and national emissions for each year, but differ in how those emissions are distributed spatially and temporally.

Whereas early CarbonTracker releases used monthly-constant fossil fuel emissions, starting with CT2015 we introduced the use of temporal scaling factors to simulate day-of-week and diurnal variability for those emissions. These "Temporal Improvements for Modeling Emissions by Scaling" (TIMES) scaling factors, introduced by Nassar et al. [2013], are again applied to both the Miller and ODIAC emissions modules for CT2022. The scaling factors consist of seven day-of-week global scaling factor maps, and 24 hourly global scaling factor maps to represent the diurnal cycle. For use in TM5, the hourly scaling factors were aggregated to three-hourly factors to accommodate the time step of the model.

4.1 The "Miller" emissions dataset

- **Global and National Totals** The Miller fossil fuel emission inventory is derived from independent global total and spatially-resolved inventories. Annual global total fossil fuel CO_2 emissions are based on the Appalachian Engergy Centers CDIAC at AppState project (https://energy.appstate.edu/research/work-areas/cdiac-appstate), which is an effort to update the original annual global and country fossil fuel-CO_2 emissions estimates from the DOEs Carbon Dioxide Information and Analysis Center (CDIAC) [Boden et al., 2017]. The CDIAC at AppState emissions estimates used in CT2022 extend through 2017.

  In order to estimate these fluxes through April 2022 (the months in 2022 needed for our 12-week assimilation window), we extrapolate the CDIAC at AppState estimates using the fractional increases from other fossil fuel emissions products: 1) The BP (formerly British Petroleum) Statistical Review of World Energy [BP, 2021], and 2) The near-real-time CarbonMonitor product https://carbonmonitor.org/, accessed Dec. 6, 2022. To calculate emissions for 2018 and 2019, annual fractional emissions increases (by country and fuel type: coal, oil, and gas) are derived from BP data and applied to CDIAC at AppState data for 2017. For 2020 through mid-2022 emissions, fractional increases are applied to 2019 emissions estimates on a per-country and monthly basis. For example, to calculate July 2000

emissions for France, the ratio of July 2020 to July 2019 emissions for France are used to scale July 2019 emissions. No fuel-type data is available from CarbonMonitor, so the same year-on-year fractional changes are applied to all fuel types.

- **Spatial Distribution** Miller fossil-fuel CO_2 fluxes are spatially distributed in two steps: First, the coarse-scale country totals through 2017 from CDIAC at AppState are mapped onto a $1^\circ \times 1^\circ$ grid according to the spatial patterns from the EDGAR v5.0 inventories [Commission et al., 2019]. The spatial pattern varies by year up until the end of the EDGAR v5.0 product in 2018. After this, the trends estimated in each pixel are linearly extrapolated. Note that while EDGAR provides annual emissions estimates at $1^\circ \times 1^\circ$ resolution, their totals do not agree with those from CDIAC at AppState. Thus, only the spatial patterns in EDGAR are used. The CDIAC country-by-country totals sum to about 95% of the global total emissions; the remaining 5% is mapped to global shipping routes according to EDGAR, which we treat as a proxy for bunker fuel emissions.
- **Temporal Distribution** For North America between 30 and 60°N, the Miller system imposes a seasonal cycle derived from the first and second harmonics [Thoning et al., 1989] of the Blasing et al. [2004] analysis for the United States. The Blasing analysis has ˜10% higher emissions in winter than in summer. This scheme defines a fixed fraction of emissions for each month, so while the shape of the annual cycle is invariant, the amplitude of that cycle scales with the annual total emissions. For Eurasia, a set of seasonal emissions factors from EDGAR distributed by emissions sector is used to define fossil fuel seasonality. As in North America, this seasonality is imposed only from 30-60°N. The Eurasian seasonal amplitude is about 25%, significantly larger than that in North America, owing to the absence of a secondary summertime maximum due to air conditioning. See Figure 6 for the resulting time series of fossil fuel emissions. In order to avoid discontinuities in the fossil fuel emissions between consecutive years, a spline curve that conserves annual totals [Rasmussen, 1991] is fit to seasonal emissions in each $1^\circ \times 1^\circ$ grid cell.

4.2 The "ODIAC" emissions dataset

- **Global Totals** We use the ODIAC2020 fossil fuel emission inventory [Oda et al., 2018; Oda and Maksyutov, 2011, 2015] as one of our fossil fuel emissions estimates. This version was prepared for use in the OCO-2 v10 MIP [Basu and Nassar, 2021; Byrne et al., 2022] and includes a 2020 anomaly derived from the Carbon Monitor emissions project (https://carbonmonitor.org/). ODIAC is also derived from independent global and country emission estimates from CDIAC, but national emission estimates used were taken from [Gilfillan and Marland, 2021]. Differences between the Gilfillan and Marland [2021] global total and country-by-country totals were ascribed to the entire emissions field. Annual country total fossil fuel CO_2 emissions for 2018-2019 were extrapolated using the BP Statistical Review of World Energy [British Petroleum, 2019], and those for 2020 used the Carbon Monitor results as described in Byrne et al. [2022].
- **Spatial Distribution** ODIAC emissions are spatially distributed using many available "proxy data" that explain spatial extent of emissions according to emission types (emissions over land, gas flaring, aviation and marine bunker). Emissions over land were distributed in two steps: First, emissions attributable to power plants were mapped using geographical locations (latitude and longitude) provided by the global power plant dataset CARbon Monitoring and Action, CARMA. Next, the remaining land emissions (*i.e.* land total minus power plant emissions) were distributed using nightlight imagery collected by U.S. Air Force Defense Meteorological Satellite Project (DMSP) satellites. Emissions from gas flaring were also mapped using nightlight imagery. Emissions from aviation were mapped using flight tracks adopted from UK AERO2k air emission inventory. It should be noted that currently, air traffic emissions are emitted at ground level within CarbonTracker. Emissions from marine bunker fuels are placed entirely in the ocean basins along shipping routes according to patterns from the

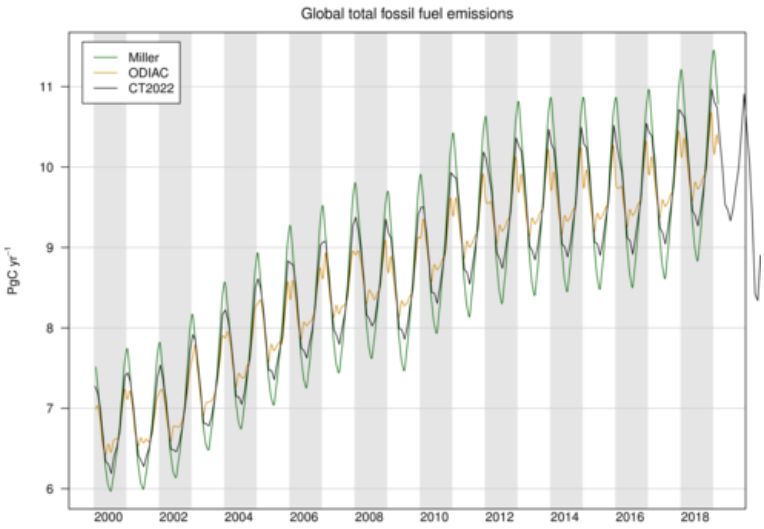

Figure 6: Time series of global fossil fuel emissions showing annual cycles. The Miller (green) and ODIAC (tan) estimates are each used by half of the sixteen inversions in the CT2022 suite, so the CT2022 (black) inventory is effectively an average of Miller and ODIAC. Note that fossil fuel emissions are not optimized in CarbonTracker.

EDGAR database.

- **Temporal Distribution** The CDIAC estimates used for mapping emissions in ODIAC only describe how much CO_2 was emitted in a given year. To present seasonal changes in emissions, we used the CDIAC $1^\circ \times 1^\circ$ monthly fossil fuel emission inventory [Andres et al., 2011]. The CDIAC monthly data utilizes the top 20 emitting countries' fuel (coal, oil and gas) consumption statistics available to estimate seasonal change in emissions. Monthly emission numbers at each pixel were divided by annual total and then a fraction to annual total was obtained. Monthly emissions in the ODIAC inventory were derived by multiplying this fraction by the emission in each grid cell.

4.3 Uncertainties

Marland [2008] attached an uncertainty of about 5% (95% confidence interval; approximately 2-σ) to the global total fossil fuel source. Estimates by Andres et al. [2014] put a larger uncertainty of 8.4% (2-σ) on the CDIAC global total. Uncertainties for individual regions of the world, and for sub-annual time periods are likely to be larger. Additional uncertainties are introduced when the emissions are distributed in space and time. In the Miller dataset, the overall Eurasian seasonality is based on scaling factors derived only from Western Europe and thus highly uncertain, but most likely a better representation than assuming no emission seasonality at all. Similarly, the use of the CDIAC monthly emission dataset for modeling seasonality introduces additional uncertainty in ODIAC. The additional uncertainty for the global total in the monthly CDIAC emission, which is solely due to the method for estimating seasonality, is reported as 6.4% [Andres et al., 2011]. As mentioned earlier, fossil fuel emissions are not optimized in the current CarbonTracker system, similar to nearly all carbon data analysis systems. Spatial and temporal atmospheric CO_2 gradients arise from terrestrial biosphere and fossil-fuel sources. These gradients, which are interpreted by CarbonTracker, are difficult to attribute to one or the other cause. This is because atmospheric sampling sites have historically been established in locations remote from biospheric and anthropogenic sources, especially in the temperate Northern Hemisphere. Given that surface CO_2 flux due to biospheric activity and oceanic exchange is much more uncertain compared to fossil fuel emissions, CarbonTracker, like most

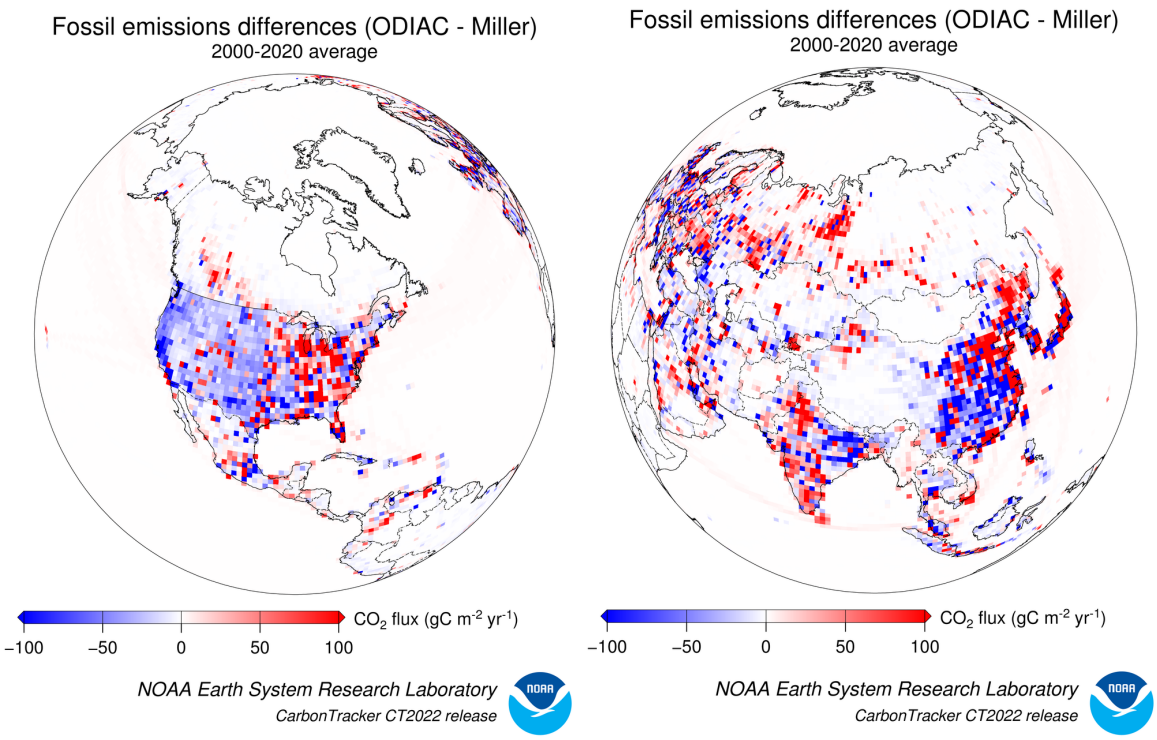

Figure 7: Spatial differences in long-term mean fossil fuel emissions between the two priors. Note that both the Miller and ODIAC emissions inventories use the same country totals, but have different models for spatial distribution of that flux within countries.

current carbon dioxide data assimilation systems, does not attempt to optimize fossil fuel emissions. That is, the contribution of CO_2 from fossil fuel burning to observed CO_2 mole fractions is considered known. As detailed above, however, in CarbonTracker an effort is made to account for some aspects of fossil fuel uncertainty by using two different fossil fuel estimates. From a technical point of view, extra land biosphere prior flux uncertainty is included in the system to represent the random errors in fossil fuel emissions. Eventually, fossil fuel emissions could be optimized within CarbonTracker, especially with the addition of $^{14}CO_2$ observations as constraints [Basu et al., 2016, 2020].

5 Oceans module

The oceans play an important role in the Earth's carbon cycle. They are the largest long-term sink for carbon and have an enormous capacity to store and redistribute CO_2 within the Earth system. Oceanographers estimate that about 48% of the CO_2 from fossil fuel burning has been absorbed by the ocean [Sabine et al., 2004]. The dissolution of CO_2 in seawater shifts the balance of the ocean carbonate equilibrium towards a more acidic state with a lower pH. This effect is already measurable [Caldeira and Wickett, 2003], and is expected to become an acute challenge to shell-forming organisms over the coming decades and centuries. Although the oceans as a whole have been a relatively steady net carbon sink, CO_2 can also be released from oceans depending on local temperatures, biological activity, wind speeds, and ocean circulation. These processes are all considered in CarbonTracker, since they can have significant effects on the ocean sink. Improved estimates of the air-sea exchange of carbon in turn help us to understand variability of both the atmospheric burden of CO_2 and terrestrial carbon exchange.

The initial release of CarbonTracker (CT2007) used climatological estimates of CO_2 partial pressure

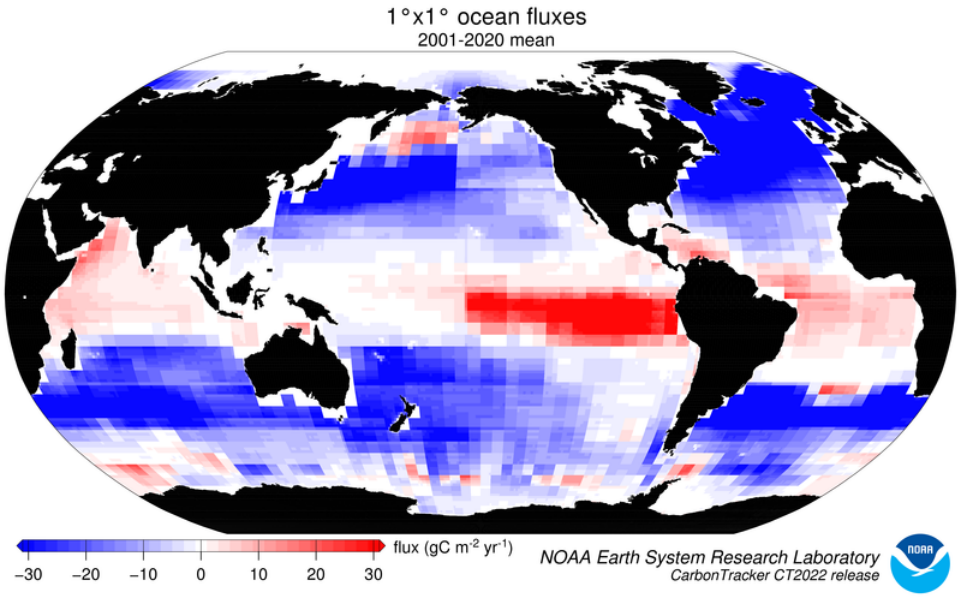

Figure 8: Posterior long-term mean ocean fluxes from CarbonTracker. The pattern of air-sea exchange of CO_2 averaged over the time period indicated, as estimated by CarbonTracker. Negative fluxes (blue colors) represent CO_2 uptake by the ocean, whereas positive fluxes (red colors) indicate regions in which the ocean is a net source of CO_2 to the atmosphere. Units are g C m^{-2} yr^{-1}.

in surface waters (pCO_2) from Takahashi et al. [2002] to compute a first-guess air-sea flux. This air-sea pCO_2 disequilibrium was modulated by a surface barometric pressure correction before being multiplied by a gas-transfer coefficient to yield a flux. Starting with CT2007B and continuing through the CT2011_oi release, the air-sea pCO_2 disequilibrium was imposed from analysis of ocean inversions [Jacobson et al., 2007, "OIF"] results, with short-term flux variability derived from the atmospheric model wind speeds via the gas transfer coefficient. The barometric pressure correction was removed so that climatological high- and low-pressure cells did not bias the long-term means of the first guess fluxes.

In CT2022, two models are used to provide prior estimates of air-sea CO_2 flux. The OIF scheme provides one of these flux priors, and the other is an updated version of the Takahashi et al. [2009] pCO_2 climatology.

5.1 Air-sea gas exchange

Oceanic uptake of CO_2 in CarbonTracker is computed using air-sea differences in partial pressure of CO_2 inferred either from ocean inversions (called "OIF" henceforth), or from a compilation of direct measurements of seawater pCO_2 (called "pCO_2-clim" henceforth). These air-sea partial pressure differences are combined with a gas transfer velocity computed from wind speeds in the atmospheric transport model to compute fluxes of carbon dioxide across the sea surface.

In either method, the first-guess fluxes have no interannual variability (IAV) other than a smooth trend. IAV in oceanic CO_2 flux is due to anomalies in surface pCO_2, such as those that occur in the tropical eastern Pacific during an El Niño, and to associated variability in winds, ocean circulation, and sea-surface properties. In CarbonTracker, only the surface winds (and hence gas transfer), manifest these interannual anomalies; the remaining IAV of flux must be inferred from atmospheric CO_2 signals.

In the following sections we describe the two ocean flux prior models. We then describe the air-sea gas transfer velocity parameterization and discuss details of the inversion methodology specific to oceanic exchange of CO_2.

5.2 OIF: the Ocean Inversion Fluxes prior

For the OIF prior, long-term mean air-sea fluxes and the uncertainties associated with them are derived from the ocean interior inversions reported in Jacobson et al. [2007]. These ocean inversion flux estimates are composed of separate preindustrial (natural) and anthropogenic flux inversions based on the methods described in Gloor et al. [2003] and biogeochemical interpretations of Gruber et al. [1996]. The uptake of anthropogenic CO_2 by the ocean is assumed to increase in proportion to atmospheric CO_2 levels, consistent with estimates from ocean carbon models.

OIF contemporary pCO_2 fields were computed by summing the preindustrial and anthropogenic flux components from inversions using five different configurations of the Princeton/GFDL MOM3 ocean general circulation model [Pacanowski and Gnanadesikan, 1998], then dividing by a gas transfer velocity computed from the European Centre for Medium-Range Weather Forecasts (ECMWF) ERA40 reanalysis. There are two small differences in first-guess fluxes in this computation from those reported in Jacobson et al. [2007]. First, the five OIF estimates all used Takahashi et al. [2002] pCO_2 estimates to provide high-resolution patterning of flux within inversion regions (the alternative "forward" model patterns were not used). To good approximation, this choice only affects the spatial and temporal distribution of flux within each of the 30 ocean inversion regions, not the magnitude of the estimated flux. Second, wind speed differences between the ERA40 product used in the offline analysis and the ECMWF operational model used in the online CarbonTracker analysis result in small deviations from the OIF estimates.

Other than the smooth trend in anthropogenic flux assumed by the OIF results, interannual variability (IAV) in the first guess ocean flux comes entirely from wind speed effects on the gas transfer velocity. This is because the ocean inversions retrieve only a long-term mean and smooth trend.

5.3 pCO_2-Clim: Takahashi climatology prior

The pCO_2-Clim prior is derived from the Takahashi et al. [2009] climatology of seawater pCO_2. This climatology was created from about 3 million direct observations of seawater pCO_2 around the world between 1970 and 2007. With the exception of measurements in the Bering Sea, these observations were all linearly extrapolated to the corresponding month of the year 2000 by assuming a constant trend of 1.5 μatm yr^{-1}. This set of global monthly measurements corrected to the reference year 2000 was then interpolated onto a regular grid using a modeled surface current field.

The Takahashi et al. [2009] product goes beyond providing this estimate of surface water pCO_2. They also compute climatological air-sea exchange of CO_2 by using the GLOBALVIEW-CO_2 atmospheric carbon dioxide product to compute air-sea ΔpCO_2, sea surface properties inferred from ocean climatologies, and winds from atmospheric reanalysis to estimate gas-transfer velocity. Unlike many other atmospheric analyses, we have chosen not to use the climatological fluxes as our prior, nor to use the climatological ΔpCO_2. Instead, we take only the seawater pCO_2 distribution from the Takahashi et al. [2009] climatology–our atmospheric model provides both pCO_2 in the air at the sea surface and the winds needed to estimate gas transfer. Seawater pCO_2 is extrapolated from 2000 to the actual year of the CarbonTracker simulation using a presumed increase of 1.5 μatm yr^{-1} at every point in the global ocean. This is the same trend used in Takahashi et al. [2009] to normalize observations from many years to the reference year of the analysis (2000).

5.4 Gas-transfer velocity and ocean surface properties

Both priors use CO_2 solubilities and Schmidt numbers computed from World Ocean Atlas 2009 (WOA09) climatological fields of sea surface temperature and sea surface salinity fields [Levitus et al., 2010]. Gas transfer velocity in CarbonTracker is parameterized as a quadratic function of wind speed following Wan-

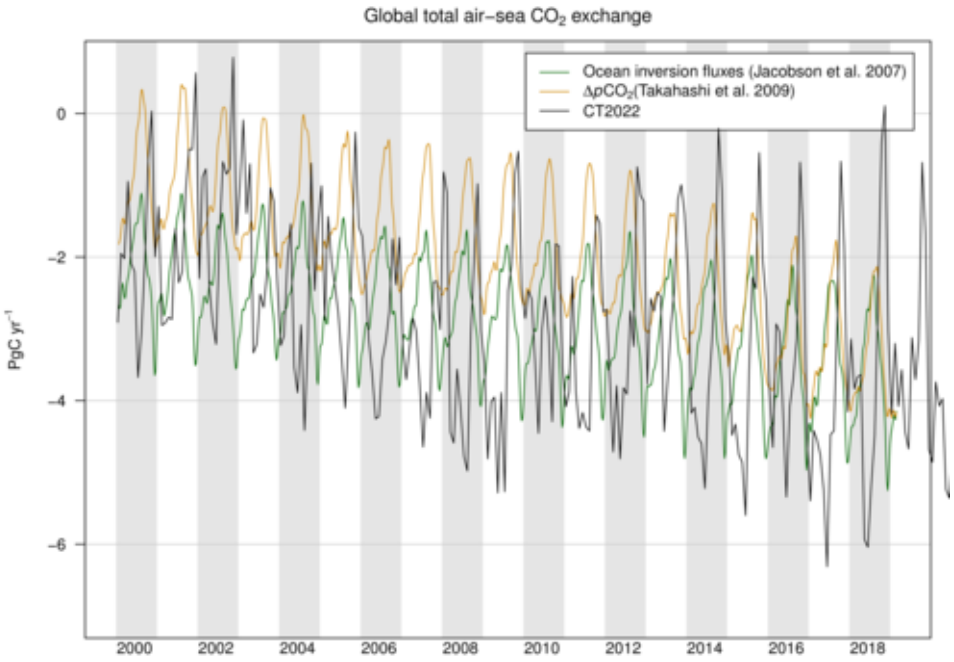

Figure 9: Comparison of air-sea flux priors and the CT2022 posterior. Global CO_2 uptake by the ocean, expressed in Pg C yr^{-1}. Positive flux represents a gain of CO_2 to the atmosphere, and the negative numbers here indicate that the ocean is a sink of CO_2. While both priors manifest similar trends of increasing oceanic uptake of CO_2, the OIF prior (in green) has more oceanic uptake and a greater annual cycle than the pCO_2-clim prior (in tan). The CT2022 across-model posterior estimate is shown in black for comparison.

ninkhof [1992], using the formulation for instantaneous winds. Gas exchange is computed every 3 hours using wind speeds from the ECMWF operational model as represented by the atmospheric transport model.

Air-sea transfer is inhibited by the presence of sea ice, and for this work fluxes are scaled by the daily sea ice fraction in each gridbox provided by the ECMWF forecast data.

5.5 Specifics of the inversion methodology related to air-sea CO_2 fluxes

The first-guess fluxes described here are subject to scaling during the CarbonTracker optimization process, in which atmospheric CO_2 mole fraction observations are combined with transport simulated by the atmospheric model to infer flux signals. Prior air-sea fluxes are adjusted within each of the 30 ocean inversion regions. In this process, signals of terrestrial flux in atmospheric CO_2 distribution can be erroneously interpreted as being caused by oceanic fluxes. This flux "aliasing" or "leakage" is evident in some regions as a change in the shape of the seasonal cycle of air-sea flux.

Prior uncertainties for the OIF and pCO_2-clim models are specified as uncertainties on scaling factors multiplying net CO_2 flux in each of the 30 ocean inversion regions. The pCO_2-clim prior has independent regional uncertainties (a diagonal prior covariance matrix), with the uncertainty standard deviation on each region set to 40%. The OIF prior uncertainty has a fully-covariate covariance matrix with off-diagonal elements representing the results of the ocean inversion of Jacobson et al. [2007]. The preindustrial flux uncertainty is time-independent, but the anthropogenic flux uncertainty grows in time as anthropogenic flux uptake increases. The latter is scaled to the simulation date, then added to the former. Total uncertainties are consistent with the Jacobson et al. [2007] results.

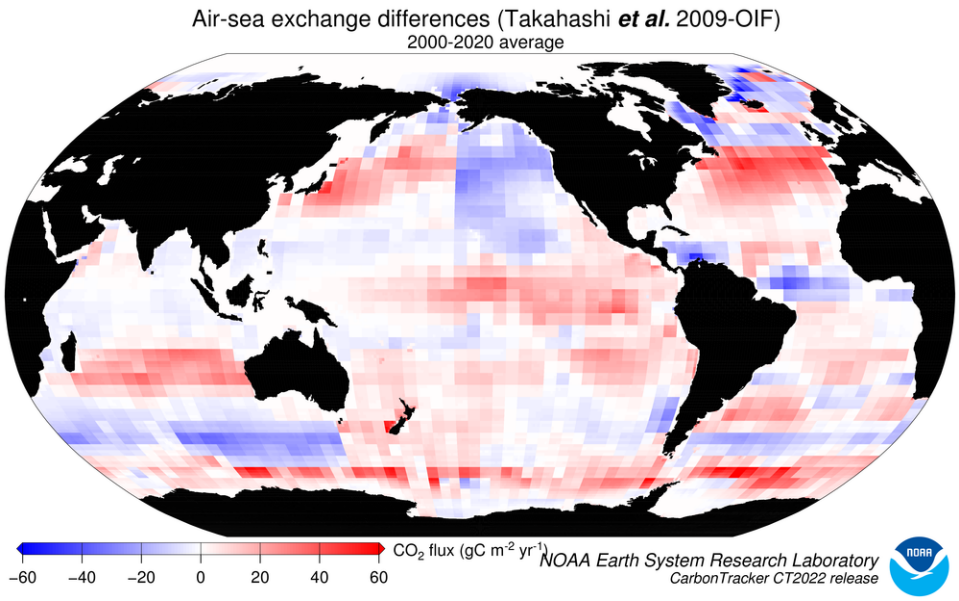

Figure 10: Differences in long-term mean ocean fluxes between the two priors. Red indicates areas where the pCO_2-clim prior has less oceanic uptake (or more outgassing to the atmosphere) than the OIF prior, and blue represents the opposite. Units are gC m-2 yr-1.

6 Atmospheric transport

The link between observations of CO_2 in the atmosphere and the exchange of CO_2 at the Earth's surface is transport in the atmosphere: storm systems, cloud complexes, and weather of all sorts cause winds that transport CO_2 around the world. As a result, local surface CO_2 exchange events like fires, forest growth, and ocean upwelling can have impacts at remote locations. To simulate the winds and the weather, CarbonTracker uses sophisticated numerical models that are driven by the daily weather forecasts from the specialized meteorological centers of the world. Since CO_2 does not decay or react in the lower atmosphere, the influence of emissions and uptake in locations such as North America and Europe are ultimately seen in our measurements even at the South Pole. Getting the transport of CO_2 just right is an enormous challenge, and costs us almost all of the computer resources for CarbonTracker. To represent the atmospheric transport, we use the Transport Model 5 (TM5). This is a community-supported model whose development is shared among many scientific groups with different areas of expertise. TM5 is used for many applications other than CarbonTracker, including forecasting air-quality, studying the dispersion of aerosols in the tropics, tracking biomass burning plumes, and predicting pollution levels that future generations might have to deal with.

6.1 TM5 offline tracer transport model

TM5 is an offline global chemical transport model with two-way nested grids. In this global model, regions for which high-resolution simulations are desired can be nested in the coarser global grid. The advantage to this approach is that transport simulations can be performed with a regional focus without the need for boundary conditions. Further, this approach allows measurements outside the "zoom" domain to constrain regional fluxes in the data assimilation, and ensures that regional estimates are consistent with global constraints. TM5 is based on a predecessor model TM3, with improvements in the advection scheme, vertical diffusion parameterization, and meteorological preprocessing of the wind fields [Krol et al., 2005].

The model is developed and maintained jointly by the Institute for Marine and Atmospheric Research

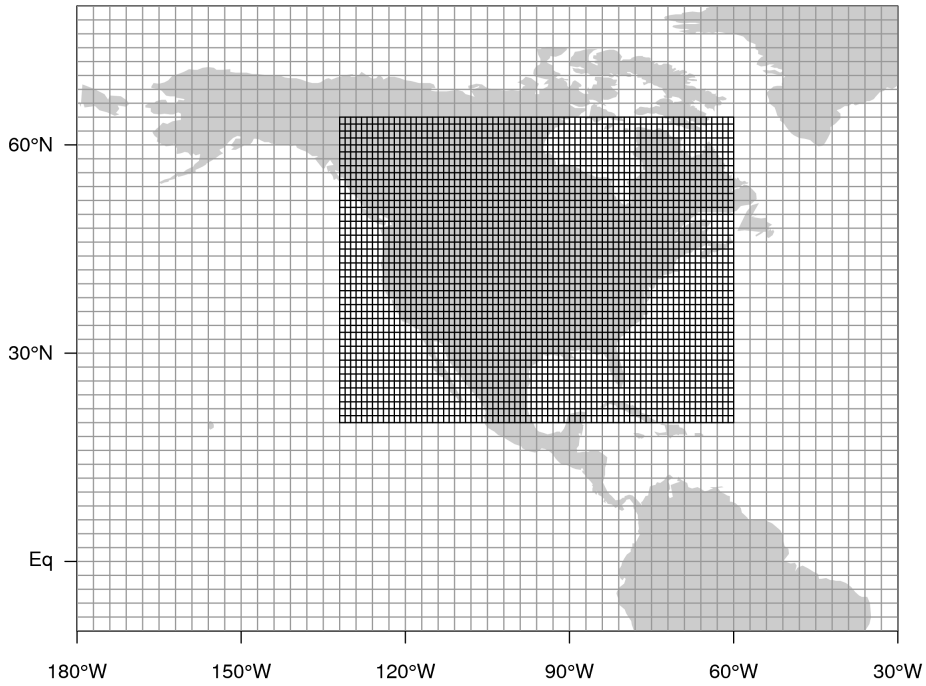

Figure 11: Nested grids used in CarbonTracker over North America. TM5 is a global model, but it employs nested grids to provide higher resolution over regions of interest. This figure shows the $1^\circ \times 1^\circ$ nested regional grid over North America and a portion of the global 3° longitude $\times$ 2° latitude grid.

Utrecht (IMAU, The Netherlands), the Joint Research Centre (JRC, Italy), the Royal Netherlands Meteorological Institute (KNMI), the Netherlands Institute for Space Research (SRON), and the NOAA Global Monitoring Laboratory (GML).

In CarbonTracker, TM5 separately simulates advection, deep and shallow convection, and vertical diffusion in both the planetary boundary layer and free troposphere. The carbon dioxide concentrations predicted by CarbonTracker do not feed back onto these predictions of winds.

Prior to use in TM5, ECMWF meteorological data are preprocessed into coarser grids, with attention to retrieving a flow that conserves tracer mass. Like most numerical weather prediction models, advection in the parent ECMWF model is not strictly mass-conserving, so this step is crucial. In CarbonTracker, TM5 is currently run at a global 3° longitude $\times$ 2° latitude resolution with a nested regional grid over North America at $1^\circ \times 1^\circ$ resolution (Figure 11). TM5 uses a dynamically-variable time step with a maximum length of 90 minutes. This overall timestep is dynamically reduced to maintain numerical stability, generally during times of high wind speeds. The timestep is divided in half and individual advection, diffusion, convection, and chemistry operators are applied symmetrically in each half step. Furthermore, transport operators in nested grids are modeled at shorter timesteps, so processes at the finest scales are conducted at an effective timestep of one-quarter the overall timestep. See Krol et al. [2005] for details.

The winds which drive TM5 come from the ERA5 reanalysis implemented in the European Centre for Medium-Range Weather Forecasts (ECMWF) modeling system. The ERA5 reanalysis uses CY41R2 version of the ECMWF Integrated Forecast System (IFS) model. That model uses a 12-minute time step and a spectral T639 horizontal resolution, which corresponds to approximately 28 km spacing at the equator on a reduced Gaussian grid. This version of the IFS has 137 model layers in the vertical, of which TM5 uses a 34-layer subset. These levels are listed in Table 1.

Model Level	Mean Height (m)	Model Level	Mean Height (m)
1	33	18	9400
2	109	19	10131
3	255	20	11011
4	477	21	11749
5	814	22	12492
6	1273	23	13393
7	1835	24	14304
8	2556	25	15226
9	3315	26	16322
10	4205	27	17446
11	5026	28	18459
12	5603	29	20380
13	6186	30	24376
14	6771	31	29834
15	7355	32	35623
16	8086	33	42602
17	8816	34	123210

Table 1: Mean mid-level heights in meters above ground from the ERA5 reanalysis using the TM5 34 level subset.

6.2 Convective flux fix

Until recently, TM5 was known to have difficulties representing the global surface distribution of sulfur hexafluoride (SF_6, see Figure 12 and Peters et al. [2004]). SF_6 is a nearly inert tracer in the atmosphere, with very small surface and atmospheric sinks and an atmospheric lifetime of about 1,000 years. Consequently, its global budget is very well known from observations alone. It is thought to be released mainly via leakage from electrical transformers. Since the electrical distribution system is closely tied to fossil fuel consumption, SF_6 is often considered an analog for fossil fuel CO_2 in the atmosphere. It is useful for understanding the rate at which Northern Hemisphere land surfaces are ventilated to the free troposphere, and the rate of interhemispheric exchange in models [Patra et al., 2011].

As a result of more than a decade's worth of work on understanding the apparently sluggish mixing in TM5 as revealed by SF_6 simulations, a fault in one of the vertical mixing parameterizations of the model was discovered. When it was originally created, TM5 implemented the same planetary boundary layer (PBL) mixing and convection schemes as the parent ECMWF model. Recent comparisons between TM5, the ECMWF parent model, and radiosonde profile data show that the PBL scheme in TM5 performs similarly to that of the parent ECMWF model. The convective scheme, however, does not produce similar results in TM5 as compared to the ECMWF model.

In a previous configuration of TM5, the convective entrainment and detrainment mass fluxes of the parent ECMWF model were re-diagnosed within TM5 using other meteorological information. The ECMWF model is used to produce both operational forecasts and the ERA-interim reanalysis, but the convective fluxes are stored for the ERA-interim product only. Thus, using ERA-interim meteorology, a direct comparison is possible. This comparison revealed that the TM5 internal rediagnosis of convective fluxes was faulty. TM5 was subsequently modified to use parent model ERA-interim convective fluxes directly. Using the parent model convective fluxes result in a significantly better SF_6 simulations. Simulations with these parent-model convective fluxes are said to use the "convective flux fix". Simulations with the convective flux fix show significantly improved agreement with SF_6 observations (see Figure 12).

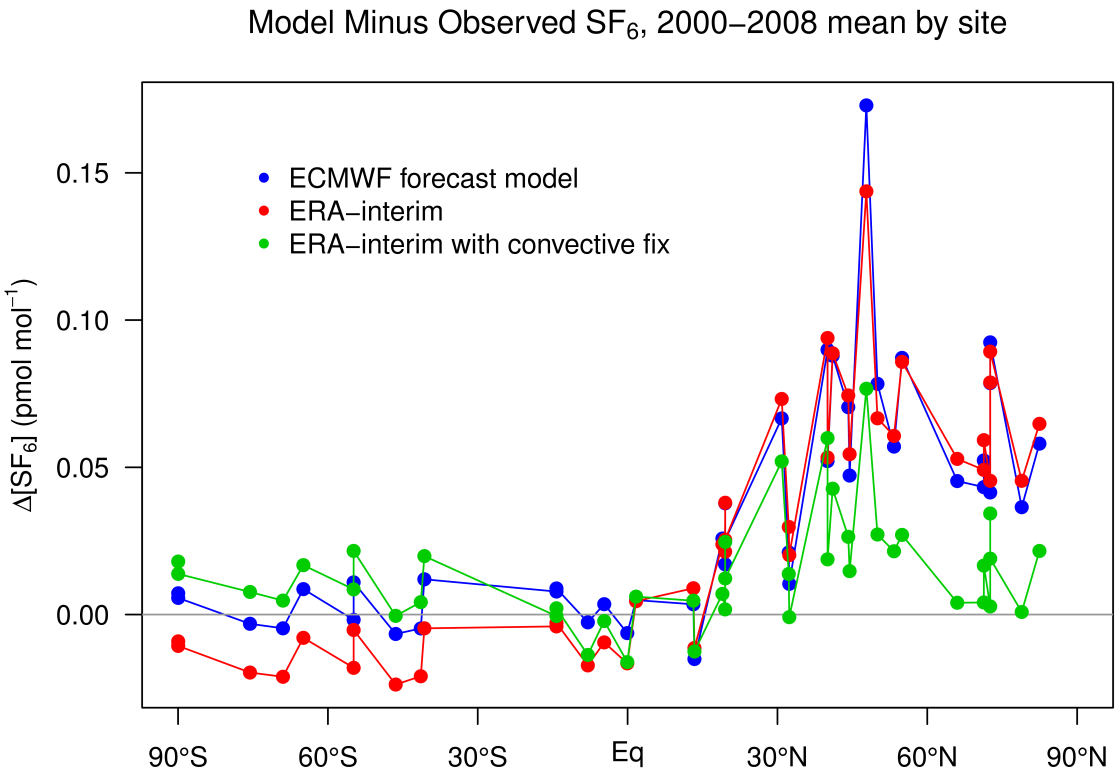

Figure 12: Long-term mean model residuals of SF_6 concentrations as a function of latitude. Residuals are defined as model-minus-observation, so a positive residual indicates the model has too much SF_6. Three different transport model simulations are shown. The ECMWF forecast (blue) and ERA-interim (red) transport simulations do not include the recent "convective flux fix". The ERA-interim with this convective flux fix is shown in green. Units are pmol mol^{-1}, or parts per trillion. CT2022 uses the ERA-interim transport with the convective flux fix.

Since the parent-model convective fluxes are only available for the ERA-interim product, CT2022 uses only ERA-interim transport with the convective flux fix. Previous releases of CarbonTracker also used the ECMWF operational model transport, for which parent-model convective fluxes are not available. We believe that TM5 simulations without the parent-model convective fluxes are faulty and should not be included in our product. When the convective flux fix was instituted in CT2013B, it resulted in the largest realignment of surface CO_2 fluxes in the history of the CarbonTracker program [Schuh et al., 2019]. This is a prominent example of the sensitive reliance of atmospheric inversions on accurate atmospheric transport.

7 Observations

The observations of atmospheric CO_2 mole fraction made by NOAA GML and partner laboratories are at the heart of CarbonTracker. They inform us on changes in the carbon cycle, whether those changes are regular (such as the annual cycle of growth and decay of leaves and other plant matter), or irregular (such as the release of tons of carbon by a wildfire). The results in CarbonTracker depend directly on the quality, location, and frequency of available observations. The level of detail at which we can retrieve information on the carbon cycle increases strongly with the density of the CO_2 observing network.

7.1 The CarbonTracker observational network

Observations simulated by CT2022 are supplied by the GLOBALVIEW+ data product version 7.0 [**?**], available at the NOAA GML ObsPack web site. This study uses measurements of air samples collected at 559 sites around the world by 66 laboratories:

- Penn State University (PSU)
- NOAA Global Monitoring Laboratory (NOAA)
- Instituto de Pesquisas Energeticas e Nucleares (IPEN)
- Environment and Climate Change Canada (ECCC)
- AVOCET Group @ NASA LaRC (NASA-LaRC)
- National Institute for Environmental Studies (NIES)
- CSIRO Oceans and Atmosphere, Climate Science Centre - GASLAB (CSIRO)
- Chinese Academy of Meteorological Sciences (CMA)
- Scripps Institution of Oceanography (SIO)
- Scripps Institution of Oceanography CO2 Program (SIO_CO2)
- Max Planck Institute for Biogeochemistry (MPI-BGC)
- Laboratoire des Sciences du Climat et de l'Environnement - UMR8212 CEA-CNRS-UVSQ (LSCE)
- Japan Meteorological Agency (JMA)
- NOAA Chemical Sciences Division (NOAA-CSD)
- National Institute of Water and Atmospheric Research (NIWA)
- ICOS ATMOSPHERE THEMATIC CENTRE (ICOS-ATC)
- Norwegian Institute for Air Research (NILU)
- University of Bern, Physics Institute, Climate and Environmental Physics (KUP)
- Atmospheric Chemistry Research Group School of Chemistry University of Bristol (UNIVBRIS)
- Harvard University (HU)
- Netherlands Organisation for Applied Scientific Research (TNO)
- California Institute of Technology, Division of Geological and Planetary Science (CALTECH)
- Institute of Atmospheric Sciences and Climate (CNR-ISAC) (CNR-ISAC)
- Meteorological Research Institute (MRI)
- South African Weather Service (SAWS)
- University of Exeter, Centre for Environmental Data Analysis (CEDA)
- Institut de Ciencia i Tecnologia Ambientals, Universitat Autonoma de Barcelona (ICTA-UAB)
- Lawrence Berkeley National Laboratory and ARM Climate Research Facility (LBNL-ARM)
- Hohenpeissenberg Meteorological Observatory (HPB)
- Earth Networks, Inc. (EN)
- NASA Goddard Space Flight Center (NASA-GSFC)
- National Center For Atmospheric Research (NCAR)
- University of Heidelberg, Institut fuer Umweltphysik (UHEI-IUP)
- NOAA ESRL Halocarbons and Other Atmospheric Trace Species (NOAA-HATS)
- Hong Kong Observatory (HKO)
- Lund University - Centre for Environmental and Climate Research (LUND-CEC)
- Hungarian Meteorological Service (HMS)
- Karlsruhe Institute of Technology (IMK-ASF) (KIT/IMK-ASF)
- Institute for Atmospheric and Environmental Sciences, University of Frankfurt (IAU)
- Joint Research Centre (JRC)
- Izana Atmospheric Research Center, Meteorological State Agency of Spain (AEMET)
- High Altitude Research Stations Jungfraujoch and Gornergrat International Foundation (HFSJG)

Source	Online availability	Comment
GLOBALVIEW+ v7.0	ObsPack download	Main source of observations
GLOBALVIEW+ v8.0	ObsPack download	Observations since Jan 1, 2021
NIES shipboard observations	Available from NIES	No permission to redistribute

Table 2: Sources of CO_2 observational data for CT2022

- Swiss Federal Laboratories for Materials Science and Technology (EMPA)
- University of Science and Technology (AGH) (AGH)
- University of Minnesota (UofMN)
- Integrated Carbon Observation System - Flask and Calibration Laboratory (ICOS)
- Czechglobe - Global Change Research Institute CAS (CAS)
- University of Wisconsin (UofWI)
- National Agency for New Technology, Energy, and Environment (ENEA)
- University of Groningen (RUG), Centre for Isotope Research (CIO) (RUG)
- Oregon State University (OSU)
- Finnish Meteorological Institute (FMI)
- Ricerca sul Sistema Energetico (RSE)
- Commissariat l'nergie atomique et aux nergies alternatives (CEA)
- Savannah River National Laboratory (SRNL)
- University of Helsinki (UHELS)
- University of Virginia (UofVA)
- Umweltbundesamt, Station Schauinsland (UBA-SCHAU)
- Lawrence Berkeley National Laboratory (LBNL)
- Forest Ecology and Management, SLU Ume (SLU)
- Center for Atmospheric and Oceanic Studies, Tohoku University (TU)
- University of East Anglia (UEA)
- Main Geophysical Observatory (MGO)
- Utah Atmospheric Trace gas & Air Quality (U-ATAQ)
- Umweltbundesamt, Zugspitze GAW Station (UBA/ZUG)

The CO_2 measurement data assimilated in CT2022 are freely available for download from the GML ObsPack web portal or from partner websites. The bulk of assimilated measurements come from GLOBALVIEWplus v7.0 (2021) and from the GLOBALVIEWplus v8.0 product. Additional observations were gathered from specialized ObsPack products as detailed in Table 2.

We also make available an ObsPack containing the simulated values of all measurement data considered by CT2022. This CT2022 ObsPack contains most, but not all, of the measured values. Measured values are only distributed directly when we have permission to do so.

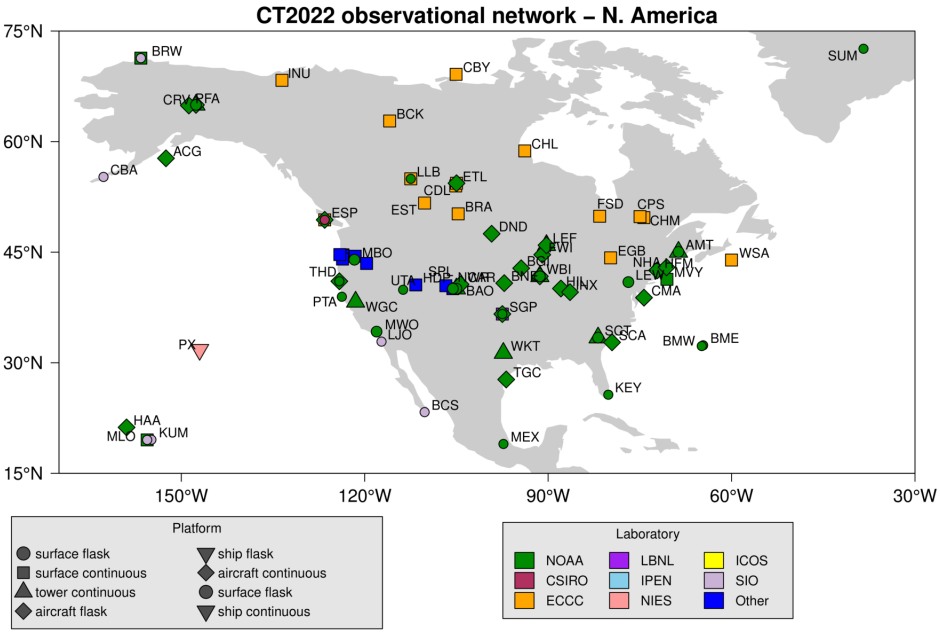

Figure 13: CarbonTracker observational network over North America. See the CarbonTracker interactive network map for more details.

Users are encouraged to review the usage requirements for these data products, and to contact the measurement laboratories directly for details about the observations.

With the advent in 2015 of GLOBALVIEW+, data are now presented to CarbonTracker with a higher temporal frequency than in past observational products. At sites with quasi-continuous monitoring, CT2022 assimilates hourly average CO_2 concentrations. In the past, a single daily assimilation value was constructed at these sites, generally a four-hour average during well-mixed background conditions. At continental sites, this four-hour period was generally from local noon to 4pm; at many mountain sites background conditions are met at nighttime when upslope winds are uncommon. Using GLOBALVIEW+, CarbonTracker can now assimilate each hourly average during these background conditions independently. For many sites, all available hourly averages throughout the day are assimilated. Details vary by dataset, but can be checked at the interactive data plotting page.

Note that all of these observations are calibrated against the same world CO_2 standard (WMO-X2007).

Starting with GLOBALVIEW+, we generally use the recommendations of data providers as to which observations are appropriate for assimilation. Such observations are identified by a variable in the ObsPack distribution, obs_flag. Only observations with obs_flag = 1 are identified for assimilation by data providers. We modify the designation of assimilation data for Environment and Climate Change Canada

quasi-continuous sampling sites. For these data, obs_flag is set to 1 by the data provider for times when they represent the daily minimum CO_2 concentration. This is generally later in the day than our standard scheme of local noon-4pm used to represent times of well-mixed PBLs. For these datasets, we have changed obs_flag to indicate assimilation only for the local noon - 4pm time period. These selected observations are further filtered based on the CCG curve fitting routine of Thoning et al. [1989]. This filter fits a smooth curve to the selected observations, and measurements more than 3 standard deviations away from this curve are excluded from assimilation.

At mountain-top sites (*e.g.* MLO, NWR, and SPL), it is usually nighttime hours that are selected for assimilation, as these tend to be the most stable time period. Nighttime hours also avoid periods of upslope flows that contain local vegetative and/or anthropogenic influence.

Data from the Sutro tower (STR) and the Boulder (Erie, Colorado) tower (BAO) are strongly influenced by local urban emissions, which CarbonTracker is unable to resolve. At these two sites, pollution events have been identified using co-located measurements of carbon monoxide. In this study, measurements thought to be affected by pollution events have been excluded. This technique is under active refinement.

With CT2022, we have begun to assimilate CO_2 measurements from NOAA light aircraft profiling time series, from intakes at multiple levels on NOAA tall towers, and from extensive shipboard and Siberian tower measurements collected by our partners at NIES. These datasets can be explored at the interactive data plotting page.

We apply a further selection criterion during the assimilation to exclude non-marine boundary layer (MBL) observations that are very poorly forecasted in our framework. We use the so-called model-data mismatch in this process, which is the random error ascribed to each observation to account for measurement errors as well as modeling errors of that observation. We interpret an observed-minus-forecasted mole fraction that exceeds 3 times the prescribed model-data mismatch as an indicator that our modeling framework fails. This can happen for instance when an air sample is representative of local exchange not captured well by our $1^\circ \times 1^\circ$ fluxes, when local meteorological conditions are not captured by our offline transport fields, but also when large-scale CO_2 exchange is suddenly changed (*e.g.* fires, pests, droughts) to an extent that can not be accommodated by our flux modules. This last situation would imply an important change in the carbon cycle and has to be recognized by the researchers when analyzing the results. In accordance with the 3-sigma rejection criterion, about 0.2% of the observations are discarded through this mechanism in our assimilation.

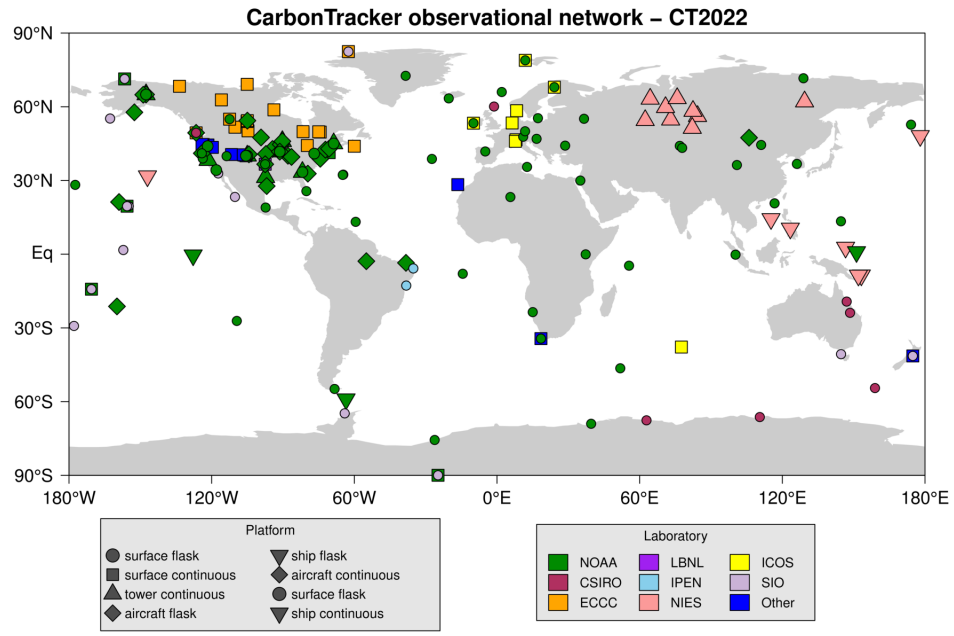

Figure 14: CarbonTracker global observational network. See the CarbonTracker interactive network map for more details.

7.2 Adaptive model-data mismatch

The statistical optimization method we use to constrain surface CO_2 fluxes requires that each assimilation constraint is assigned a "model-data mismatch" (MDM) error value. This is meant to express the statistics of simulated-minus-observed CO_2 observations we could expect if CarbonTracker were using perfect surface fluxes. Such deviations arise from many sources, including random noise in the measurement system, *in situ* variability that we do not expect to resolve in our model, and faults with the atmospheric transport model. Generally, transport and inverse model faults are the dominant terms in MDM values. The MDM is one of two major "tuning knobs" used to adjust the performance of our ensemble Kalman filter. The other is also an error quantity, meant to represent the expected error on our first-guess fluxes. Discussion of this prior covariance error can be found in section 8.2.

Prior to CT2015, CarbonTracker used a single MDM value for each assimilation dataset. The NOAA continuous observations at the 396m level of the WLEF tower in northern Wisconsin, for example, were assigned a MDM of 3.0 ppm, meaning that the residuals between model-forecasted measurements and the actual observed concentrations are expected to be unbiased (*i.e.*, have a mean of zero) and have a standard deviation of 3 ppm. In practice, however, we have found that it is far easier to simulate wintertime observations than those during summer. This is mainly due to higher ambient variability of CO_2 in the summer.

Starting with CT2016, we began to use an empirical scheme to assign MDM values, exploiting statistics of model performance from independently-configured preliminary inversions. The posterior residuals for each dataset are classified into relevant bins, and then statistics of model performance are analyzed within each of those bins. For every dataset, these bins include equally-spaced intervals of one-tenth of a year. For analyzers collecting data throughout the day, we also classify the measurements into 4-hour intervals of local time. For aircraft datasets, we further classify measurements into vertical levels of 1000m thickness (0-1000 m ASL, 1000-2000 m ASL, etc.). For each of these bins, bias and random error are combined to form total deviation from observed values as a root-mean square error (RMSE). The assigned MDM is set to a constant fraction of this total RMSE. This scaling is meant to force the assimilation scheme to extract as much information as possible from available observations. We use two different scaling factors to convert RMSE to MDM, depending on whether the preliminary inversions actually assimilated the measurements in the relevant bin, or merely simulated those measurements. For measurements assimilated by the preliminary inversions, the MDM is 0.95 $*$ RMSE; for measurements not assimilated in the preliminary inversions, the MDM is 0.85 $*$ RMSE.

The adaptive MDM scheme performs well in terms of average χ^2, which in an optimally-tuned system should be close to 1.0 for each dataset (see Table 3). Notably, the seasonal variations of MDM successfully compensate for the higher ambient variability of CO_2 at continental sites during the growing season. It is, however, an iterative process, requiring that we conduct a previous inversion. For various reasons, this previous inversion performed before CT2022 differs in significant aspects from the actual CT2022 inversions. These differences have led to MDM values which are slightly too large and thus average χ^2 values which are generally smaller than the target of 1.0 (in some cases, as low as 0.2 or 0.3). The next iteration of CarbonTracker will be able to use the more recent CT2022 inversions to refine the adaptive MDM scheme.

Duplicate observations are identified as those within 50 minutes temporally, 10m vertically, and 0.05 degrees of latitude and longitude laterally (nominally, about 5km). The MDM for such observations is inflated by $\sqrt{n}$, where n is the number of duplicates.

7.3 Statistical performance of CT2022

Starting with CT2022, we reserved about 5% of available assimilation data for a cross-validation exercise. To the extent possible, withheld measurements were chosen to be independent from other observations. For surface flask observations, which are generally collected on a weekly time basis, all samples are considered

independent from one another, so withheld data were selected randomly. Aircraft flasks collected during a profile are considered co-dependent, so entire profiles were randomly selected for withholding. Finally, for *in situ* analyzers with quasi-continuous sampling (towers, observatories), 24-hour periods were randomly chosen and that entire day's worth of data were withheld. Shipboard quasi-continuous datasets, which account for more than a quarter of assimilation data for CT2022 were inadvertently excluded from this cross-validation exercise. As a result, about 3% (115,756 measurements out of about 4.2 million) were withheld.

Each residual from the withheld measurements was normalized by its prescribed model-data mismatch (MDM) error, to form a set of χ values. The mean χ^2, which for a perfect set of independent, normally-distributed variates should approach 1.0, was found to be 0.92.

Table 3 summarizes the datasets assimilated in CarbonTracker, and the performance of the assimilation scheme for each dataset. These diagnostics are useful for evaluating how well CarbonTracker does in simulating observed CO_2.

Dataset	Lab.	Location	Latitude	Longitude	Elev. (m)	Used	Rej.	Unsampled	R (ppm)	χ^2	Bias (ppm)	SE (ppm)
co2_abp_surface-flask_1_representative	NOAA	Arembepe, Bahia, Brazil	12.77°S	38.17°W	1	90	1	0	0.1 - 4.5	0.41	-0.98	0.97
co2_abp_surface-flask_26_marine	IPEN	Arembepe, Bahia, Brazil	12.77°S	38.17°W	1	100	1	0	0.3 - 67.4	0.46	-3.11	12.66
co2_acg_aircraft-pfp_1_allvalid_0-1000masl	NOAA	Alaska Coast Guard, United States	57.74°N	152.50°W	440	402	26	0	0.1 - 6.8	1.19	-0.59	2.76
co2_acg_aircraft-pfp_1_allvalid_1000 2000masl	NOAA	Alaska Coast Guard, United States	57.74°N	152.50°W	1490	204	18	0	0.1 - 4.1	1.37	-0.23	1.71
co2_acg_aircraft-pfp_1_allvalid_2000-3000masl	NOAA	Alaska Coast Guard, United States	57.74°N	152.50°W	2533	118	15	0	0.4 - 2.5	1.71	-0.03	1.26
co2_acg_aircraft-pfp_1_allvalid_3000 4000masl	NOAA	Alaska Coast Guard, United States	57.74°N	152.50°W	3530	112	11	0	0.2 - 2.1	1.61	0.09	1.28
co2_acg_aircraft-pfp_1_allvalid_4000-5000masl	NOAA	Alaska Coast Guard, United States	57.74°N	152.50°W	4424	100	7	0	0.4 - 2.0	1.31	-0.19	1.30
co2_acg_aircraft-pfp_1_allvalid_5000 6000masl	NOAA	Alaska Coast Guard, United States	57.74°N	152.50°W	5494	116	8	0	0.5 - 2.8	1.45	-0.07	1.35
co2_acg_aircraft-pfp_1_allvalid_6000-7000masl	NOAA	Alaska Coast Guard, United States	57.74°N	152.50°W	6443	117	8	0	0.3 - 3.3	1.69	0.06	1.36
co2_acg_aircraft-pfp_1_allvalid_7000 8000masl	NOAA	Alaska Coast Guard, United States	57.74°N	152.50°W	7495	149	3	0	0.3 - 2.8	1.38	0.00	1.40
co2_acg_aircraft-pfp_1_allvalid_8000-9000masl	NOAA	Alaska Coast Guard, United States	57.74°N	152.50°W	8342	20	0	0	0.4 - 1.5	1.32	0.69	0.65
co2_ah2_shipboard-insitu_20_allvalid	NIES	Alligator Hope (M/S Alligator Hope of Mitsui O.S.K. Lines, Ltd.)	variable		Surface	27567	2718	0	0.3 - 94.0	1.13	-0.48	2.92
co2_alt_surface-flask_1_representative	NOAA	Alert, Nunavut, Canada	82.45°N	62.51°W	185	1421	16	0	0.2 - 5.5	0.38	-0.09	0.81

(table continued on next page)

Dataset	Lab.	Location	Latitude	Longitude	Elev. (m)	Used	Rej.	Unsampled	R (ppm)	χ^2	Bias (ppm)	SE (ppm)
co2_alt_surface-flask_2_representati	CSIRO	Alert, Nunavut, Canada	82.45°N	62.51°W	185	790	45	0	0.1 - 8.8	1.05	0.04	0.86
co2_alt_surface-flask_4_representative	SIO	Alert, Nunavut, Canada	82.45°N	62.51°W	185	475	7	0	0.4 - 6.1	0.53	-0.02	0.81
co2_alt_surface-flask_426_represent	SIO_CO2	Alert, Nunavut, Canada	82.45°N	62.51°W	185	645	5	0	0.5 - 7.6	0.38	-0.16	0.89
co2_alt_surface-insitu_6_allvalid	ECCC	Alert, Nunavut, Canada	82.45°N	62.51°W	185	22934	1648	0	0.5 - 3.8	1.16	-0.07	0.79
co2_ams_surface-insitu_11_allvalid	LSCE	Amsterdam Island, France	37.80°S	77.54°E	55	31170	106	0	0.3 - 1.0	0.41	-0.05	0.28
co2_amt_surface-pfp_1_allvalid-107magl	NOAA	Argyle, Maine, United States	45.03°N	68.68°W	53	1621	8	0	1.6 - 25.2	0.61	0.16	3.69
co2_amt_tower-insitu_1_allvalid-107magl	NOAA	Argyle, Maine, United States	45.03°N	68.68°W	53	19889	582	0	1.4 - 8.7	0.98	0.14	3.66
co2_amt_tower-insitu_1_allvalid-12magl	NOAA	Argyle, Maine, United States	45.03°N	68.68°W	53	18492	565	0	1.5 - 5.7	1.02	0.40	3.97
co2_amt_tower-insitu_1_allvalid-30magl	NOAA	Argyle, Maine, United States	45.03°N	68.68°W	53	13447	437	0	1.5 - 5.8	1.08	0.64	4.04
co2_ara_surface-flask_2_representative	CSIRO	Arcturus, Queensland, Australia	23.86°S	148.47°E	175	16	0	0	1.7 - 4.3	0.53	-0.15	2.43
co2_asc_surface-flask_1_representati	NOAA	Ascension Island, United Kingdom	7.97°S	14.40°W	85	1691	0	0	0.5 - 1.3	1.14	0.13	0.73
co2_ask_surface-flask_1_representative	NOAA	Assekrem, Algeria	23.26°N	5.63°E	2710	827	22	0	0.3 - 0.9	1.25	-0.23	0.69
co2_azr_surface-flask_1_representati	NOAA	Terceira Island, Azores, Portugal	38.77°N	27.38°W	19	525	20	0	0.5 - 2.3	1.08	0.07	1.39
co2_azv_tower-insitu_20_allvalid-29magl	NIES	Azovo, Russia	54.70°N	73.03°E	110	10687	434	0	1.9 - 4.9	1.12	-0.89	3.84
co2_azv_tower-insitu_20_allvalid-50magl	NIES	Azovo, Russia	54.70°N	73.03°E	110	10387	405	0	1.9 - 5.0	1.11	-0.71	3.82

(table continued on next page)

Dataset	Lab.	Location	Latitude	Longitude	Elev. (m)	Used	Rej.	Unsampled	R (ppm)	χ^2	Bias (ppm)	SE (ppm)
co2_bal_surface-flask_1_representative	NOAA	Baltic Sea, Poland	55.35°N	17.22°E	3	899	16	0	0.6 - 12.2	0.82	-2.23	5.54
co2_bao_surface-pfp_1_allvalid-300magl	NOAA	Boulder Atmospheric Observatory, Colorado, United States	40.05°N	105.00°W	1584	2348	3	0	2.4 - 26.5	0.40	-1.83	2.97
co2_bao_tower-insitu_1_allvalid-100magl	NOAA	Boulder Atmospheric Observatory, Colorado, United States	40.05°N	105.00°W	1584	9441	209	0	2.2 - 12.9	0.82	-3.10	5.49
co2_bao_tower-insitu_1_allvalid-22magl	NOAA	Boulder Atmospheric Observatory, Colorado, United States	40.05°N	105.00°W	1584	9555	202	0	2.3 - 16.6	0.80	-3.43	6.38
co2_bao_tower-insitu_1_allvalid-300magl	NOAA	Boulder Atmospheric Observatory, Colorado, United States	40.05°N	105.00°W	1584	62262	637	0	2.1 - 24.7	0.70	0.14	4.61
co2_bck_surface-insitu_6_allvalid	ECCC	Behchoko, Northwest Territories, Canada	62.80°N	115.92°W	160	10702	734	0	1.6 - 3.7	1.10	0.06	2.31
co2_bcs_surface-flask_426_representative	SIO_CO2	Baja California Sur, Mexico	23.30°N	110.20°W	4	115	1	0	0.3 - 3.8	0.56	0.65	1.83
co2_bgi_aircraft-pfp_1_allvalid_0-1000masl	NOAA	Bradgate, Iowa, United States	42.82°N	94.41°W	611	5	0	0	2.7 - 7.6	1.04	-2.50	3.07
co2_bgi_aircraft-pfp_1_allvalid_1000-2000masl	NOAA	Bradgate, Iowa, United States	42.82°N	94.41°W	1587	45	3	0	0.5 - 4.6	1.15	-0.58	2.61
co2_bgi_aircraft-pfp_1_allvalid_2000 3000masl	NOAA	Bradgate, Iowa, United States	42.82°N	94.41°W	2548	15	1	0	0.5 - 1.6	1.14	0.14	0.92
co2_bgi_aircraft-pfp_1_allvalid_3000-4000masl	NOAA	Bradgate, Iowa, United States	42.82°N	94.41°W	3524	46	5	0	0.2 - 3.5	1.30	0.19	1.46
co2_bgi_aircraft-pfp_1_allvalid_4000 5000masl	NOAA	Bradgate, Iowa, United States	42.82°N	94.41°W	4569	23	3	0	0.1 - 1.1	1.58	0.34	0.76
co2_bgi_aircraft-pfp_1_allvalid_5000-6000masl	NOAA	Bradgate, Iowa, United States	42.82°N	94.41°W	5506	38	0	0	0.3 - 1.5	1.19	0.07	0.97

(table continued on next page)

Dataset	Lab.	Location	Latitude	Longitude	Elev. (m)	Used	Rej.	Unsampled	R (ppm)	χ^2	Bias (ppm)	SE (ppm)
co2_bgi_aircraft-pfp_1_allvalid_6000-7000masl	NOAA	Bradgate, Iowa, United States	42.82°N	94.41°W	6474	37	1	0	0.2 - 2.6	1.13	0.19	1.20
co2_bgi_aircraft-pfp_1_allvalid_7000-8000masl	NOAA	Bradgate, Iowa, United States	42.82°N	94.41°W	7469	35	0	0	0.3 - 1.4	0.77	-0.05	0.69
co2_bgi_aircraft-pfp_1_allvalid_8000-9000masl	NOAA	Bradgate, Iowa, United States	42.82°N	94.41°W	8050	3	0	0	0.9 - 0.9	0.39	-0.11	1.02
co2_bhd_surface-flask_1_representative	NOAA	Baring Head Station, New Zealand	41.41°S	174.87°E	85	249	2	0	0.2 - 6.5	0.82	0.04	1.10
co2_bhd_surface-flask_426_represent	SIO_CO2	Baring Head Station, New Zealand	41.41°S	174.87°E	85	145	6	0	0.4 - 4.3	0.86	0.99	1.51
co2_bhd_surface-insitu_15_baseline	NIWA	Baring Head Station, New Zealand	41.41°S	174.87°E	85	673	6	0	0.5 - 4.9	0.65	0.56	0.77
co2_bir_surface-insitu_442_allvalid-10magl	ICOS-ATC	Birkenes Observatory, Norway	58.39°N	8.25°E	215	207	4	0	2.1 - 3.4	0.97	-0.20	3.15
co2_bir_surface-insitu_56_allvalid	NILU	Birkenes Observatory, Norway	58.39°N	8.25°E	215	2690	310	0	1.6 - 5.0	1.26	-2.05	5.06
co2_bkt_surface-flask_1_representati	NOAA	Bukit Kototabang, Indonesia	0.20°S	100.32°E	845	510	0	0	3.8 - 7.5	1.04	4.40	3.74
co2_bme_surface-flask_1_representative	NOAA	St. Davids Head, Bermuda, United Kingdom	32.37°N	64.65°W	12	221	4	0	0.8 - 2.7	1.02	0.37	1.63
co2_bmw_surface-flask_1_representati	NOAA	Tudor Hill, Bermuda, United Kingdom	32.26°N	64.88°W	30	675	18	0	0.5 - 2.4	1.09	0.53	1.36
co2_bne_aircraft-pfp_1_allvalid_0-1000masl	NOAA	Beaver Crossing, Nebraska, United States	40.80°N	97.18°W	633	65	2	0	1.5 - 10.6	0.69	-0.65	3.81
co2_bne_aircraft-pfp_1_allvalid_1000-2000masl	NOAA	Beaver Crossing, Nebraska, United States	40.80°N	97.18°W	1383	162	5	0	0.5 - 7.3	1.19	-0.42	2.60
co2_bne_aircraft-pfp_1_allvalid_2000-3000masl	NOAA	Beaver Crossing, Nebraska, United States	40.80°N	97.18°W	2294	106	2	0	0.4 - 8.9	1.00	-0.28	1.86

(table continued on next page)

Dataset	Lab.	Location	Latitude	Longitude	Elev. (m)	Used	Rej.	Unsampled	R (ppm)	χ^2	Bias (ppm)	SE (ppm)
co2_bne_aircraft-pfp_1_allvalid_3000 4000masl	NOAA	Beaver Crossing, Nebraska, United States	40.80°N	97.18°W	3396	139	6	0	0.1 - 9.7	1.27	-0.19	1.67
co2_bne_aircraft-pfp_1_allvalid_4000-5000masl	NOAA	Beaver Crossing, Nebraska, United States	40.80°N	97.18°W	4278	76	4	0	0.1 - 12.5	1.22	-0.32	2.39
co2_bne_aircraft-pfp_1_allvalid_5000 6000masl	NOAA	Beaver Crossing, Nebraska, United States	40.80°N	97.18°W	5392	109	7	0	0.2 - 14.4	1.14	-0.17	2.20
co2_bne_aircraft-pfp_1_allvalid_6000-7000masl	NOAA	Beaver Crossing, Nebraska, United States	40.80°N	97.18°W	6362	107	3	0	0.2 - 14.9	1.13	-0.13	2.29
co2_bne_aircraft-pfp_1_allvalid_7000 8000masl	NOAA	Beaver Crossing, Nebraska, United States	40.80°N	97.18°W	7657	85	2	0	0.1 - 23.0	1.39	-0.04	3.78
co2_bne_aircraft-pfp_1_allvalid_8000-9000masl	NOAA	Beaver Crossing, Nebraska, United States	40.80°N	97.18°W	8072	27	0	0	0.4 - 1.2	1.40	-0.49	0.94
co2_bra_surface-insitu_6_allvalid	ECCC	Bratt's Lake Saskatchewan, Canada	50.20°N	104.71°W	595	10462	437	0	1.8 - 3.9	1.07	-0.06	2.55
co2_brw_surface-flask_1_representative	NOAA	Barrow Atmospheric Baseline Observatory, United States	71.32°N	156.61°W	11	1834	30	0	0.2 - 13.8	0.57	-0.27	1.43
co2_brw_surface-flask_426_represent	SIO_CO2	Barrow Atmospheric Baseline Observatory, United States	71.32°N	156.61°W	11	754	6	0	0.7 - 10.8	0.48	-0.20	1.48
co2_brw_surface-insitu_1_allvalid	NOAA	Barrow Atmospheric Baseline Observatory, United States	71.32°N	156.61°W	11	34112	1906	0	1.0 - 5.6	0.99	-0.19	1.25
co2_brz_aircraft-insitu_20_allvalid_0 1000masl	NIES	Berezorechka, Russia	56.15°N	84.33°E	636	30842	190	0	1.5 - 185.6	0.27	-0.38	3.48
co2_brz_aircraft-insitu_20_allvalid_1000-2000masl	NIES	Berezorechka, Russia	56.15°N	84.33°E	1501	41597	166	0	1.1 - 75.6	0.22	-0.40	2.85

(table continued on next page)

Dataset	Lab.	Location	Latitude	Longitude	Elev. (m)	Used	Rej.	Unsampled	R (ppm)	χ^2	Bias (ppm)	SE (ppm)
co2_brz_aircraft-insitu_20_allvalid_2 3000masl	NIES	Berezorechka, Russia	56.15°N	84.33°E	2408	18582	61	0	0.9 - 64.1	0.21	-0.27	2.26
co2_brz_aircraft-insitu_20_allvalid_3000-4000masl	NIES	Berezorechka, Russia	56.15°N	84.33°E	3085	2446	24	0	0.4 - 41.2	0.27	-0.31	2.17
co2_brz_tower-insitu_20_allvalid-20magl	NIES	Berezorechka, Russia	56.15°N	84.33°E	168	13640	563	0	2.1 - 19.0	1.03	-0.16	3.94
co2_brz_tower-insitu_20_allvalid-40magl	NIES	Berezorechka, Russia	56.15°N	84.33°E	168	13167	515	0	2.1 - 18.5	1.04	-0.42	3.94
co2_brz_tower-insitu_20_allvalid-5magl	NIES	Berezorechka, Russia	56.15°N	84.33°E	168	13780	520	0	2.2 - 18.9	1.04	-0.22	4.01
co2_brz_tower-insitu_20_allvalid-80magl	NIES	Berezorechka, Russia	56.15°N	84.33°E	168	9082	326	0	1.9 - 19.0	1.06	-0.69	4.04
co2_bsc_surface-flask_1_representati	NOAA	Black Sea, Constanta, Romania	44.18°N	28.66°E	0	409	3	0	2.3 - 16.3	0.94	-5.69	7.99
co2_car_aircraft-pfp_1_allvalid_1000-2000masl	NOAA	Briggsdale, Colorado, United States	40.63°N	104.33°W	1783	48	1	0	1.2 - 4.2	0.67	-0.27	2.23
co2_car_aircraft-pfp_1_allvalid_2000 3000masl	NOAA	Briggsdale, Colorado, United States	40.63°N	104.33°W	2450	969	20	0	0.3 - 5.1	0.84	0.20	1.90
co2_car_aircraft-pfp_1_allvalid_3000-4000masl	NOAA	Briggsdale, Colorado, United States	40.63°N	104.33°W	3455	1124	47	0	0.2 - 2.3	1.18	0.10	0.98
co2_car_aircraft-pfp_1_allvalid_4000 5000masl	NOAA	Briggsdale, Colorado, United States	40.63°N	104.33°W	4497	1024	37	0	0.2 - 2.1	1.16	0.21	0.85
co2_car_aircraft-pfp_1_allvalid_5000-6000masl	NOAA	Briggsdale, Colorado, United States	40.63°N	104.33°W	5485	785	26	0	0.3 - 2.1	1.12	0.18	0.80

(table continued on next page)

Dataset	Lab.	Location	Latitude	Longitude	Elev. (m)	Used	Rej.	Unsampled	R (ppm)	χ^2	Bias (ppm)	SE (ppm)
co2_car_aircraft-pfp_1_allvalid_6000 7000masl	NOAA	Briggsdale, Colorado, United States	40.63°N	104.33°W	6438	773	32	0	0.5 - 2.0	1.19	0.35	0.76
co2_car_aircraft-pfp_1_allvalid_7000-8000masl	NOAA	Briggsdale, Colorado, United States	40.63°N	104.33°W	7473	764	9	0	0.3 - 2.2	1.16	0.29	0.77
co2_car_aircraft-pfp_1_allvalid_8000 9000masl	NOAA	Briggsdale, Colorado, United States	40.63°N	104.33°W	8219	170	2	0	0.2 - 1.7	1.16	0.12	0.76
co2_car_aircraft-pfp_1_allvalid_9000-10000masl	NOAA	Briggsdale, Colorado, United States	40.63°N	104.33°W	9140	1	0	0	0.7 - 0.7	1.52	0.46	NA
co2_car_aircraft-pfp_1_allvalid_1100 12000masl	NOAA	Briggsdale, Colorado, United States	40.63°N	104.33°W	11869	2	0	0	0.5 - 0.5	1.47	0.22	0.60
co2_cba_surface-flask_1_representative	NOAA	Cold Bay, Alaska, United States	55.21°N	162.72°W	21	1404	29	0	0.8 - 4.8	1.01	-0.93	1.68
co2_cba_surface-flask_4_representati	SIO	Cold Bay, Alaska, United States	55.21°N	162.72°W	21	399	15	0	0.6 - 6.5	1.16	-0.70	2.01
co2_cby_surface-insitu_6_allvalid	ECCC	Cambridge Bay, Nunavut Territory, Canada	69.13°N	105.06°W	35	8767	691	0	0.8 - 1.8	1.15	-0.03	1.22
co2_cdl_surface-insitu_6_allvalid	ECCC	Candle Lake, Saskatchewan, Canada	53.99°N	105.12°W	600	8503	316	0	1.6 - 4.3	0.93	0.09	2.54
co2_cfa_surface-flask_2_representative	CSIRO	Cape Ferguson, Queensland, Australia	19.28°S	147.06°E	2	583	0	0	0.1 - 2.4	0.51	-0.35	1.06
co2_cgo_surface-flask_1_representati	NOAA	Cape Grim, Tasmania, Australia	40.68°S	144.69°E	94	703	0	0	0.3 - 7.3	0.74	-0.18	0.64
co2_cgo_surface-flask_2_representative	CSIRO	Cape Grim, Tasmania, Australia	40.68°S	144.69°E	94	1228	4	0	0.3 - 4.0	0.47	-0.25	0.61
co2_cgo_surface-flask_4_representati	SIO	Cape Grim, Tasmania, Australia	40.68°S	144.69°E	94	411	7	0	0.3 - 1.2	0.86	-0.29	0.56
co2_chl_surface-insitu_6_allvalid	ECCC	Churchill, Manitoba, Canada	58.74°N	93.82°W	29	7617	695	0	1.1 - 3.0	1.04	-0.14	1.82

(table continued on next page)

Dataset	Lab.	Location	Latitude	Longitude	Elev. (m)	Used	Rej.	Unsampled	R (ppm)	χ^2	Bias (ppm)	SE (ppm)
co2_chm_surface-insitu_6_allvalid	ECCC	Chibougamau, Quebec, Canada	49.69°N	74.34°W	393	3400	172	0	1.9 - 3.5	1.15	0.05	2.48
co2_chr_surface-flask_1_representative	NOAA	Christmas Island, Republic of Kiribati	1.70°N	157.15°W	0	594	0	0	0.3 - 1.8	0.67	-0.20	0.60
co2_chr_surface-flask_426_represent	SIO_CO2	Christmas Island, Republic of Kiribati	1.70°N	157.15°W	0	273	2	0	0.5 - 2.2	0.83	-0.50	0.77
co2_cib_surface-flask_1_representative	NOAA	Centro de Investigacion de la Baja Atmosfera (CIBA), Spain	41.81°N	4.93°W	845	433	10	0	1.9 - 5.0	1.10	0.82	3.83
co2_cma_aircraft-pfp_1_allvalid_0-1000masl	NOAA	Offshore Cape May, New Jersey, United States	38.83°N	74.32°W	635	511	11	0	1.5 - 7.6	1.14	-0.29	3.09
co2_cma_aircraft-pfp_1_allvalid_1000-2000masl	NOAA	Offshore Cape May, New Jersey, United States	38.83°N	74.32°W	1536	311	6	0	0.7 - 5.0	0.98	-0.31	2.24
co2_cma_aircraft-pfp_1_allvalid_2000 3000masl	NOAA	Offshore Cape May, New Jersey, United States	38.83°N	74.32°W	2301	392	5	0	0.6 - 6.1	0.92	-0.19	1.80
co2_cma_aircraft-pfp_1_allvalid_3000-4000masl	NOAA	Offshore Cape May, New Jersey, United States	38.83°N	74.32°W	3441	358	13	0	0.3 - 2.8	1.10	0.18	1.21
co2_cma_aircraft-pfp_1_allvalid_4000 5000masl	NOAA	Offshore Cape May, New Jersey, United States	38.83°N	74.32°W	4190	189	7	0	0.3 - 2.7	1.20	-0.03	1.31
co2_cma_aircraft-pfp_1_allvalid_5000-6000masl	NOAA	Offshore Cape May, New Jersey, United States	38.83°N	74.32°W	5345	350	10	0	0.4 - 2.3	1.16	0.09	1.10
co2_cma_aircraft-pfp_1_allvalid_6000 7000masl	NOAA	Offshore Cape May, New Jersey, United States	38.83°N	74.32°W	6269	287	7	0	0.4 - 1.8	1.14	-0.09	1.02
co2_cma_aircraft-pfp_1_allvalid_7000-8000masl	NOAA	Offshore Cape May, New Jersey, United States	38.83°N	74.32°W	7725	274	4	0	0.4 - 1.8	1.10	0.28	0.88
co2_cma_aircraft-pfp_1_allvalid_8000 9000masl	NOAA	Offshore Cape May, New Jersey, United States	38.83°N	74.32°W	8048	33	0	0	0.6 - 1.4	0.76	-0.06	0.98

(table continued on next page)

Dataset	Lab.	Location	Latitude	Longitude	Elev. (m)	Used	Rej.	Unsampled	R (ppm)	χ^2	Bias (ppm)	SE (ppm)
co2_con_aircraft-flask_42_allvalid_0-1000masl	NIES	CONTRAIL (Comprehensive Observation Network for TRace gases by AIrLiner)	variable		820	1	0	0	0.1 - 0.1	0.78	-0.09	NA
co2_con_aircraft-flask_42_allvalid_10 2000masl	NIES	CONTRAIL (Comprehensive Observation Network for TRace gases by AIrLiner)	variable		1385	4	0	0	0.3 - 0.4	0.57	0.23	0.35
co2_con_aircraft-flask_42_allvalid_3000-4000masl	NIES	CONTRAIL (Comprehensive Observation Network for TRace gases by AIrLiner)	variable		3491	2	0	0	0.3 - 0.3	2.53	-0.37	0.34
co2_con_aircraft-flask_42_allvalid_50 6000masl	NIES	CONTRAIL (Comprehensive Observation Network for TRace gases by AIrLiner)	variable		5631	2	0	0	1.0 - 1.0	0.44	-0.02	0.83
co2_con_aircraft-flask_42_allvalid_6000-7000masl	NIES	CONTRAIL (Comprehensive Observation Network for TRace gases by AIrLiner)	variable		6391	4	0	0	0.1 - 2.7	1.56	1.14	1.64
co2_con_aircraft-flask_42_allvalid_80 9000masl	NIES	CONTRAIL (Comprehensive Observation Network for TRace gases by AIrLiner)	variable		8578	6	0	0	0.1 - 0.8	1.07	-0.06	0.46
co2_con_aircraft-flask_42_allvalid_9000-10000masl	NIES	CONTRAIL (Comprehensive Observation Network for TRace gases by AIrLiner)	variable		9648	305	5	1	0.0 - 2.2	1.18	0.13	0.71

(table continued on next page)

Dataset	Lab.	Location	Latitude	Longitude	Elev. (m)	Used	Rej.	Unsampled	R (ppm)	χ^2	Bias (ppm)	SE (ppm)
co2_con_aircraft-flask_42_allvalid_10 11000masl	NIES	CONTRAIL (Comprehensive Observation Network for TRace gases by AIrLiner)	variable		10672	1923	36	0	0.1 - 1.6	0.98	0.06	0.64
co2_con_aircraft-flask_42_allvalid_11000-12000masl	NIES	CONTRAIL (Comprehensive Observation Network for TRace gases by AIrLiner)	variable		11536	1023	16	0	0.1 - 1.7	0.89	0.13	0.72
co2_con_aircraft-flask_42_allvalid_12 13000masl	NIES	CONTRAIL (Comprehensive Observation Network for TRace gases by AIrLiner)	variable		12260	208	9	0	0.1 - 2.2	0.95	-0.08	0.97
co2_cps_surface-insitu_6_allvalid	ECCC	Chapais,Quebec, Canada	49.82°N	74.98°W	391	9312	707	0	1.4 - 3.6	1.41	0.25	2.73
co2_cpt_surface-flask_1_representati	NOAA	Cape Point, South Africa	34.35°S	18.49°E	230	221	2	0	0.2 - 1.3	0.44	0.18	0.43
co2_cpt_surface-insitu_36_marine	SAWS	Cape Point, South Africa	34.35°S	18.49°E	230	133019	5268	0	0.4 - 1.0	1.00	0.00	0.56
co2_crv_aircraft-pfp_1_allvalid_0-1000masl	NOAA	Carbon in Arctic Reservoirs Vulnerability Experiment (CARVE), United States	64.99°N	147.60°W	315	1390	50	0	0.9 - 50.8	0.93	-2.28	5.51
co2_crv_aircraft-pfp_1_allvalid_1000-2000masl	NOAA	Carbon in Arctic Reservoirs Vulnerability Experiment (CARVE), United States	64.99°N	147.60°W	1438	60	19	0	0.3 - 8.8	1.72	0.45	2.39
co2_crv_aircraft-pfp_1_allvalid_2000 3000masl	NOAA	Carbon in Arctic Reservoirs Vulnerability Experiment (CARVE), United States	64.99°N	147.60°W	2555	72	2	0	0.2 - 3.3	1.20	0.12	1.46

(table continued on next page)

Dataset	Lab.	Location	Latitude	Longitude	Elev. (m)	Used	Rej.	Unsampled	R (ppm)	χ^2	Bias (ppm)	SE (ppm)
co2_crv_aircraft-pfp_1_allvalid_3000-4000masl	NOAA	Carbon in Arctic Reservoirs Vulnerability Experiment (CARVE), United States	64.99°N	147.60°W	3390	48	6	0	0.4 - 1.9	1.98	0.25	1.09
co2_crv_aircraft-pfp_1_allvalid_4000 5000masl	NOAA	Carbon in Arctic Reservoirs Vulnerability Experiment (CARVE), United States	64.99°N	147.60°W	4518	27	4	0	0.2 - 1.9	2.33	0.51	1.12
co2_crv_aircraft-pfp_1_allvalid_5000-6000masl	NOAA	Carbon in Arctic Reservoirs Vulnerability Experiment (CARVE), United States	64.99°N	147.60°W	5269	267	14	0	0.1 - 2.2	1.12	0.20	1.42
co2_crv_surface-pfp_1_allvalid-32magl	NOAA	Carbon in Arctic Reservoirs Vulnerability Experiment (CARVE), United States	64.99°N	147.60°W	611	1332	10	0	1.9 - 9.2	0.66	-0.30	3.16
co2_crv_tower-insitu_1_allvalid-17magl	NOAA	Carbon in Arctic Reservoirs Vulnerability Experiment (CARVE), United States	64.99°N	147.60°W	611	9284	560	0	1.5 - 4.8	1.23	-0.19	3.04
co2_crv_tower-insitu_1_allvalid-32magl	NOAA	Carbon in Arctic Reservoirs Vulnerability Experiment (CARVE), United States	64.99°N	147.60°W	611	9590	700	0	1.5 - 5.6	1.26	-0.26	2.83
co2_crv_tower-insitu_1_allvalid-5magl	NOAA	Carbon in Arctic Reservoirs Vulnerability Experiment (CARVE), United States	64.99°N	147.60°W	611	9357	678	0	1.5 - 4.3	1.30	-0.10	3.16

(table continued on next page)

Dataset	Lab.	Location	Latitude	Longitude	Elev. (m)	Used	Rej.	Unsampled	R (ppm)	χ^2	Bias (ppm)	SE (ppm)
co2_crz_surface-flask_1_representati	NOAA	Crozet Island, France	46.43°S	51.85°E	197	756	0	0	0.1 - 0.5	0.82	0.01	0.32
co2_cya_surface-flask_2_representative	CSIRO	Casey, Antarctica, Australia	66.28°S	110.52°E	47	576	0	0	0.1 - 0.6	0.81	0.03	0.25
co2_dem_tower-insitu_20_allvalid-45magl	NIES	Demyanskoe, Russia	59.79°N	70.87°E	63	13827	497	0	1.7 - 5.0	1.19	-0.33	3.34
co2_dem_tower-insitu_20_allvalid-63magl	NIES	Demyanskoe, Russia	59.79°N	70.87°E	63	12988	505	0	1.7 - 5.1	1.20	-0.45	3.36
co2_dnd_aircraft-pfp_1_allvalid_0-1000masl	NOAA	Dahlen, North Dakota, United States	47.50°N	99.24°W	744	212	8	0	0.4 - 7.0	1.04	-0.49	3.69
co2_dnd_aircraft-pfp_1_allvalid_1000-2000masl	NOAA	Dahlen, North Dakota, United States	47.50°N	99.24°W	1507	281	24	0	0.2 - 5.5	1.10	-0.23	2.62
co2_dnd_aircraft-pfp_1_allvalid_2000 3000masl	NOAA	Dahlen, North Dakota, United States	47.50°N	99.24°W	2470	312	31	0	0.1 - 3.2	1.27	-0.18	1.42
co2_dnd_aircraft-pfp_1_allvalid_3000-4000masl	NOAA	Dahlen, North Dakota, United States	47.50°N	99.24°W	3530	248	14	0	0.4 - 2.9	1.57	0.03	1.27
co2_dnd_aircraft-pfp_1_allvalid_4000 5000masl	NOAA	Dahlen, North Dakota, United States	47.50°N	99.24°W	4466	187	7	0	0.5 - 3.8	1.14	0.07	1.31
co2_dnd_aircraft-pfp_1_allvalid_5000-6000masl	NOAA	Dahlen, North Dakota, United States	47.50°N	99.24°W	5508	216	9	0	0.3 - 2.4	1.15	0.13	1.05
co2_dnd_aircraft-pfp_1_allvalid_6000 7000masl	NOAA	Dahlen, North Dakota, United States	47.50°N	99.24°W	6481	196	4	0	0.3 - 2.3	1.37	0.11	1.04
co2_dnd_aircraft-pfp_1_allvalid_7000-8000masl	NOAA	Dahlen, North Dakota, United States	47.50°N	99.24°W	7474	201	8	0	0.2 - 1.9	1.28	0.22	0.99

(table continued on next page)

Dataset	Lab.	Location	Latitude	Longitude	Elev. (m)	Used	Rej.	Unsampled	R (ppm)	χ^2	Bias (ppm)	SE (ppm)
co2_dnd_aircraft-pfp_1_allvalid_8000-9000masl	NOAA	Dahlen, North Dakota, United States	47.50°N	99.24°W	8053	3	0	0	0.6 - 2.3	1.06	-1.37	1.02
co2_drp_shipboard-flask_1_representative	NOAA	Drake Passage	variable		Surface	243	5	0	0.1 - 1.2	0.65	0.03	0.40
co2_dsi_surface-flask_1_representati	NOAA	Dongsha Island, Taiwan	20.70°N	116.73°E	3	385	0	0	1.9 - 6.9	0.82	1.19	2.81
co2_egb_surface-insitu_6_allvalid	ECCC	Egbert, Ontario, Canada	44.23°N	79.78°W	251	13640	426	0	2.5 - 4.9	0.95	-0.21	3.71
co2_eic_surface-flask_1_representati	NOAA	Easter Island, Chile	27.16°S	109.43°W	47	540	2	0	0.5 - 1.7	1.02	0.36	0.97
co2_esp_aircraft-pfp_1_allvalid_0-1000masl	NOAA	Estevan Point, British Columbia, Canada	49.38°N	126.54°W	544	744	35	0	0.6 - 7.3	0.79	-0.76	3.02
co2_esp_aircraft-pfp_1_allvalid_1000-2000masl	NOAA	Estevan Point, British Columbia, Canada	49.38°N	126.54°W	1554	931	56	0	0.3 - 3.2	1.26	-0.11	1.40
co2_esp_aircraft-pfp_1_allvalid_2000-3000masl	NOAA	Estevan Point, British Columbia, Canada	49.38°N	126.54°W	2554	800	44	0	0.2 - 2.5	1.23	-0.05	1.22
co2_esp_aircraft-pfp_1_allvalid_3000-4000masl	NOAA	Estevan Point, British Columbia, Canada	49.38°N	126.54°W	3553	757	41	0	0.3 - 2.4	1.36	0.05	1.15
co2_esp_aircraft-pfp_1_allvalid_4000-5000masl	NOAA	Estevan Point, British Columbia, Canada	49.38°N	126.54°W	4511	662	22	0	0.5 - 2.4	1.26	0.08	1.16
co2_esp_aircraft-pfp_1_allvalid_5000-6000masl	NOAA	Estevan Point, British Columbia, Canada	49.38°N	126.54°W	5378	446	10	0	0.5 - 2.0	1.16	-0.00	1.10
co2_esp_surface-flask_2_representative	CSIRO	Estevan Point, British Columbia, Canada	49.38°N	126.54°W	7	17	2	0	0.2 - 7.1	0.48	-0.97	1.71
co2_esp_surface-insitu_6_allvalid	ECCC	Estevan Point, British Columbia, Canada	49.38°N	126.54°W	7	12971	393	0	1.6 - 3.8	0.84	-0.41	2.17
co2_est_surface-insitu_6_allvalid	ECCC	Esther, Alberta, Canada	51.67°N	110.21°W	707	11753	415	0	1.8 - 4.4	1.09	-0.19	2.78

(table continued on next page)

Dataset	Lab.	Location	Latitude	Longitude	Elev. (m)	Used	Rej.	Unsampled	R (ppm)	χ^2	Bias (ppm)	SE (ppm)
co2_etl_aircraft-pfp_1_allvalid_0-1000masl	NOAA	East Trout Lake, Saskatchewan, Canada	54.35°N	104.99°W	909	194	18	0	1.0 - 3.8	1.30	-0.34	2.23
co2_etl_aircraft-pfp_1_allvalid_1000-2000masl	NOAA	East Trout Lake, Saskatchewan, Canada	54.35°N	104.99°W	1511	741	40	0	0.7 - 3.1	1.26	-0.25	1.97
co2_etl_aircraft-pfp_1_allvalid_2000 3000masl	NOAA	East Trout Lake, Saskatchewan, Canada	54.35°N	104.99°W	2484	789	28	0	0.8 - 5.5	1.19	-0.26	1.49
co2_etl_aircraft-pfp_1_allvalid_3000-4000masl	NOAA	East Trout Lake, Saskatchewan, Canada	54.35°N	104.99°W	3501	279	11	0	0.5 - 2.1	1.23	-0.03	1.23
co2_etl_aircraft-pfp_1_allvalid_4000 5000masl	NOAA	East Trout Lake, Saskatchewan, Canada	54.35°N	104.99°W	4580	269	10	0	0.6 - 5.1	1.00	0.05	1.50
co2_etl_aircraft-pfp_1_allvalid_5000-6000masl	NOAA	East Trout Lake, Saskatchewan, Canada	54.35°N	104.99°W	5642	254	10	0	0.6 - 2.1	1.25	0.05	1.21
co2_etl_aircraft-pfp_1_allvalid_6000 7000masl	NOAA	East Trout Lake, Saskatchewan, Canada	54.35°N	104.99°W	6741	136	3	0	0.5 - 1.9	1.46	0.48	1.02
co2_etl_aircraft-pfp_1_allvalid_7000-8000masl	NOAA	East Trout Lake, Saskatchewan, Canada	54.35°N	104.99°W	7150	96	3	0	0.7 - 2.4	1.26	0.02	1.71
co2_etl_surface-insitu_6_allvalid	ECCC	East Trout Lake, Saskatchewan, Canada	54.35°N	104.99°W	493	17218	1007	0	1.6 - 3.9	1.07	-0.14	2.45
co2_fsd_surface-insitu_6_allvalid	ECCC	Fraserdale, Canada	49.88°N	81.57°W	210	21843	999	0	1.7 - 4.5	1.05	0.03	2.68
co2_ftl_aircraft-pfp_1_allvalid_1000 2000masl	NOAA	Fortaleza, Brazil	3.52°S	38.28°W	1810	10	0	0	0.1 - 1.2	1.42	-0.46	1.09
co2_ftl_aircraft-pfp_1_allvalid_2000-3000masl	NOAA	Fortaleza, Brazil	3.52°S	38.28°W	2498	23	0	0	0.4 - 2.2	0.97	-0.53	1.28

(table continued on next page)

Dataset	Lab.	Location	Latitude	Longitude	Elev. (m)	Used	Rej.	Unsampled	R (ppm)	χ^2	Bias (ppm)	SE (ppm)
co2_ftl_aircraft-pfp_1_allvalid_3000 4000masl	NOAA	Fortaleza, Brazil	3.52°S	38.28°W	3479	37	0	0	0.3 - 2.1	1.24	0.04	1.39
co2_ftl_aircraft-pfp_1_allvalid_4000-5000masl	NOAA	Fortaleza, Brazil	3.52°S	38.28°W	4267	7	0	0	0.5 - 2.7	1.12	0.07	1.64
co2_ftw_shipboard-insitu_20_allvalid	NIES	Fujitrans World (M/S Fujitrans World of Kagoshima Shipping Co., Ltd.)	variable		Surface	69451	2688	0	0.1 - 19.6	0.85	-0.24	1.51
co2_ftws_shipboard-insitu_20_allvalid	NIES	Fujitrans World - Southeast Asia Route (M/S Fujitrans World of Kagoshima Shipping Co., Ltd.)	variable		Surface	227646	6095	0	0.1 - 32.5	0.69	-0.86	2.83
co2_fwi_aircraft-pfp_1_allvalid_0-1000masl	NOAA	Fairchild, Wisconsin, United States	44.66°N	90.96°W	623	9	0	0	3.6 - 10.7	0.54	-1.50	5.32
co2_fwi_aircraft-pfp_1_allvalid_1000-2000masl	NOAA	Fairchild, Wisconsin, United States	44.66°N	90.96°W	1577	47	4	0	0.5 - 8.2	1.22	-0.54	2.78
co2_fwi_aircraft-pfp_1_allvalid_2000 3000masl	NOAA	Fairchild, Wisconsin, United States	44.66°N	90.96°W	2535	18	0	0	0.3 - 2.8	1.02	-0.37	1.95
co2_fwi_aircraft-pfp_1_allvalid_3000-4000masl	NOAA	Fairchild, Wisconsin, United States	44.66°N	90.96°W	3518	48	7	0	0.2 - 2.9	1.32	0.04	1.68
co2_fwi_aircraft-pfp_1_allvalid_4000 5000masl	NOAA	Fairchild, Wisconsin, United States	44.66°N	90.96°W	4570	28	2	0	0.2 - 2.1	1.30	0.32	1.03
co2_fwi_aircraft-pfp_1_allvalid_5000-6000masl	NOAA	Fairchild, Wisconsin, United States	44.66°N	90.96°W	5523	41	1	0	0.2 - 9.9	1.08	0.72	2.37
co2_fwi_aircraft-pfp_1_allvalid_6000 7000masl	NOAA	Fairchild, Wisconsin, United States	44.66°N	90.96°W	6504	30	5	0	0.1 - 2.2	1.65	0.37	1.11

(table continued on next page)

Dataset	Lab.	Location	Latitude	Longitude	Elev. (m)	Used	Rej.	Unsampled	R (ppm)	χ^2	Bias (ppm)	SE (ppm)
co2_fwi_aircraft-pfp_1_allvalid_7000-8000masl	NOAA	Fairchild, Wisconsin, United States	44.66°N	90.96°W	7484	39	0	0	0.5 - 2.2	1.26	0.13	1.15
co2_gmi_surface-flask_1_representati	NOAA	Mariana Islands, Guam	13.39°N	144.66°E	0	1072	21	0	0.3 - 1.4	0.89	0.07	0.78
co2_gw_shipboard-insitu_20_allvalid	NIES	Golden Wattle (M/S Alligator Hope of Mitsui O.S.K. Lines, Ltd.)	variable		Surface	13101	877	0	0.1 - 58.7	0.96	-0.27	1.56
co2_haa_aircraft-pfp_1_allvalid_0-1000masl	NOAA	Molokai Island, Hawaii, United States	21.23°N	158.95°W	879	20	2	0	0.2 - 1.2	1.75	0.36	0.63
co2_haa_aircraft-pfp_1_allvalid_1000-2000masl	NOAA	Molokai Island, Hawaii, United States	21.23°N	158.95°W	1598	206	14	0	0.2 - 1.0	1.28	0.17	0.70
co2_haa_aircraft-pfp_1_allvalid_2000 3000masl	NOAA	Molokai Island, Hawaii, United States	21.23°N	158.95°W	2524	196	15	0	0.2 - 1.1	1.35	0.08	0.73
co2_haa_aircraft-pfp_1_allvalid_3000-4000masl	NOAA	Molokai Island, Hawaii, United States	21.23°N	158.95°W	3488	217	8	0	0.2 - 1.1	1.21	0.07	0.71
co2_haa_aircraft-pfp_1_allvalid_4000 5000masl	NOAA	Molokai Island, Hawaii, United States	21.23°N	158.95°W	4532	251	7	0	0.1 - 1.2	1.27	0.10	0.80
co2_haa_aircraft-pfp_1_allvalid_5000-6000masl	NOAA	Molokai Island, Hawaii, United States	21.23°N	158.95°W	5440	194	3	0	0.1 - 1.1	1.26	0.07	0.75
co2_haa_aircraft-pfp_1_allvalid_6000 7000masl	NOAA	Molokai Island, Hawaii, United States	21.23°N	158.95°W	6490	202	1	0	0.2 - 1.5	1.23	0.21	0.94
co2_haa_aircraft-pfp_1_allvalid_7000-8000masl	NOAA	Molokai Island, Hawaii, United States	21.23°N	158.95°W	7471	114	2	0	0.2 - 2.1	0.91	0.24	1.30
co2_haa_aircraft-pfp_1_allvalid_8000 9000masl	NOAA	Molokai Island, Hawaii, United States	21.23°N	158.95°W	8041	61	0	0	0.2 - 3.1	1.06	-0.10	0.86

(table continued on next page)

Dataset	Lab.	Location	Latitude	Longitude	Elev. (m)	Used	Rej.	Unsampled	R (ppm)	χ^2	Bias (ppm)	SE (ppm)
co2_hba_surface-flask_1_representative	NOAA	Halley Station, Antarctica, United Kingdom	75.61°S	26.21°W	30	726	0	0	0.0 - 0.6	1.01	0.05	0.18
co2_hdp_surface-insitu_3_nonlocal	NCAR	Hidden Peak (Snowbird), Utah, United States	40.56°N	111.65°W	3351	55241	1975	0	0.8 - 2.0	1.18	-0.36	1.19
co2_hfm_aircraft-pfp_1_allvalid_0-1000masl	NOAA	Harvard Forest, Massachusetts, United States	42.54°N	72.17°W	761	146	8	0	0.3 - 7.0	0.76	-0.40	3.46
co2_hfm_aircraft-pfp_1_allvalid_1000 2000masl	NOAA	Harvard Forest, Massachusetts, United States	42.54°N	72.17°W	1532	253	10	0	1.0 - 10.7	0.97	-0.20	2.53
co2_hfm_aircraft-pfp_1_allvalid_2000-3000masl	NOAA	Harvard Forest, Massachusetts, United States	42.54°N	72.17°W	2452	174	13	0	0.5 - 8.9	1.46	-0.19	2.00
co2_hfm_aircraft-pfp_1_allvalid_3000 4000masl	NOAA	Harvard Forest, Massachusetts, United States	42.54°N	72.17°W	3432	149	8	0	0.3 - 6.2	1.29	0.11	1.27
co2_hfm_aircraft-pfp_1_allvalid_4000-5000masl	NOAA	Harvard Forest, Massachusetts, United States	42.54°N	72.17°W	4563	181	3	0	0.3 - 2.5	1.34	0.17	1.03
co2_hfm_aircraft-pfp_1_allvalid_5000 6000masl	NOAA	Harvard Forest, Massachusetts, United States	42.54°N	72.17°W	5483	196	4	0	0.3 - 1.7	1.26	0.27	0.95
co2_hfm_aircraft-pfp_1_allvalid_6000-7000masl	NOAA	Harvard Forest, Massachusetts, United States	42.54°N	72.17°W	6426	145	3	0	0.3 - 2.5	1.62	0.42	0.94
co2_hfm_aircraft-pfp_1_allvalid_7000 8000masl	NOAA	Harvard Forest, Massachusetts, United States	42.54°N	72.17°W	7388	167	7	0	0.2 - 6.5	1.14	0.44	2.33
co2_hfm_aircraft-pfp_1_allvalid_8000-9000masl	NOAA	Harvard Forest, Massachusetts, United States	42.54°N	72.17°W	8031	2	0	0	1.7 - 1.7	0.31	-1.11	1.31
co2_hil_aircraft-pfp_1_allvalid_0-1000masl	NOAA	Homer, Illinois, United States	40.07°N	87.91°W	612	174	6	0	0.9 - 8.0	1.13	-0.67	3.40

(table continued on next page)

Dataset	Lab.	Location	Latitude	Longitude	Elev. (m)	Used	Rej.	Unsampled	R (ppm)	χ^2	Bias (ppm)	SE (ppm)
co2_hil_aircraft-pfp_1_allvalid_1000-2000masl	NOAA	Homer, Illinois, United States	40.07°N	87.91°W	1554	436	16	0	0.7 - 6.3	1.05	-0.25	2.58
co2_hil_aircraft-pfp_1_allvalid_2000 3000masl	NOAA	Homer, Illinois, United States	40.07°N	87.91°W	2537	255	13	0	0.1 - 4.8	0.90	-0.45	1.77
co2_hil_aircraft-pfp_1_allvalid_3000-4000masl	NOAA	Homer, Illinois, United States	40.07°N	87.91°W	3503	454	15	0	0.3 - 3.0	1.05	-0.27	1.42
co2_hil_aircraft-pfp_1_allvalid_4000 5000masl	NOAA	Homer, Illinois, United States	40.07°N	87.91°W	4545	295	9	0	0.2 - 2.5	1.25	-0.13	1.22
co2_hil_aircraft-pfp_1_allvalid_5000-6000masl	NOAA	Homer, Illinois, United States	40.07°N	87.91°W	5513	389	7	0	0.2 - 2.0	1.20	-0.15	1.20
co2_hil_aircraft-pfp_1_allvalid_6000 7000masl	NOAA	Homer, Illinois, United States	40.07°N	87.91°W	6520	323	22	0	0.2 - 2.3	1.15	0.02	1.19
co2_hil_aircraft-pfp_1_allvalid_7000-8000masl	NOAA	Homer, Illinois, United States	40.07°N	87.91°W	7484	357	10	0	0.4 - 2.5	1.06	-0.04	1.10
co2_hil_aircraft-pfp_1_allvalid_8000 9000masl	NOAA	Homer, Illinois, United States	40.07°N	87.91°W	8042	32	0	0	0.7 - 3.1	1.20	-1.15	1.78
co2_hpb_surface-flask_1_representative	NOAA	Hohenpeissenberg, Germany	47.80°N	11.02°E	936	600	12	0	3.6 - 14.5	1.08	2.03	6.81
co2_hun_surface-flask_1_representati	NOAA	Hegyhatsal, Hungary	46.95°N	16.65°E	248	937	10	0	2.1 - 9.9	0.79	-2.01	5.47
co2_ice_surface-flask_1_representative	NOAA	Storhofdi, Vestmannaeyjar, Iceland	63.40°N	20.29°W	118	538	23	0	0.4 - 4.2	1.03	-0.45	1.07
co2_igr_tower-insitu_20_allvalid-24magl	NIES	Igrim, Russia	63.19°N	64.42°E	9	10627	304	0	3.7 - 6.0	0.92	-1.96	4.43
co2_igr_tower-insitu_20_allvalid-47magl	NIES	Igrim, Russia	63.19°N	64.42°E	9	10515	274	0	3.9 - 8.4	0.68	-1.86	5.91

(table continued on next page)

Dataset	Lab.	Location	Latitude	Longitude	Elev. (m)	Used	Rej.	Unsampled	R (ppm)	χ^2	Bias (ppm)	SE (ppm)
co2_inu_surface-insitu_6_allvalid	ECCC	Inuvik,Northwest Territories, Canada	68.32°N	133.53°W	113	10857	591	0	1.9 - 3.7	1.05	-0.26	2.31
co2_inx_aircraft-pfp_1_allvalid_0-1000masl	NOAA	INFLUX (Indianapolis Flux Experiment), United States	39.58°N	86.42°W	652	171	3	0	1.1 - 5.8	0.81	-2.14	3.81
co2_inx_aircraft-pfp_1_allvalid_1000 2000masl	NOAA	INFLUX (Indianapolis Flux Experiment), United States	39.58°N	86.42°W	1354	57	3	0	0.8 - 5.2	1.23	-0.49	2.62
co2_inx_aircraft-pfp_1_allvalid_2000-3000masl	NOAA	INFLUX (Indianapolis Flux Experiment), United States	39.58°N	86.42°W	2501	21	0	0	0.2 - 2.1	0.92	0.26	1.53
co2_inx_aircraft-pfp_1_allvalid_3000 4000masl	NOAA	INFLUX (Indianapolis Flux Experiment), United States	39.58°N	86.42°W	3226	9	1	0	0.2 - 1.0	2.72	0.24	0.67
co2_izo_surface-insitu_27_allvalid	AEMET	Izana, Tenerife, Canary Islands, Spain	28.31°N	16.50°W	2373	55987	1830	14813	0.6 - 1.0	1.08	0.18	0.75
co2_jfj_surface-insitu_442_allvalid-5magl	ICOS-ATC	Jungfraujoch, Switzerland	46.55°N	7.99°E	3570	5142	22	0	0.9 - 3.9	0.44	0.15	1.50
co2_jfj_surface-insitu_49_allvalid	KUP	Jungfraujoch, Switzerland	46.55°N	7.99°E	3570	19147	331	0	1.5 - 4.5	0.66	0.09	1.85
co2_jfj_surface-insitu_5_allvalid	EMPA	Jungfraujoch, Switzerland	46.55°N	7.99°E	3570	7744	109	0	0.8 - 5.3	0.61	0.17	1.68
co2_key_surface-flask_1_representative	NOAA	Key Biscayne, Florida, United States	25.67°N	80.16°W	1	649	13	0	1.0 - 2.5	0.64	0.21	1.75
co2_krs_tower-insitu_20_allvalid-35magl	NIES	Karasevoe, Russia	58.25°N	82.42°E	76	13234	615	0	1.8 - 5.8	1.14	-0.39	3.77
co2_krs_tower-insitu_20_allvalid-67magl	NIES	Karasevoe, Russia	58.25°N	82.42°E	76	12452	611	0	1.8 - 5.7	1.16	-0.45	3.69
co2_kum_surface-flask_1_representati	NOAA	Cape Kumukahi, Hawaii, United States	19.56°N	154.89°W	8	2098	14	0	0.3 - 3.4	0.58	-0.21	0.95
co2_kum_surface-flask_4_representative	SIO	Cape Kumukahi, Hawaii, United States	19.56°N	154.89°W	8	664	25	0	0.4 - 1.3	0.89	-0.18	1.04

(table continued on next page)

Dataset	Lab.	Location	Latitude	Longitude	Elev. (m)	Used	Rej.	Unsampled	R (ppm)	χ^2	Bias (ppm)	SE (ppm)
co2_kum_surface-flask_426_represent	SIO_CO2	Cape Kumukahi, Hawaii, United States	19.56°N	154.89°W	8	699	15	0	0.3 - 1.6	0.94	-0.17	0.91
co2_kzd_surface-flask_1_representative	NOAA	Sary Taukum, Kazakhstan	44.08°N	76.87°E	595	414	6	0	0.5 - 8.6	0.74	-1.16	3.78
co2_kzm_surface-flask_1_representati	NOAA	Plateau Assy, Kazakhstan	43.25°N	77.88°E	2519	361	5	0	1.2 - 4.1	0.96	-0.09	2.61
co2_lef_aircraft-pfp_1_allvalid_0-1000masl	NOAA	Park Falls, Wisconsin, United States	45.95°N	90.27°W	773	618	39	0	0.9 - 6.7	1.00	-0.39	2.97
co2_lef_aircraft-pfp_1_allvalid_1000 2000masl	NOAA	Park Falls, Wisconsin, United States	45.95°N	90.27°W	1522	1196	50	0	0.4 - 6.3	0.99	-0.21	2.65
co2_lef_aircraft-pfp_1_allvalid_2000-3000masl	NOAA	Park Falls, Wisconsin, United States	45.95°N	90.27°W	2464	939	35	0	0.5 - 4.2	0.88	-0.27	1.80
co2_lef_aircraft-pfp_1_allvalid_3000 4000masl	NOAA	Park Falls, Wisconsin, United States	45.95°N	90.27°W	3502	1085	18	0	0.3 - 3.3	0.96	-0.19	1.48
co2_lef_aircraft-pfp_1_allvalid_4000-5000masl	NOAA	Park Falls, Wisconsin, United States	45.95°N	90.27°W	4016	3	0	0	1.8 - 1.8	0.43	-0.91	1.33
co2_lef_tower-insitu_1_allvalid-11magl	NOAA	Park Falls, Wisconsin, United States	45.95°N	90.27°W	472	10478	370	0	2.1 - 4.7	0.94	-0.07	3.41
co2_lef_tower-insitu_1_allvalid-122magl	NOAA	Park Falls, Wisconsin, United States	45.95°N	90.27°W	472	25084	1266	0	1.9 - 5.0	1.02	-0.08	3.56
co2_lef_tower-insitu_1_allvalid-244magl	NOAA	Park Falls, Wisconsin, United States	45.95°N	90.27°W	472	62630	2346	0	2.0 - 7.4	0.94	-0.25	3.59
co2_lef_tower-insitu_1_allvalid-30magl	NOAA	Park Falls, Wisconsin, United States	45.95°N	90.27°W	472	24555	1190	0	2.0 - 5.3	1.02	0.04	3.73
co2_lef_tower-insitu_1_allvalid-396magl	NOAA	Park Falls, Wisconsin, United States	45.95°N	90.27°W	472	150691	6560	0	1.9 - 13.8	0.99	-0.05	3.41

(table continued on next page)

Dataset	Lab.	Location	Latitude	Longitude	Elev. (m)	Used	Rej.	Unsampled	R (ppm)	χ^2	Bias (ppm)	SE (ppm)
co2_lef_tower-insitu_1_allvalid-76magl	NOAA	Park Falls, Wisconsin, United States	45.95°N	90.27°W	472	10330	450	0	2.0 - 4.4	0.96	-0.34	3.30
co2_lew_surface-pfp_1_allvalid-95magl	NOAA	Lewisburg, Pennsylvania, United States	40.94°N	76.88°W	166	688	19	0	3.1 - 9.4	0.74	-1.73	5.53
co2_ljo_surface-flask_426_representative	SIO_CO2	La Jolla, California, United States	32.87°N	117.26°W	10	448	1	0	1.0 - 16.0	0.40	1.91	2.61
co2_llb_surface-flask_1_representati	NOAA	Lac La Biche, Alberta, Canada	54.95°N	112.47°W	540	142	3	0	2.0 - 18.0	0.57	-1.44	4.66
co2_llb_surface-insitu_6_allvalid	ECCC	Lac La Biche, Alberta, Canada	54.95°N	112.47°W	540	13413	384	0	2.0 - 6.5	1.00	-0.61	3.44
co2_lmp_surface-flask_1_representati	NOAA	Lampedusa, Italy	35.52°N	12.63°E	45	559	10	0	0.9 - 2.5	1.07	-0.12	1.73
co2_lut_surface-insitu_44_allvalid	RUG	Lutjewad, Netherlands	53.40°N	6.35°E	1	12528	389	0	3.5 - 11.4	0.75	-2.18	6.07
co2_maa_surface-flask_2_representati	CSIRO	Mawson Station, Antarctica, Australia	67.62°S	62.87°E	32	664	0	0	0.1 - 1.2	0.76	0.03	0.23
co2_mbo_surface-pfp_1_allvalid-11magl	NOAA	Mt. Bachelor Observatory, United States	43.98°N	121.69°W	2731	1465	23	0	0.9 - 4.6	0.72	-0.24	1.62
co2_mex_surface-flask_1_representati	NOAA	High Altitude Global Climate Observation Center, Mexico	18.98°N	97.31°W	4464	359	4	0	0.8 - 3.2	0.97	0.80	1.40
co2_mhd_surface-flask_1_representative	NOAA	Mace Head, County Galway, Ireland	53.33°N	9.90°W	5	787	16	0	0.6 - 4.6	0.80	-0.34	1.16
co2_mhd_surface-insitu_11_representa	LSCE	Mace Head, County Galway, Ireland	53.33°N	9.90°W	5	34349	2401	0	0.6 - 2.2	1.37	-0.06	0.90
co2_mid_surface-flask_1_representative	NOAA	Sand Island, Midway, United States	28.21°N	177.38°W	11	868	20	0	0.3 - 1.5	1.13	0.34	1.00
co2_mkn_surface-flask_1_representati	NOAA	Mt. Kenya, Kenya	0.06°S	37.30°E	3644	127	0	0	0.4 - 3.3	1.10	1.66	1.89
co2_mlo_surface-flask_1_representative	NOAA	Mauna Loa, Hawaii, United States	19.54°N	155.58°W	3397	1962	30	0	0.4 - 2.6	0.61	0.09	0.53
co2_mlo_surface-flask_2_representati	CSIRO	Mauna Loa, Hawaii, United States	19.54°N	155.58°W	3397	976	1	0	0.5 - 3.3	0.25	0.24	0.56

(table continued on next page)

Dataset	Lab.	Location	Latitude	Longitude	Elev. (m)	Used	Rej.	Unsampled	R (ppm)	χ^2	Bias (ppm)	SE (ppm)
co2_mlo_surface-flask_4_representative	SIO	Mauna Loa, Hawaii, United States	19.54°N	155.58°W	3397	761	13	0	0.3 - 1.4	0.76	0.12	0.57
co2_mlo_surface-flask_426_represent	SIO_CO2	Mauna Loa, Hawaii, United States	19.54°N	155.58°W	3397	956	30	0	0.4 - 1.4	1.02	0.08	0.54
co2_mlo_surface-insitu_1_allvalid	NOAA	Mauna Loa, Hawaii, United States	19.54°N	155.58°W	3397	38188	0	0	0.4 - 0.7	1.34	0.14	0.52
co2_mqa_surface-flask_2_representati	CSIRO	Macquarie Island, Australia	54.48°S	158.97°E	6	733	0	0	0.2 - 1.0	0.58	0.21	0.36
co2_mvy_surface-insitu_1_allvalid	NOAA	Marthas Vineyard, Massachusetts, United States	41.33°N	70.57°W	0	63052	0	0	2.5 - 8.2	1.10	-0.21	4.28
co2_mwo_surface-pfp_1_allvalid-46magl	NOAA	Mt. Wilson Observatory, United States	34.22°N	118.06°W	1728	3926	76	0	1.3 - 17.3	0.68	-2.80	5.35
co2_nat_surface-flask_1_representative	NOAA	Farol De Mae Luiza Lighthouse, Brazil	5.80°S	35.19°W	50	310	3	0	0.8 - 1.6	1.03	-0.68	1.02
co2_nat_surface-flask_26_marine	IPEN	Farol De Mae Luiza Lighthouse, Brazil	5.80°S	35.19°W	50	194	1	0	0.7 - 2.0	0.95	-0.81	1.13
co2_nha_aircraft-pfp_1_allvalid_0-1000masl	NOAA	Offshore Portsmouth, New Hampshire (Isles of Shoals), United States	42.95°N	70.63°W	612	762	22	0	1.4 - 6.6	1.11	-0.16	2.72
co2_nha_aircraft-pfp_1_allvalid_1000 2000masl	NOAA	Offshore Portsmouth, New Hampshire (Isles of Shoals), United States	42.95°N	70.63°W	1494	595	21	0	1.0 - 4.0	1.06	-0.08	2.10
co2_nha_aircraft-pfp_1_allvalid_2000-3000masl	NOAA	Offshore Portsmouth, New Hampshire (Isles of Shoals), United States	42.95°N	70.63°W	2407	576	25	0	0.3 - 3.7	1.00	-0.21	1.79
co2_nha_aircraft-pfp_1_allvalid_3000 4000masl	NOAA	Offshore Portsmouth, New Hampshire (Isles of Shoals), United States	42.95°N	70.63°W	3482	480	24	0	0.4 - 3.6	1.17	0.04	1.33

(table continued on next page)

Dataset	Lab.	Location	Latitude	Longitude	Elev. (m)	Used	Rej.	Unsampled	R (ppm)	χ^2	Bias (ppm)	SE (ppm)
co2_nha_aircraft-pfp_1_allvalid_4000-5000masl	NOAA	Offshore Portsmouth, New Hampshire (Isles of Shoals), United States	42.95°N	70.63°W	4410	285	11	0	0.4 - 2.1	1.23	-0.09	1.19
co2_nha_aircraft-pfp_1_allvalid_5000 6000masl	NOAA	Offshore Portsmouth, New Hampshire (Isles of Shoals), United States	42.95°N	70.63°W	5368	360	15	0	0.3 - 3.5	1.10	-0.01	1.26
co2_nha_aircraft-pfp_1_allvalid_6000-7000masl	NOAA	Offshore Portsmouth, New Hampshire (Isles of Shoals), United States	42.95°N	70.63°W	6304	268	6	0	0.3 - 3.6	1.21	-0.05	1.27
co2_nha_aircraft-pfp_1_allvalid_7000 8000masl	NOAA	Offshore Portsmouth, New Hampshire (Isles of Shoals), United States	42.95°N	70.63°W	7666	287	6	0	0.5 - 2.0	1.31	0.28	1.11
co2_nha_aircraft-pfp_1_allvalid_8000-9000masl	NOAA	Offshore Portsmouth, New Hampshire (Isles of Shoals), United States	42.95°N	70.63°W	8039	4	1	0	0.4 - 0.5	1.01	-0.60	0.71
co2_nmb_surface-flask_1_representati	NOAA	Gobabeb, Namibia	23.58°S	15.03°E	456	485	14	0	0.5 - 1.8	0.94	0.05	0.98
co2_noy_tower-insitu_20_allvalid-21magl	NIES	Noyabrsk, Russia	63.43°N	75.78°E	108	9349	414	0	1.5 - 5.2	1.12	-0.01	3.15
co2_noy_tower-insitu_20_allvalid-43magl	NIES	Noyabrsk, Russia	63.43°N	75.78°E	108	9714	426	0	1.6 - 5.4	1.13	-0.14	3.13
co2_nwr_surface-flask_1_representative	NOAA	Niwot Ridge, Colorado, United States	40.05°N	105.59°W	3523	1265	4	0	0.5 - 8.3	0.53	0.37	1.29
co2_nwr_surface-insitu_3_nonlocal	NCAR	Niwot Ridge, Colorado, United States	40.05°N	105.59°W	3523	62986	2084	0	0.8 - 4.5	0.97	-0.04	1.40
co2_nwr_surface-pfp_1_allvalid-3magl	NOAA	Niwot Ridge, Colorado, United States	40.05°N	105.59°W	3523	3212	56	0	0.7 - 10.5	0.52	0.13	1.81

(table continued on next page)

Dataset	Lab.	Location	Latitude	Longitude	Elev. (m)	Used	Rej.	Unsampled	R (ppm)	χ^2	Bias (ppm)	SE (ppm)
co2_obn_surface-flask_1_representati	NOAA	Obninsk, Russia	55.11°N	36.60°E	183	173	3	0	2.6 - 12.1	0.56	-0.18	5.36
co2_ofr_surface-insitu_68_allhours	OSU	Fir, Oregon, United States	44.65°N	123.55°W	263	55301	24	0	3.5 - 33.2	0.21	-1.77	6.57
co2_omp_surface-insitu_68_allhours	OSU	Marys Peak, Oregon, United States	44.50°N	123.55°W	1249	112852	1531	0	1.2 - 18.6	0.64	0.76	3.03
co2_omt_surface-insitu_68_allhours	OSU	Metolius, Oregon, United States	44.45°N	121.56°W	1255	74274	854	0	1.7 - 16.8	0.57	1.20	3.89
co2_ong_surface-insitu_68_allhours	OSU	Burns, Oregon, United States	43.47°N	119.69°W	1398	80687	595	0	1.2 - 27.1	0.46	-0.04	3.19
co2_owa_surface-insitu_68_allhours	OSU	Walton, Oregon, United States	44.07°N	123.63°W	715	37015	847	0	2.0 - 6.6	0.96	-1.03	3.35
co2_oxk_surface-flask_1_representati	NOAA	Ochsenkopf, Germany	50.03°N	11.81°E	1022	465	7	0	1.4 - 5.7	0.94	-0.97	3.94
co2_oyq_surface-insitu_68_allhours	OSU	Yaquina Head, Oregon, United States	44.67°N	124.07°W	116	33451	46	0	1.7 - 34.5	0.26	-2.17	4.05
co2_pal_surface-flask_1_representati	NOAA	Pallas-Sammaltunturi, GAW Station, Finland	67.97°N	24.12°E	565	756	8	0	1.3 - 14.8	0.52	-0.32	2.32
co2_pal_surface-insitu_30_marine	FMI	Pallas-Sammaltunturi, GAW Station, Finland	67.97°N	24.12°E	565	22767	293	0	1.0 - 3.0	0.81	-0.19	1.14
co2_pal_surface-insitu_30_nonlocal	FMI	Pallas-Sammaltunturi, GAW Station, Finland	67.97°N	24.12°E	565	94896	2294	0	1.1 - 5.6	0.85	-0.17	1.94
co2_pfa_aircraft-pfp_1_allvalid_0-1000masl	NOAA	Poker Flat, Alaska, United States	64.90°N	148.76°W	551	542	56	0	1.1 - 6.8	1.03	-0.52	3.26
co2_pfa_aircraft-pfp_1_allvalid_1000-2000masl	NOAA	Poker Flat, Alaska, United States	64.90°N	148.76°W	1515	578	46	0	0.4 - 7.1	1.19	-0.34	1.66
co2_pfa_aircraft-pfp_1_allvalid_2000-3000masl	NOAA	Poker Flat, Alaska, United States	64.90°N	148.76°W	2513	647	41	0	0.2 - 4.0	1.33	-0.38	1.22
co2_pfa_aircraft-pfp_1_allvalid_3000-4000masl	NOAA	Poker Flat, Alaska, United States	64.90°N	148.76°W	3467	647	30	0	0.2 - 2.8	1.42	-0.04	1.20

(table continued on next page)

Dataset	Lab.	Location	Latitude	Longitude	Elev. (m)	Used	Rej.	Unsampled	R (ppm)	χ^2	Bias (ppm)	SE (ppm)
co2_pfa_aircraft-pfp_1_allvalid_4000-5000masl	NOAA	Poker Flat, Alaska, United States	64.90°N	148.76°W	4506	555	51	0	0.3 - 2.2	1.37	0.05	1.05
co2_pfa_aircraft-pfp_1_allvalid_5000 6000masl	NOAA	Poker Flat, Alaska, United States	64.90°N	148.76°W	5446	524	20	0	0.3 - 2.4	1.34	0.06	1.16
co2_pfa_aircraft-pfp_1_allvalid_6000-7000masl	NOAA	Poker Flat, Alaska, United States	64.90°N	148.76°W	6449	511	16	0	0.2 - 2.6	1.37	0.23	1.28
co2_pfa_aircraft-pfp_1_allvalid_7000 8000masl	NOAA	Poker Flat, Alaska, United States	64.90°N	148.76°W	7209	229	6	0	0.1 - 2.7	1.13	0.18	1.53
co2_poc_shipboard-flask_1_representative	NOAA	Pacific Ocean	variable		Surface	2089	74	0	0.0 - 5.3	0.98	-0.06	0.57
co2_prs_surface-insitu_21_allvalid	RSE	Plateau Rosa Station, Italy	45.93°N	7.70°E	3480	14434	426	0	1.1 - 2.9	0.99	0.14	1.53
co2_psa_surface-flask_1_representative	NOAA	Palmer Station, Antarctica, United States	64.77°S	64.05°W	10	937	0	0	0.1 - 0.9	0.58	-0.03	0.27
co2_psa_surface-flask_4_representati	SIO	Palmer Station, Antarctica, United States	64.77°S	64.05°W	10	440	6	0	0.1 - 1.0	0.46	-0.02	0.29
co2_pta_surface-flask_1_representative	NOAA	Point Arena, California, United States	38.95°N	123.74°W	17	374	2	0	2.8 - 10.8	0.56	-2.34	4.87
co2_px_shipboard-insitu_20_allvalid	NIES	Pyxis (M/S Pyxis of Toyofuji Shipping Co., Ltd.)	variable		Surface	317360	24199	0	0.1 - 52.2	1.07	-0.03	1.51
co2_rk1_surface-flask_426_representative	SIO_CO2	Kermadec Island, Raoul Island	29.20°S	177.90°W	2	86	6	0	0.2 - 1.2	0.91	-0.25	0.68
co2_rpb_surface-flask_1_representati	NOAA	Ragged Point, Barbados	13.16°N	59.43°W	15	922	13	0	0.2 - 1.7	1.01	0.06	0.73
co2_rta_aircraft-pfp_1_allvalid_0-1000masl	NOAA	Rarotonga, Cook Islands	21.25°S	159.83°W	654	103	2	0	0.3 - 0.7	0.98	0.16	0.46

(table continued on next page)

Dataset	Lab.	Location	Latitude	Longitude	Elev. (m)	Used	Rej.	Unsampled	R (ppm)	χ^2	Bias (ppm)	SE (ppm)
co2_rta_aircraft-pfp_1_allvalid_1000 2000masl	NOAA	Rarotonga, Cook Islands	21.25°S	159.83°W	1640	309	5	0	0.2 - 0.6	1.13	-0.07	0.47
co2_rta_aircraft-pfp_1_allvalid_2000-3000masl	NOAA	Rarotonga, Cook Islands	21.25°S	159.83°W	2567	311	3	0	0.3 - 0.8	1.19	-0.15	0.49
co2_rta_aircraft-pfp_1_allvalid_3000 4000masl	NOAA	Rarotonga, Cook Islands	21.25°S	159.83°W	3483	437	6	0	0.2 - 0.9	1.15	-0.18	0.55
co2_rta_aircraft-pfp_1_allvalid_4000-5000masl	NOAA	Rarotonga, Cook Islands	21.25°S	159.83°W	4543	328	1	0	0.3 - 0.9	1.23	-0.05	0.58
co2_rta_aircraft-pfp_1_allvalid_5000 6000masl	NOAA	Rarotonga, Cook Islands	21.25°S	159.83°W	5470	353	1	0	0.2 - 0.9	1.28	-0.12	0.58
co2_rta_aircraft-pfp_1_allvalid_6000-7000masl	NOAA	Rarotonga, Cook Islands	21.25°S	159.83°W	6246	314	5	0	0.2 - 2.2	0.70	0.04	0.71
co2_san_aircraft-pfp_1_allvalid_1000 2000masl	NOAA	Santarem, Brazil	2.85°S	54.95°W	1713	10	0	0	1.0 - 4.0	0.65	-1.99	2.44
co2_san_aircraft-pfp_1_allvalid_2000-3000masl	NOAA	Santarem, Brazil	2.85°S	54.95°W	2527	48	1	0	0.3 - 3.0	0.95	-0.07	1.57
co2_san_aircraft-pfp_1_allvalid_3000 4000masl	NOAA	Santarem, Brazil	2.85°S	54.95°W	3436	77	0	0	0.5 - 2.2	1.22	0.30	1.02
co2_san_aircraft-pfp_1_allvalid_4000-5000masl	NOAA	Santarem, Brazil	2.85°S	54.95°W	4600	6	0	0	1.3 - 1.5	0.45	0.42	0.85
co2_sca_aircraft-pfp_1_allvalid_0-1000masl	NOAA	Offshore Charleston, South Carolina, United States	32.77°N	79.55°W	651	285	11	0	0.5 - 4.4	1.16	-0.68	2.61
co2_sca_aircraft-pfp_1_allvalid_1000-2000masl	NOAA	Offshore Charleston, South Carolina, United States	32.77°N	79.55°W	1537	228	6	0	0.6 - 3.5	1.14	0.38	1.77

(table continued on next page)

Dataset	Lab.	Location	Latitude	Longitude	Elev. (m)	Used	Rej.	Unsampled	R (ppm)	χ^2	Bias (ppm)	SE (ppm)
co2_sca_aircraft-pfp_1_allvalid_2000 3000masl	NOAA	Offshore Charleston, South Carolina, United States	32.77°N	79.55°W	2487	510	20	0	0.3 - 2.7	1.00	0.29	1.30
co2_sca_aircraft-pfp_1_allvalid_3000-4000masl	NOAA	Offshore Charleston, South Carolina, United States	32.77°N	79.55°W	3522	334	13	0	0.2 - 2.8	1.04	0.23	1.17
co2_sca_aircraft-pfp_1_allvalid_4000 5000masl	NOAA	Offshore Charleston, South Carolina, United States	32.77°N	79.55°W	4457	467	13	0	0.2 - 2.3	1.11	0.12	1.01
co2_sca_aircraft-pfp_1_allvalid_5000-6000masl	NOAA	Offshore Charleston, South Carolina, United States	32.77°N	79.55°W	5502	288	7	0	0.4 - 2.0	1.16	0.14	0.88
co2_sca_aircraft-pfp_1_allvalid_6000 7000masl	NOAA	Offshore Charleston, South Carolina, United States	32.77°N	79.55°W	6415	327	5	0	0.4 - 1.5	1.14	0.17	0.83
co2_sca_aircraft-pfp_1_allvalid_7000-8000masl	NOAA	Offshore Charleston, South Carolina, United States	32.77°N	79.55°W	7451	413	12	0	0.3 - 1.5	1.03	0.15	0.77
co2_sca_aircraft-pfp_1_allvalid_8000 9000masl	NOAA	Offshore Charleston, South Carolina, United States	32.77°N	79.55°W	8108	97	2	0	0.2 - 1.8	0.84	0.05	1.21
co2_sca_aircraft-pfp_1_allvalid_9000-10000masl	NOAA	Offshore Charleston, South Carolina, United States	32.77°N	79.55°W	9362	15	0	0	0.3 - 4.8	1.40	-0.34	2.32
co2_sca_aircraft-pfp_1_allvalid_1000 11000masl	NOAA	Offshore Charleston, South Carolina, United States	32.77°N	79.55°W	10432	18	0	0	0.1 - 5.0	1.08	-0.41	1.86
co2_sca_aircraft-pfp_1_allvalid_11000-12000masl	NOAA	Offshore Charleston, South Carolina, United States	32.77°N	79.55°W	11160	7	0	0	0.4 - 5.3	0.85	-0.94	3.25
co2_sca_aircraft-pfp_1_allvalid_1200 13000masl	NOAA	Offshore Charleston, South Carolina, United States	32.77°N	79.55°W	12636	14	0	0	0.3 - 1.6	1.31	0.21	0.88
co2_sca_aircraft-pfp_1_allvalid_13000-14000masl	NOAA	Offshore Charleston, South Carolina, United States	32.77°N	79.55°W	13145	4	0	0	0.6 - 0.8	1.46	0.17	1.02

(table continued on next page)

Dataset	Lab.	Location	Latitude	Longitude	Elev. (m)	Used	Rej.	Unsampled	R (ppm)	χ^2	Bias (ppm)	SE (ppm)
co2_sct_surface-pfp_1_allvalid-305magl	NOAA	Beech Island, South Carolina, United States	33.41°N	81.83°W	115	2556	11	0	2.3 - 33.2	0.40	-0.71	3.54
co2_sct_tower-insitu_1_allvalid-305magl	NOAA	Beech Island, South Carolina, United States	33.41°N	81.83°W	115	90991	1503	0	2.4 - 23.6	0.83	0.41	4.51
co2_sct_tower-insitu_1_allvalid-31magl	NOAA	Beech Island, South Carolina, United States	33.41°N	81.83°W	115	15240	449	0	2.7 - 4.8	0.84	-0.60	4.39
co2_sct_tower-insitu_1_allvalid-61magl	NOAA	Beech Island, South Carolina, United States	33.41°N	81.83°W	115	15592	477	0	2.6 - 4.7	0.84	-0.78	4.11
co2_sey_surface-flask_1_representati	NOAA	Mahe Island, Seychelles	4.68°S	55.53°E	2	826	0	0	0.3 - 1.0	1.11	-0.11	0.72
co2_sgp_aircraft-pfp_1_allvalid_0-1000masl	NOAA	Southern Great Plains, Oklahoma, United States	36.61°N	97.49°W	679	994	42	0	0.2 - 8.3	0.97	-0.16	2.80
co2_sgp_aircraft-pfp_1_allvalid_1000 2000masl	NOAA	Southern Great Plains, Oklahoma, United States	36.61°N	97.49°W	1571	1229	44	0	0.6 - 6.2	0.92	0.13	2.09
co2_sgp_aircraft-pfp_1_allvalid_2000-3000masl	NOAA	Southern Great Plains, Oklahoma, United States	36.61°N	97.49°W	2462	1197	39	0	0.5 - 2.3	1.01	-0.21	1.43
co2_sgp_aircraft-pfp_1_allvalid_3000 4000masl	NOAA	Southern Great Plains, Oklahoma, United States	36.61°N	97.49°W	3467	977	33	0	0.6 - 1.9	1.21	-0.16	1.05
co2_sgp_aircraft-pfp_1_allvalid_4000-5000masl	NOAA	Southern Great Plains, Oklahoma, United States	36.61°N	97.49°W	4656	557	22	0	0.4 - 2.1	1.20	-0.18	1.01
co2_sgp_aircraft-pfp_1_allvalid_5000 6000masl	NOAA	Southern Great Plains, Oklahoma, United States	36.61°N	97.49°W	5395	236	9	0	0.4 - 1.6	1.29	-0.05	0.90
co2_sgp_aircraft-pfp_1_allvalid_6000-7000masl	NOAA	Southern Great Plains, Oklahoma, United States	36.61°N	97.49°W	6464	2	4	0	0.6 - 0.6	3.15	-0.99	0.65

(table continued on next page)

Dataset	Lab.	Location	Latitude	Longitude	Elev. (m)	Used	Rej.	Unsampled	R (ppm)	χ^2	Bias (ppm)	SE (ppm)
co2_sgp_aircraft-pfp_1_allvalid_80009000masl	NOAA	Southern Great Plains, Oklahoma, United States	36.61°N	97.49°W	8062	2	0	0	1.3 - 1.3	0.02	-1.20	1.97
co2_sgp_aircraft-pfp_1_allvalid_9000-10000masl	NOAA	Southern Great Plains, Oklahoma, United States	36.61°N	97.49°W	9686	7	0	0	0.8 - 0.8	3.31	-0.73	0.63
co2_sgp_aircraft-pfp_1_allvalid_1100012000masl	NOAA	Southern Great Plains, Oklahoma, United States	36.61°N	97.49°W	11321	2	0	0	0.7 - 0.7	0.49	-0.05	0.96
co2_sgp_aircraft-pfp_1_allvalid_12000-13000masl	NOAA	Southern Great Plains, Oklahoma, United States	36.61°N	97.49°W	12858	3	0	0	0.5 - 0.5	2.13	-0.18	0.78
co2_sgp_surface-flask_1_representati	NOAA	Southern Great Plains, Oklahoma, United States	36.61°N	97.49°W	314	897	13	0	2.2 - 8.0	0.79	-0.85	3.48
co2_sgp_surface-insitu_64_allvalid-60magl	LBNL-ARM	Southern Great Plains, Oklahoma, United States	36.61°N	97.49°W	314	19267	664	0	2.4 - 10.0	0.88	-0.40	4.75
co2_shm_surface-flask_1_representati	NOAA	Shemya Island, Alaska, United States	52.71°N	174.13°E	23	700	15	0	0.7 - 5.9	1.19	-0.50	1.70
co2_sis_surface-flask_2_representative	CSIRO	Shetland Islands, Scotland	60.09°N	1.25°W	30	82	5	0	0.2 - 2.2	1.36	0.49	1.15
co2_smo_surface-flask_1_representati	NOAA	Tutuila, American Samoa	14.25°S	170.56°W	42	1663	15	0	0.1 - 2.2	0.78	-0.04	0.39
co2_smo_surface-flask_4_representative	SIO	Tutuila, American Samoa	14.25°S	170.56°W	42	590	2	0	0.1 - 4.5	0.43	-0.04	0.64
co2_smo_surface-flask_426_represent	SIO_CO2	Tutuila, American Samoa	14.25°S	170.56°W	42	665	10	0	0.2 - 2.1	0.76	-0.13	0.52
co2_smo_surface-insitu_1_allvalid	NOAA	Tutuila, American Samoa	14.25°S	170.56°W	42	36127	0	0	0.2 - 0.8	1.42	-0.01	0.29
co2_spl_surface-insitu_3_nonlocal	NCAR	Storm Peak Laboratory (Desert Research Institute), United States	40.45°N	106.73°W	3210	63312	1562	0	1.0 - 2.8	1.03	-0.60	1.59
co2_spo_surface-flask_1_representative	NOAA	South Pole, Antarctica, United States	89.98°S	24.80°W	2810	1430	2	1	0.0 - 1.3	0.23	0.00	0.12

(table continued on next page)

Dataset	Lab.	Location	Latitude	Longitude	Elev. (m)	Used	Rej.	Unsampled	R (ppm)	χ^2	Bias (ppm)	SE (ppm)
co2_spo_surface-flask_4_representati	SIO	South Pole, Antarctica, United States	89.98°S	24.80°W	2810	474	2	0	0.1 - 8.9	0.21	-0.01	0.15
co2_spo_surface-flask_426_representative	SIO_CO2	South Pole, Antarctica, United States	89.98°S	24.80°W	2810	446	0	0	0.1 - 1.5	0.23	-0.02	0.21
co2_spo_surface-insitu_1_allvalid	NOAA	South Pole, Antarctica, United States	89.98°S	24.80°W	2810	53887	2	0	0.1 - 0.5	1.56	-0.00	0.09
co2_stm_surface-flask_1_representative	NOAA	Ocean Station M, Norway	66.00°N	2.00°E	0	780	18	0	0.4 - 5.5	0.99	-0.36	1.26
co2_sum_surface-flask_1_representati	NOAA	Summit, Greenland	72.60°N	38.42°W	3210	809	59	0	0.3 - 1.2	1.38	-0.12	0.77
co2_svv_tower-insitu_20_allvalid-27magl	NIES	Savvushka, Russia	51.33°N	82.13°E	495	7513	310	0	1.5 - 5.0	1.13	-0.41	3.76
co2_svv_tower-insitu_20_allvalid-52magl	NIES	Savvushka, Russia	51.33°N	82.13°E	495	7093	310	0	1.5 - 4.9	1.16	-0.36	3.82
co2_syo_surface-flask_1_representative	NOAA	Syowa Station, Antarctica, Japan	69.01°S	39.59°E	14	449	0	0	0.1 - 0.6	0.58	-0.09	0.18
co2_tap_surface-flask_1_representati	NOAA	Tae-ahn Peninsula, Republic of Korea	36.74°N	126.13°E	16	1197	18	0	1.6 - 12.1	0.73	-0.33	5.17
co2_tf1_shipboard-insitu_20_allvalid	NIES	Trans Future 1 (M/S Trans Future 1 of the Toyofuji Shipping Co., Ltd)	variable		Surface	75787	1442	0	0.9 - 69.3	0.62	-0.96	3.34
co2_tf5_shipboard-insitu_20_allvalid	NIES	Trans Future 5 (M/S Trans Future 5 of Toyofuji Shipping Co., Ltd.)	variable		Surface	399131	10327	0	0.2 - 66.8	0.59	-0.07	1.79
co2_tgc_aircraft-pfp_1_allvalid_0-1000masl	NOAA	Offshore Corpus Christi, Texas, United States	27.73°N	96.86°W	692	173	11	0	0.7 - 4.9	0.88	-0.32	2.12
co2_tgc_aircraft-pfp_1_allvalid_1000-2000masl	NOAA	Offshore Corpus Christi, Texas, United States	27.73°N	96.86°W	1555	201	4	0	0.5 - 3.1	1.00	0.28	1.43

(table continued on next page)

Dataset	Lab.	Location	Latitude	Longitude	Elev. (m)	Used	Rej.	Unsampled	R (ppm)	χ^2	Bias (ppm)	SE (ppm)
co2_tgc_aircraft-pfp_1_allvalid_2000-3000masl	NOAA	Offshore Corpus Christi, Texas, United States	27.73°N	96.86°W	2521	428	18	0	0.4 - 2.2	0.95	0.14	0.94
co2_tgc_aircraft-pfp_1_allvalid_3000 4000masl	NOAA	Offshore Corpus Christi, Texas, United States	27.73°N	96.86°W	3489	250	9	0	0.3 - 1.4	1.10	0.13	0.81
co2_tgc_aircraft-pfp_1_allvalid_4000-5000masl	NOAA	Offshore Corpus Christi, Texas, United States	27.73°N	96.86°W	4460	435	11	0	0.2 - 1.3	1.06	0.05	0.76
co2_tgc_aircraft-pfp_1_allvalid_5000 6000masl	NOAA	Offshore Corpus Christi, Texas, United States	27.73°N	96.86°W	5552	222	7	0	0.2 - 1.0	1.18	0.10	0.68
co2_tgc_aircraft-pfp_1_allvalid_6000-7000masl	NOAA	Offshore Corpus Christi, Texas, United States	27.73°N	96.86°W	6414	246	4	0	0.2 - 1.0	1.22	0.15	0.67
co2_tgc_aircraft-pfp_1_allvalid_7000 8000masl	NOAA	Offshore Corpus Christi, Texas, United States	27.73°N	96.86°W	7431	334	6	0	0.1 - 1.1	1.14	0.14	0.63
co2_tgc_aircraft-pfp_1_allvalid_8000-9000masl	NOAA	Offshore Corpus Christi, Texas, United States	27.73°N	96.86°W	8065	82	1	0	0.3 - 1.3	0.91	0.15	0.73
co2_thd_aircraft-pfp_1_allvalid_0-1000masl	NOAA	Trinidad Head, California, United States	41.05°N	124.15°W	629	391	9	0	1.8 - 11.7	0.57	-1.33	5.00
co2_thd_aircraft-pfp_1_allvalid_1000-2000masl	NOAA	Trinidad Head, California, United States	41.05°N	124.15°W	1536	213	12	0	0.4 - 2.3	1.34	-0.07	3.83
co2_thd_aircraft-pfp_1_allvalid_2000 3000masl	NOAA	Trinidad Head, California, United States	41.05°N	124.15°W	2480	400	15	0	0.2 - 2.4	1.31	0.14	1.30
co2_thd_aircraft-pfp_1_allvalid_3000-4000masl	NOAA	Trinidad Head, California, United States	41.05°N	124.15°W	3512	259	19	0	0.1 - 3.8	1.43	0.22	1.43
co2_thd_aircraft-pfp_1_allvalid_4000 5000masl	NOAA	Trinidad Head, California, United States	41.05°N	124.15°W	4440	328	13	0	0.2 - 4.4	1.11	0.22	1.34

(table continued on next page)

Dataset	Lab.	Location	Latitude	Longitude	Elev. (m)	Used	Rej.	Unsampled	R (ppm)	χ^2	Bias (ppm)	SE (ppm)
co2_thd_aircraft-pfp_1_allvalid_5000-6000masl	NOAA	Trinidad Head, California, United States	41.05°N	124.15°W	5492	213	6	0	0.2 - 2.5	1.28	0.18	1.12
co2_thd_aircraft-pfp_1_allvalid_6000 7000masl	NOAA	Trinidad Head, California, United States	41.05°N	124.15°W	6450	260	12	0	0.3 - 2.2	1.32	0.16	0.99
co2_thd_aircraft-pfp_1_allvalid_7000-8000masl	NOAA	Trinidad Head, California, United States	41.05°N	124.15°W	7472	270	17	0	0.2 - 2.0	1.03	0.10	0.98
co2_thd_aircraft-pfp_1_allvalid_8000 9000masl	NOAA	Trinidad Head, California, United States	41.05°N	124.15°W	8044	22	0	0	0.8 - 1.5	1.13	-0.14	1.20
co2_thd_surface-flask_1_representative	NOAA	Trinidad Head, California, United States	41.05°N	124.15°W	107	655	3	0	1.9 - 16.3	0.51	-2.29	4.96
co2_tik_surface-flask_1_representati	NOAA	Hydrometeorological Observatory of Tiksi, Russia	71.60°N	128.89°E	19	280	6	0	1.2 - 6.1	0.86	-0.45	3.72
co2_ulb_aircraft-pfp_1_allvalid_1000-2000masl	NOAA	Ulaanbaatar, Mongolia	47.40°N	106.00°E	1648	154	4	0	0.3 - 4.3	1.34	-0.01	1.72
co2_ulb_aircraft-pfp_1_allvalid_2000 3000masl	NOAA	Ulaanbaatar, Mongolia	47.40°N	106.00°E	2471	139	6	0	0.4 - 2.9	1.47	-0.07	1.41
co2_ulb_aircraft-pfp_1_allvalid_3000-4000masl	NOAA	Ulaanbaatar, Mongolia	47.40°N	106.00°E	3478	147	7	0	0.3 - 2.8	1.57	-0.41	1.50
co2_ulb_aircraft-pfp_1_allvalid_4000 5000masl	NOAA	Ulaanbaatar, Mongolia	47.40°N	106.00°E	4209	55	2	0	0.1 - 1.8	1.15	-0.47	1.23
co2_ulb_aircraft-pfp_1_allvalid_5000-6000masl	NOAA	Ulaanbaatar, Mongolia	47.40°N	106.00°E	5718	2	0	0	0.4 - 0.4	2.85	0.55	0.11
co2_ush_surface-flask_1_representati	NOAA	Ushuaia, Argentina	54.85°S	68.31°W	12	355	3	0	0.2 - 1.0	0.75	-0.22	0.57
co2_uta_surface-flask_1_representative	NOAA	Wendover, Utah, United States	39.90°N	113.72°W	1327	873	13	1	0.9 - 6.6	0.93	0.75	2.41

(table continued on next page)

Dataset	Lab.	Location	Latitude	Longitude	Elev. (m)	Used	Rej.	Unsampled	R (ppm)	χ^2	Bias (ppm)	SE (ppm)
co2_uum_surface-flask_1_representati	NOAA	Ulaan Uul, Mongolia	44.45°N	111.10°E	1007	872	12	0	2.0 - 5.1	0.84	-0.32	3.03
co2_vgn_tower-insitu_20_allvalid-42magl	NIES	Vaganovo, Russia	54.50°N	62.32°E	192	10293	407	0	2.1 - 4.1	1.13	-0.20	3.40
co2_vgn_tower-insitu_20_allvalid-85magl	NIES	Vaganovo, Russia	54.50°N	62.32°E	192	10084	375	0	2.0 - 4.9	1.11	-0.25	3.64
co2_wbi_aircraft-pfp_1_allvalid_0-1000masl	NOAA	West Branch, Iowa, United States	41.72°N	91.35°W	639	154	8	0	0.8 - 9.8	1.02	-1.11	3.70
co2_wbi_aircraft-pfp_1_allvalid_1000 2000masl	NOAA	West Branch, Iowa, United States	41.72°N	91.35°W	1550	382	20	0	0.6 - 6.7	0.87	-0.39	2.70
co2_wbi_aircraft-pfp_1_allvalid_2000-3000masl	NOAA	West Branch, Iowa, United States	41.72°N	91.35°W	2550	238	6	0	0.5 - 8.9	1.07	-0.33	1.53
co2_wbi_aircraft-pfp_1_allvalid_3000 4000masl	NOAA	West Branch, Iowa, United States	41.72°N	91.35°W	3509	399	17	0	0.3 - 2.2	1.08	-0.10	1.20
co2_wbi_aircraft-pfp_1_allvalid_4000-5000masl	NOAA	West Branch, Iowa, United States	41.72°N	91.35°W	4548	283	8	0	0.4 - 2.3	1.31	-0.05	1.11
co2_wbi_aircraft-pfp_1_allvalid_5000 6000masl	NOAA	West Branch, Iowa, United States	41.72°N	91.35°W	5520	343	11	0	0.4 - 2.1	1.17	0.01	1.14
co2_wbi_aircraft-pfp_1_allvalid_6000-7000masl	NOAA	West Branch, Iowa, United States	41.72°N	91.35°W	6507	308	17	0	0.3 - 1.9	1.40	0.01	1.04
co2_wbi_aircraft-pfp_1_allvalid_7000 8000masl	NOAA	West Branch, Iowa, United States	41.72°N	91.35°W	7486	326	10	0	0.3 - 1.7	1.31	0.05	1.07
co2_wbi_aircraft-pfp_1_allvalid_8000-9000masl	NOAA	West Branch, Iowa, United States	41.72°N	91.35°W	8047	34	2	0	0.5 - 1.2	1.01	-0.14	0.94

(table continued on next page)

Dataset	Lab.	Location	Latitude	Longitude	Elev. (m)	Used	Rej.	Unsampled	R (ppm)	χ^2	Bias (ppm)	SE (ppm)
co2_wbi_surface-pfp_1_allvalid-379magl	NOAA	West Branch, Iowa, United States	41.72°N	91.35°W	242	3346	13	0	3.2 - 37.8	0.39	-0.97	4.66
co2_wbi_tower-insitu_1_allvalid-31magl	NOAA	West Branch, Iowa, United States	41.72°N	91.35°W	242	15667	425	0	3.4 - 9.7	0.85	-0.94	5.00
co2_wbi_tower-insitu_1_allvalid-379magl	NOAA	West Branch, Iowa, United States	41.72°N	91.35°W	242	99027	2317	0	2.9 - 19.1	0.85	-0.21	4.46
co2_wbi_tower-insitu_1_allvalid-99magl	NOAA	West Branch, Iowa, United States	41.72°N	91.35°W	242	16570	434	0	3.3 - 9.2	0.82	-1.03	4.83
co2_wgc_tower-insitu_1_allvalid-30magl	NOAA	Walnut Grove, California, United States	38.27°N	121.49°W	0	16638	280	0	2.7 - 14.0	0.67	-2.54	6.94
co2_wgc_tower-insitu_1_allvalid-483magl	NOAA	Walnut Grove, California, United States	38.27°N	121.49°W	0	98537	1326	0	2.3 - 12.8	0.64	-0.05	4.58
co2_wgc_tower-insitu_1_allvalid-484magl	NOAA	Walnut Grove, California, United States	38.26°N	121.49°W	2	1400	16	0	3.3 - 6.7	0.57	-0.31	5.27
co2_wgc_tower-insitu_1_allvalid-89magl	NOAA	Walnut Grove, California, United States	38.26°N	121.49°W	2	235	1	0	4.6 - 17.2	0.82	-5.92	9.02
co2_wgc_tower-insitu_1_allvalid-91magl	NOAA	Walnut Grove, California, United States	38.27°N	121.49°W	0	16465	229	0	2.6 - 23.8	0.62	-2.67	6.53
co2_wis_surface-flask_1_representative	NOAA	Weizmann Institute of Science at the Arava Institute, Ketura, Israel	29.96°N	35.06°E	151	904	9	0	1.3 - 4.2	0.95	-0.57	2.07
co2_wkt_tower-insitu_1_allvalid-122magl	NOAA	Moody, Texas, United States	31.31°N	97.33°W	251	21210	709	0	2.2 - 6.9	0.77	-1.04	3.42

(table continued on next page)

Dataset	Lab.	Location	Latitude	Longitude	Elev. (m)	Used	Rej.	Unsampled	R (ppm)	χ^2	Bias (ppm)	SE (ppm)
co2_wkt_tower-insitu_1_allvalid-244magl	NOAA	Moody, Texas, United States	31.31°N	97.33°W	251	14848	418	0	2.2 - 6.6	0.97	-0.95	4.00
co2_wkt_tower-insitu_1_allvalid-30magl	NOAA	Moody, Texas, United States	31.31°N	97.33°W	251	21733	675	0	2.3 - 4.2	0.77	-0.85	3.54
co2_wkt_tower-insitu_1_allvalid-457magl	NOAA	Moody, Texas, United States	31.31°N	97.33°W	251	110401	2303	0	2.1 - 40.7	0.77	-0.26	2.96
co2_wkt_tower-insitu_1_allvalid-62magl	NOAA	Moody, Texas, United States	31.31°N	97.33°W	251	2443	86	0	2.0 - 4.7	0.91	-1.14	3.57
co2_wkt_tower-insitu_1_allvalid-9magl	NOAA	Moody, Texas, United States	31.31°N	97.33°W	251	2851	85	0	2.5 - 6.1	0.89	-0.95	4.34
co2_wlg_surface-flask_1_representati	NOAA	Mt. Waliguan, Peoples Republic of China	36.29°N	100.90°E	3810	852	9	0	1.0 - 4.3	0.93	-0.11	2.32
co2_wpc_shipboard-flask_1_representative	NOAA	Western Pacific Cruise	variable		Surface	182	6	0	0.1 - 2.2	1.07	-0.22	0.66
co2_wsa_surface-insitu_6_allvalid	ECCC	Sable Island, Nova Scotia, Canada	43.93°N	60.01°W	5	15659	532	0	1.6 - 3.6	1.02	-0.21	2.29
co2_yak_tower-insitu_20_allvalid-11magl	NIES	Yakutsk, Russia	62.09°N	129.36°E	264	5016	76	0	2.3 - 7.2	0.94	-0.80	5.37
co2_yak_tower-insitu_20_allvalid-77magl	NIES	Yakutsk, Russia	62.09°N	129.36°E	264	5127	80	0	2.3 - 6.4	0.98	-0.22	5.19
co2_zep_surface-flask_1_representative	NOAA	Ny-Alesund, Svalbard, Norway and Sweden	78.91°N	11.89°E	474	948	59	0	0.4 - 1.5	1.16	-0.10	0.94
co2_zep_surface-insitu_442_allvalid-15magl	ICOS-ATC	Ny-Alesund, Svalbard, Norway and Sweden	78.91°N	11.89°E	474	4198	319	0	0.5 - 1.1	1.22	0.00	0.88
co2_zep_surface-insitu_56_allvalid	NILU	Ny-Alesund, Svalbard, Norway and Sweden	78.91°N	11.89°E	474	1570	217	0	0.4 - 1.7	1.33	0.34	1.05

(table continued on next page)

Dataset	Lab.	Location	Latitude	Longitude	Elev. (m)	Used	Rej.	Unsampled	R (ppm)	χ^2	Bias (ppm)	SE (ppm)

Summary of Observational Sites Used in CarbonTracker. The site location is specified by latitude, longitude and elevation in meters above sea level. The number of observations actually assimilated for each dataset is listed in the column "Used", and the number rejected due to inability to fit the observations is listed in the column "Rej.". Model-data-mismatch (R) is a value assigned to a given site that is meant to quantify our expected ability to simulate observations there. In this table we report the range of R values assigned to dataset observations by our "adaptive" model-data mismatch scheme (Sec. 7.2). These values are principally determined from the limitations of the atmospheric transport model. It is part of the standard deviation used to interpret the difference between a simulation first guess (Hx) of an observation and the actual measured value (z). The other component, HPH^{T}, is a measure of the ability of the ensemble Kalman filter to improve its simulated value for this observation by adjusting fluxes. These elements together form the innovation χ statistic for the site: $\chi = (z - Hx)/\sqrt{(HPH^{\mathrm{T}} + R^2)}$. The innovation χ^2 reported above is the mean of all squared χ values for a given site. An average χ^2 below 1.0 indicates that the $HPH^{\mathrm{T}} + R^2$ values are too large. Conversely, values above 1.0 mean that this standard deviation is underestimated. The bias and SE columns are statistics of the posterior residuals (final modeled values - measured values). The bias is the mean of these residuals; the SE is the standard error of those residuals.

8 Ensemble data assimilation

Data assimilation is the process by which a model simulation is adjusted to agree with observations. Model simulations may drift off from reality for a number of reasons. Some models are highly nonlinear, and depend sensitively on knowing the system state with high accuracy. Weather models fall into this category, and as a result reliable forecast systems depend on having a constant stream of meteorological data to correct their simulations. In contrast, models like CarbonTracker need data assimilation not because the controlling dynamics are nonlinear, but because those dynamics are not well known. CarbonTracker uses approximate or estimated rules about the evolution of surface CO_2 fluxes, then corrects these approximate projections using observational constraints. The resulting optimal surface flux estimates can then be used to better understand the functioning of the carbon cycle.

Data assimilation is usually a cyclical process, in which estimates get refined over time as more observations become available. Mathematically, data assimilation can be performed using a wide variety of techniques, including variational and ensemble methods. Assimilation systems involving simulations of the global atmosphere are often implemented on highly parallel supercomputers in order to distribute the workload among many computational cores. CarbonTracker is an example of such a model because it relies heavily on estimates of global atmospheric transport.

CarbonTracker model predictions are limited by the relatively simple representations of CO_2 surface exchange used to predict land biosphere and ocean fluxes and emissions from fossil fuel combustion and wildfires. As described in the following section, we use data assimilation techniques to modify these surface fluxes so that the resulting atmospheric distribution of CO_2 agrees optimally with measurements. We do this by estimating a set of spatially- and temporally-varying scaling factors that multiply first-guess predictions from prior flux models. Data assimilation allows us to determine optimal values for these scaling factors.

8.1 Parameterization of unknowns

CO_2 fluxes $F(x, y, t)$ in CarbonTracker are parameterized according to

$$F(x,y,t) = \lambda(x,y,t)\Big(F_{\text{land}}(x,y,t) + F_{\text{ocean}}(x,y,t)\Big) + F_{\text{FF}}(x,y,t) + F_{\text{fire}}(x,y,t), \tag{11}$$

where F_{land}, F_{ocean}, F_{FF}, and F_{bio} are prior flux model predictions for land biosphere, ocean, fossil fuel and wildfire emissions respectively, and λ represents a set of unknown multiplicative scaling factors

applied to the fluxes, to be estimated in the assimilation. These scaling factors are the final product of our assimilation and together with the prior flux models determine CarbonTracker optimized fluxes. Note that no scaling factors are applied to the fossil fuel and fire modules. The fossil fuel and wildfire fluxes are relatively well-known from prior flux models compared to highly-uncertain land biosphere and ocean fluxes, and as a result we impose those emissions without modification in our model.

8.1.1 Optimization regions

The scaling factors λ are estimated independently for each week and optimization region. They are assumed to be constant over this time period and spatial domain. Each scaling factor is associated with a particular region of the globe, as in the Transcom inversion study [Gurney et al., 2002]. Currently the geographic distribution of these optimization regions is fixed. The choice of regions is a strong *a priori* design decision determining the reliability of the resulting fluxes. In particular, the scale of optimization regions is chosen to minimize "aggregation errors" [Kaminski et al., 2001], while limiting the set of unknown parameters to a manageable number. Following Jacobson et al. [2007], we have divide the global ocean into 30 basins encompassing large-scale ocean circulation and biogeochemical features. The terrestrial biosphere is divided up according to ecosystem type and geographical domain. Specifically, each of the 11 Transcom land regions is subdivided into a maximum of 19 "ecoregions" according to its Olson et al. [1992] vegetation classification. The set of ecoregions over North America is summarized in Table 4 and Figure 18. Note that there is currently no requirement for ecoregions to be contiguous, and a single scaling factor can be applied to the same vegetation type on both sides of a continent. Further details on ecoregions can be found in Section 9

Theoretically, this approach leads to a total number of 11*19+30=239 optimizable scaling factors for each week, but the actual number of optimization regions is only 156 since some ecosystem types are not represented in every Transcom region. It should be noted also that we have chosen to not optimize scaling factors for ice-covered regions, inland water bodies, and deserts, since the CO_2 flux from these regions is negligible.

It is important to note that even though only one parameter is available to scale, for instance, the flux from coniferous forests in Boreal North America, each $1^\circ \times 1^\circ$ grid box predominantly covered by coniferous forests will have a different optimized flux $\lambda F_{\text{land}}(x, y, t)$ depending on local temperature, radiation, and emissions as simulated by the prior flux model.

category	Olson V 1.3	Percentage area
1	Conifer Forest	19.0%
2	Broadleaf Forest	1.3%
3	Mixed Forest	7.5%
4	Grass/Shrub	12.6%
5	Tropical Forest	0.3%
6	Scrub/Woods	2.1%
7	Semitundra	19.4%
8	Fields/Woods/Savanna	4.9%
9	Northern Taiga	8.1%
10	Forest/Field	6.3%
11	Wetland	1.7%
12	Deserts	0.1%
13	Shrub/Tree/Suc	0.1%
14	Crops	9.7%
15	Conifer Snowy/Coastal	0.4%
16	Wooded tundra	1.7%
17	Mangrove	0.0%
18	Non-optimized areas (ice, polar desert, inland seas)	0.0%
19	Water	4.9%

Table 4: Ecosystem types over North America

Ecosystem types are based on the vegetation classification of Olson et al. [1992]. Note that we have adjusted the original 29 categories into only 19 regions. This was done mainly to fill the unused categories 16, 17, and 18, and to group the similar categories 23-26+29. Table 4 shows each vegetation category considered. Percentages indicate the relative area in North America associated with each category.

Each $1^\circ \times 1^\circ$ pixel of our domain was assigned one of the categories above based on the Olson category that was most prevalent in the $0.5^\circ \times 0.5^\circ$ underlying area.

8.1.2 Assimilation window

Measured CO_2 mole fractions are the result of upstream surface fluxes and atmospheric transport, which includes both advective movement and diffusive mixing. Near-field surface fluxes can cause significant changes in CO_2 mole fractions, whereas flux signals from further upstream become spread out and diluted. Generally speaking, the longer in the past a flux event occurred, the smaller its impact will be on a given sample of air (although it will be spread out through a larger volume of the atmosphere). Thus we choose an "assimilation window" that represents how far back in time we expect to be able to pinpoint a given flux signal from available measurements. A good discussion of this topic can be found in Bruhwiler et al. [2005].

In previous versions of CarbonTracker, the assimilation window was chosen to be five weeks long, meaning that a measurement could cause revisions in surface fluxes only over the 5 weeks leading up to that measurement. In CT2022, we have extended the assimilation window length to 12 weeks. This helps to resolve fluxes in regions of the world with less dense observational coverage (the tropics, Southern Hemisphere, and parts of Asia).

This assimilation window is moved forward on each cycle of our estimation system, so that new weeks are introduced at the "head" of the filter, and the weeks that fall out the "tail" of the filter are finalized. Prior to CT2022, the 5-week assimilation window was moved forward one week at a time. In CT2022, the 12-week assimilation window is moved forward two weeks at a time. Scaling factors λ retain their weekly resolution. Each cycle of the inversion system requires running the atmospheric model for a length of time equal to the assimilation window length plus the window step size. For previous CarbonTracker releases, this was 6 weeks per cycle; for CT2022 it is 14 weeks per cycle. The extra computing time required by the longer assimilation window is balanced somewhat by the two-week stepping, and we have found that CT2022 required only about 15% more computing time per than previous releases.

8.1.3 Ensemble size and localization

The ensemble system used to solve for the scalar multiplication factors is similar to that in Peters et al. [2005] and based on the square root ensemble Kalman filter of Whitaker and Hamill [2002]. Ensemble statistics are created from 1200 randomly-chosen members, each with its own background CO_2 concentration field to represent the time history of that member's surface fluxes. The ensemble Kalman filter looks for correlations between these random flux perturbations and resulting changes in simulated CO_2 measurements. We might expect that the entire ensemble would agree that increasing the CO_2 flux in a given region results in greater simulated CO_2 at a nearby downwind site. However, because we approximate the flux covariance matrix with a random sample of 1200 members, sometimes spurious correlations appear. It is unphysical, for instance, that a measurement at Summit, Greenland could be strongly influenced by surface exchange in the southern Indian Ocean, within the time span of our assimilation window. Any such correlation between the flux ensemble and the measurement in question might be spurious. Localization is a technique developed for numerical weather prediction in which unphysical correlations are diagnosed and systematically ignored [Houtekamer and Mitchell, 1998]. We only perform localization for certain datasets. Notably, it is not used for datasets judged to represent hemisphere-scale signals, such as those from marine boundary layer sites in

remote locations.

Our localization technique is based on the linear correlation coefficient between the 1200 parameter deviations and 1200 observation deviations for each parameter/observation pair. If the relationship between a parameter deviation and its modeled observational impact is statistically significant, then that relationship is retained. Otherwise, the relationship is assumed to be spurious noise due to the numerical approximation of the covariance matrix by the limited ensemble. We accept relationships that reach 95% significance in a Student's T-test with a two-tailed probability distribution.

8.1.4 Dynamical model

In CarbonTracker, the dynamical model is applied to the ensemble-mean parameter values λ as:

$$\lambda^-[t] = (\lambda_0^- + \lambda^+[t-1] + \lambda^+[t-2])/3 \tag{12}$$

Where $\lambda^-[t]$ is the prior value of the scaling factors for timestep t, λ_0^- is the initial prior vector with all elements set to 1.0, and $\lambda^+[t-1]$ and $\lambda^+[t-2]$ are the posterior ("analyzed") scaling factors for timesteps $t-1$ and $t-2$ respectively. This model describes that parameter values λ for a new time step are chosen as a combination of optimized values from the two previous time steps and a fixed overall prior value of 1.0. This operation is similar to the simple persistence forecast used in Peters et al. [2005], but represents a smoothing over three time steps, which attenuates variations in the forecast of λ in time. The inclusion of the prior term λ_0^- acts as a regularization [Baker et al., 2006] and ensures that the parameters in our system will eventually revert back to predetermined prior values when there is no information coming from observations. Note that our dynamical model equation does not include an error term on the dynamical model, for the simple reason that we don't know the error of this model. This is reflected in the treatment of covariance, which is always set to a fixed prior covariance structure and not forecast with our dynamical model.

8.2 Covariance structure

The prior covariance structure P_0^- describes the magnitude of the uncertainty on each parameter, plus their correlation in space. The latter is applied such that correlations between the same ecosystem types in different Transcom regions decrease exponentially with distance scale $L = 2000$km, and thus assumes a coupling *between* the behavior of the same ecosystems in close proximity to one another (such as coniferous forests

in Boreal and Temperate North America). Furthermore, all ecosystems *within* tropical Transcom regions are coupled decreasing exponentially with distance since we do not believe the current observing network can constrain tropical fluxes on sub-continental scales, and want to prevent spurious compensating source/sink pairs ("dipoles") to occur in the tropics.

While the correlation structure discussed above has remained fixed in all CarbonTracker releases, we have been changing the overall magnitude of the covariance matrix in an attempt to mitigate seasonal biases in our simulated CO_2 fields. Since those biases appear mostly in comparison to measurement data over land, and also because the annual cycle of CO_2 in the atmosphere is dominated by the terrestrial carbon cycle, we experimented by loosening the land prior constraint. This is made evident in the "CT2011 through CT2017" trace in the lower panel of Fig. 15. As it turns out, these biases were mostly due to our original short assimilation window length (Sec. 8.1.2) and the convective flux problem discussed in Sec. 6.2. As a result, for CT2022 we were able to scale back the land prior covariance. "L-curve" analysis [Hansen, 1998] suggested that these covariances could be reduced even from the original levels, and new values are shown in red in the lower panel of Fig. 15.

8.3 Multiple prior models

In Bayesian estimation systems like CarbonTracker, there is a potential for bias from a flux prior to propagate through the inversion system to the final result. It is difficult to quantify this effect, and as a result it is generally considered a requirement that flux priors be unbiased. We cannot guarantee this for any of our prior fluxes, be they the prior estimates for terrestrial or oceanic exchange, or the presumed wildfire and fossil fuel emissions. In order to explicitly quantify the impact of prior bias on our solution, in CT2022 we present the average of two inversions using different priors. We have used two terrestrial flux priors (including two wildfire emissions estimates), two air-sea CO_2 exchange priors, and two estimates of imposed fossil fuel emissions in a factorial design experiment. Whereas previous releases conducted 8 independent inversions exploring each unique combination of priors in a factorial design, we have determined that interactions between priors are negligible. Thus, the quantification of uncertainty due to prior selection can be explored using just two inversions, each using a unique set of priors. We present as a final result the mean flux between these two inversions and the atmospheric CO_2 distribution resulting from applying these mean fluxes to our atmospheric transport model. Each of the priors is described in detail in its corresponding documentation section.

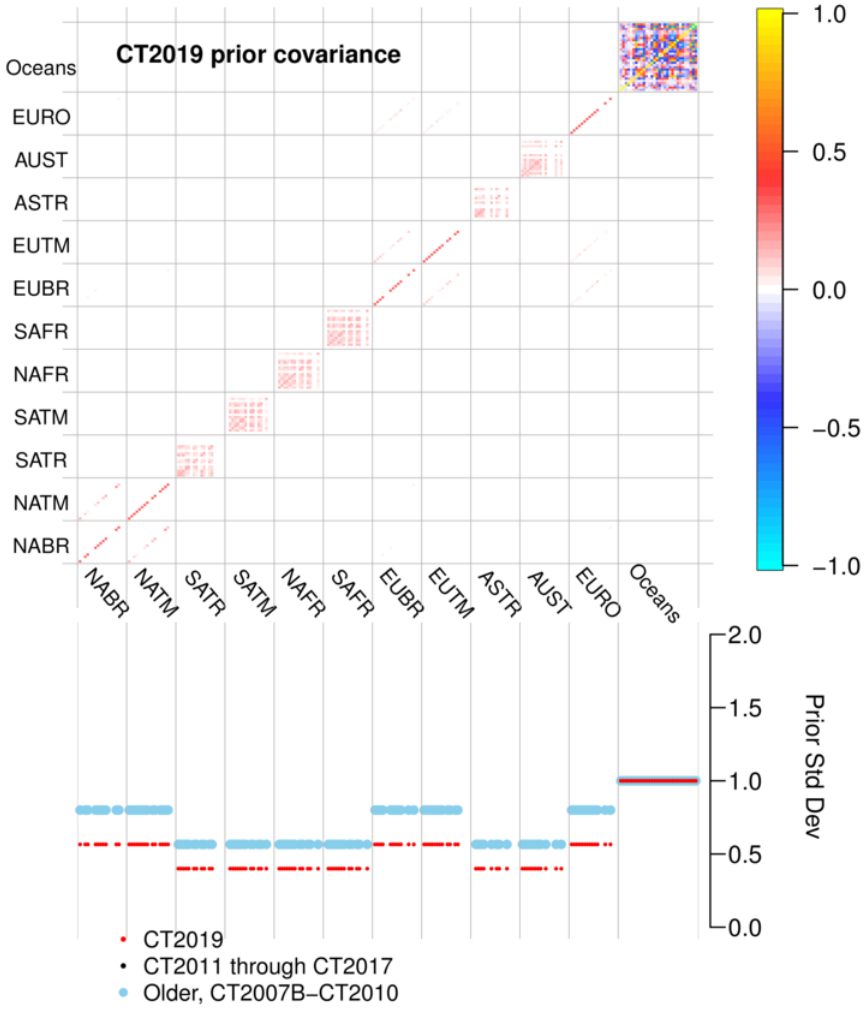

Figure 15: CT2022 prior covariance structure. The prior covariance matrix (top panel) and the square root of diagonal members of this matrix (bottom panel). Covariance matrix quantities are dimensionless squared scaling factors, and the bottom panel is the square root of this. Transcom land regions form the first 11 large divisions on the axes here. As described in Sec. 9, each of those regions contains 19 potential ecosystems. Correlations between similar ecosystems in proximate Transcom regions are visible in North America (*e.g.* NABR and NATM, the boreal and temperate North American regions) and Eurasia. Within tropical Transcom regions, however, differing ecosystems are assigned a non-zero prior covariance, which is visible here as red block-like structures on the diagonal within, for example, the South America Tropical (SATR) Transcom region. Ocean regions have a more complicated covariance structure that depends on which prior is used; the structure shown here is that of the ocean inversion flux prior. The lower panel of this diagram compares the on-diagonal elements of the prior covariance matrix by plotting their square roots. The resulting standard deviations are directly comparable to the percentages discussed in section 3 above; 0.5 is equivalent to 50%. The retuning of the covariance matrix for CT2022's multiple-prior simulation (in red) is made evident by also showing these values from previous CarbonTracker releases in light blue and black.

8.3.1 Posterior uncertainties in CarbonTracker

The formal "internal" error estimates produced by CarbonTracker are unrealistically large. This is largely a result of the dynamical model that introduces a fresh prior covariance matrix with every new week entering the assimilation window. Uncertainties using the new 12-week assimilation window are smaller that those from previous CarbonTracker releases that used a much shorter five-week assimilation window.

Uncertainties in CarbonTracker tend to increase as larger regions are considered; regional errors mostly just add in quadrature without any cancellation from dipole anticorrelation. Whereas many inversions yield smaller errors as the spatial extent of the region being considered increases, CarbonTracker acts in the opposite fashion. This is perhaps most obvious in the estimate of CarbonTracker's global annual surface flux of carbon dioxide. While CT2022 estimates a one-sigma error of about 2.7 Pg C yr^{-1} on its global flux, this quantity is in actuality much more well-constrained. This is evident from CarbonTracker's excellent agreement both with observational estimates of atmospheric growth rate and with independent CO_2 measurements.

In CT2022, our error estimates on optimized fluxes are smaller than those in previous releases. This is mainly due to the retuning of the land prior covariance discussed above. It should be noted that uncertainties presented for CT2022 take into account not only the "internal" flux uncertainty generated by a single inversion, but also the across-model "external" uncertainty representing the spread of the inversion models due to the choice of prior flux.

9 Ecoregions in CarbonTracker

9.1 What are ecoregions?

Ecoregions are the actual scale on which CarbonTracker performs its optimization over land. Ecoregions are meant to represent large expanses of land within a given continent having similar ecosystem types, and are used to divide continent-scale regions into smaller domains for analysis. The ecosystem types use in CarbonTracker are derived from the Olson et al. [1992] vegetation classification (Table 5, Figure 16).

We define an ecoregion as an ecosystem type within a given Transcom land region. There are 19 ecosystem types we extract from the Olson et al. [1992] system, and 11 Transcom land regions (Figure 17), so there are $11 \times 19 = 209$ possible ecoregions. However, not all ecosystem types are present in all Transcom

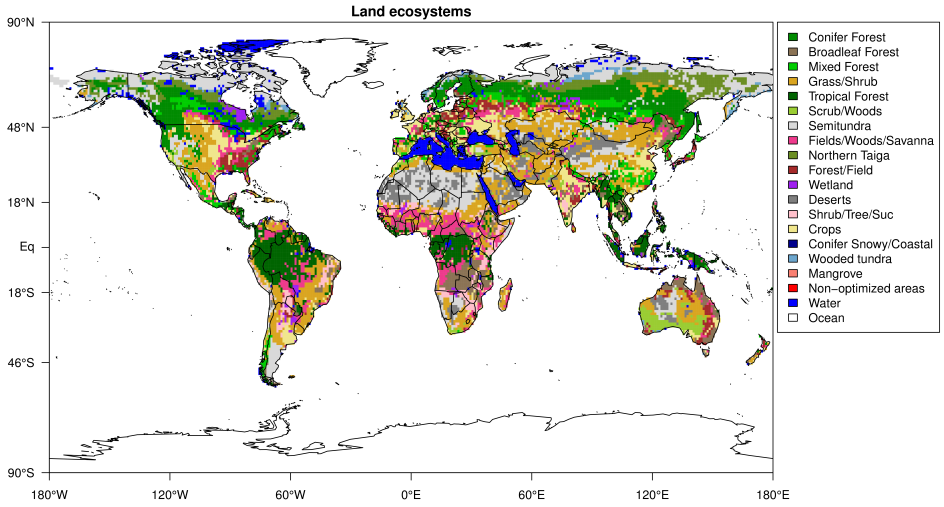

Figure 16: Global distribution of Olson ecosystem types.

regions, and the actual number of land ecoregions ends up being 126.

Note on "Semitundra": this is a potentially misleading shorthand abbreviation for a collection of ecosystems comprising semi-desert, shrubs, steppe, and polar+alpine tundra. The "Semitundra" zones appearing in northern Africa where one expects to find the Sahara desert are not, of course, tundra environments. They are instead semi-desert zones.

9.2 Why use ecoregions?

A fundamental challenge to atmospheric inversions like CarbonTracker is that there are not enough observations to directly constrain fluxes at all times and in all places. It is therefore necessary to find a way to reduce the number of unknowns being estimated. Strategies to reduce the number of unknowns in problems like this one generally impose information from external sources. In CarbonTracker, we reduce the problem size both by estimating fluxes at the ecoregion scale, and by using a terrestrial biological model to give a first guess flux from the ecoregion. The model is also used to give the spatial and temporal distribution of CO_2 flux within a region and week.

9.3 Ecosystems within Transcom regions

Each Transcom land region (Figure 17) can contain up to 19 ecoregions.

Ecosystem Type	North American Boreal		North American Temperate	
	Area (km^2)	Percentage	Area (km^2)	Percentage
Conifer Forest	2315376	22.9%	1607291	14.0%
Broadleaf Forest	-	-	269838	2.4%
Mixed Forest	592291	5.9%	930813	8.1%
Grass/Shrub	53082	0.5%	2515582	21.9%
Tropical Forest	-	-	58401	0.5%
Scrub/Woods	-	-	416520	3.6%
Semitundra	3396292	33.6%	866468	7.6%
Fields/Woods/Savanna	29243	0.3%	1020939	8.9%
Northern Taiga	1658773	16.4%	-	-
Forest/Field	61882	0.6%	1243174	10.8%
Wetland	322485	3.2%	66968	0.6%
Deserts	-	-	21934	0.2%
Shrub/Tree/Suc	-	-	11339	0.1%
Crops	-	-	1969912	17.2%
Conifer Snowy/Coastal	41440	0.4%	73437	0.6%
Wooded tundra	360388	3.6%	6643	0.1%
Mangrove	-	-	-	-
Non-optimized areas	-	-	-	-
Water	1269485	12.6%	384728	3.4%
Total	10100736	100.0%	11463986	100.0%

Table 5: Ecosystem areas over the two Transcom regions covering North America.

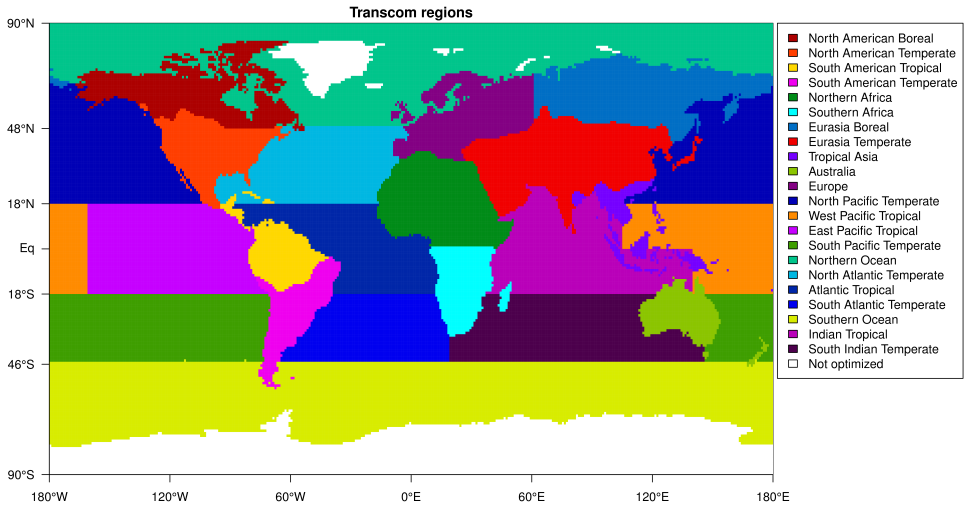

.

Figure 17: The 11 land regions and 11 ocean regions of the Transcom project, along with the unoptimized land areas in Greenland and Antarctica

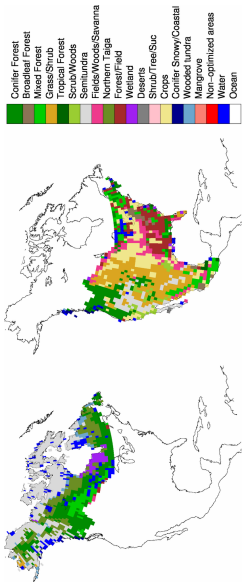

Figure 18: Ecoregions within the North American Boreal (left) and North American Temperate (right) Transcom regions.

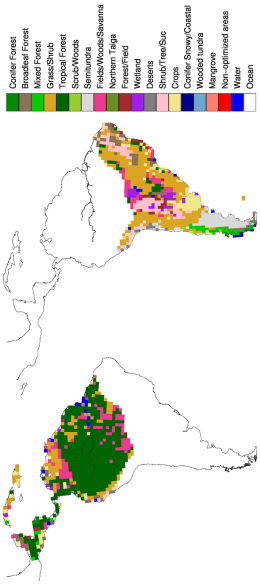

Figure 19: Ecoregions within the South American Tropical (left) and South American Temperate (right) Transcom regions.

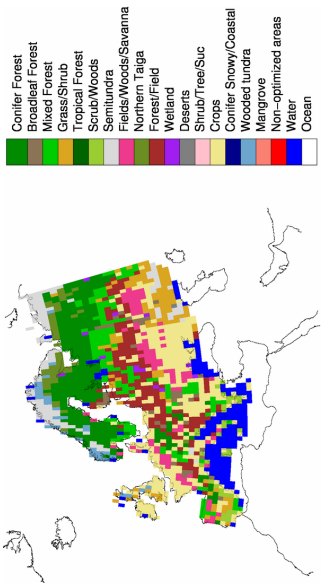

Figure 20: Ecoregions within the Europe Transcom region.

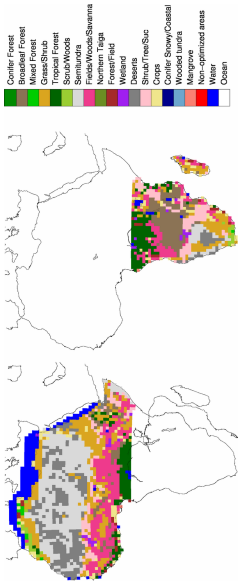

Figure 21: Ecoregions within the Northern Africa (left) and Southern Africa (right) Transcom regions.

10 Resources and References

- Jim Randerson research group
- Global Fire Emissions Database (GFED) web page
- NASA GFED_CMS CASA project
- Olson ecosystem types
- Global Fire Emissions Database (GFED) web page
- GFED_CMS web page at NACP
- DOE Energy Information Administration (EIA)
- BP Statistical Review of World Energy
- EDGAR Database
- DMSP satellite nightlight data
- Centre for Air Transport and the Environment (CATE), AERO2k aviation emissions inventory
- NOAA Pacific Marine Environmental Laboratory
- Ocean Acidification
- GML Carbon Cycle Program
- WMO/GAW Report No. 168, 2006

References

R. J. Andres, J. S. Gregg, L. Losey, G. Marland, and T. A. Boden. Monthly, global emissions of carbon dioxide from fossil fuel consumption. *Tellus B: Chemical and Physical Meteorology*, 63(3):309–327, 2011.

R. J. Andres, T. A. Boden, and D. Higdon. A new evaluation of the uncertainty associated with CDIAC estimates of fossil fuel carbon dioxide emission. *Tellus B: Chemical and Physical Meteorology*, 66(1): 23616, 2014.

D. F. Baker, R. M. Law, K. R. Gurney, P. Rayner, P. Peylin, A. S. Denning, P. Bousquet, L. Bruhwiler, Y. H. Chen, P. Ciais, I. Y. Fung, M. Heimann, J. John, T. Maki, S. Maksyutov, K. Masarie, M. Prather, B. Pak, S. Taguchi, and Z. Zhu. TransCom 3 CO_2 inversion intercomparison: Impact of transport model errors on the interannual variability of regional CO_2 fluxes, 1988-2003. *Global Biogeochemical Cycles*, 20(1), 2006. GB1002.

S. Basu and R. Nassar. Fossil Fuel CO_2 Emissions for the OCO2 Model Intercomparison Project (MIP), Jan. 2021. URL https://doi.org/10.5281/zenodo.4776925. Previous versions available from (2018), (2017), (2016), (2015a).

S. Basu, J. B. Miller, and S. Lehman. Separation of biospheric and fossil fuel fluxes of CO_2 by atmospheric inversion of CO_2 and $^{14}CO_2$ measurements: Observation system simulations. *Atmos. Chem. Phys*, 16(9): 5665–5683, 2016.

S. Basu, S. J. Lehman, J. B. Miller, A. E. Andrews, C. Sweeney, K. R. Gurney, X. Xu, J. Southon, and P. P. Tans. Estimating us fossil fuel CO_2 emissions from measurements of ^{14}C in atmospheric CO_2. *Proceedings of the National Academy of Sciences*, 117(24):13300–13307, 2020. doi: 10.1073/pnas.1919032117. URL https://www.pnas.org/doi/abs/10.1073/pnas.1919032117.

T. Blasing, G. Marland, and C. Broniak. Estimates of monthly CO_2 emissions and associated $^{13}C/^{12}C$ values from fossil-fuel consumption in the USA (1981-2003). *Carbon Dioxide Information Analysis Center, Oak Ridge National Laboratory, U.S. Department of Energy, Oak Ridge, Tenn., U.S.A.*, 2004. doi: 10.3334/CDIAC/ffe.001.

T. A. Boden, G. Marland, and R. J. Andres. Global, regional, and national fossil fuel CO_2 emissions. *Carbon Dioxide Information Analysis Center, Oak Ridge National Laboratory, U.S. Department of Energy, Oak Ridge, Tenn., U.S.A.*, 2017. doi: 10.3334/CDIAC/00001_V2017.

BP. *BP Statistical Review of World Energy*. BP p.l.c., London, 2021. URL https://www.bp.com/en/

global/corporate/energy-economics/statistical-review-of-world-energy.html.

British Petroleum. *BP Statistical Review of World Energy*. Number 68. BP p.l.c., London, 2019.

L. M. P. Bruhwiler, A. M. Michalak, W. Peters, D. F. Baker, and P. Tans. An improved Kalman smoother for atmospheric inversions. *Atmospheric Chemistry and Physics*, 5:2691–2702, 2005. doi: https://doi.org/10.5194/acp-5-2691-2005.

B. Byrne, D. F. Baker, S. Basu, M. Bertolacci, K. W. Bowman, D. Carroll, A. Chatterjee, F. Chevallier, P. Ciais, N. Cressie, D. Crisp, S. Crowell, F. Deng, Z. Deng, N. M. Deutscher, M. Dubey, S. Feng, O. García, D. W. T. Griffith, B. Herkommer, L. Hu, A. R. Jacobson, R. Janardanan, S. Jeong, M. S. Johnson, D. B. A. Jones, R. Kivi, J. Liu, Z. Liu, S. Maksyutov, J. B. Miller, S. M. Miller, I. Morino, J. Notholt, T. Oda, C. W. O'Dell, Y.-S. Oh, H. Ohyama, P. K. Patra, H. Peiro, C. Petri, S. Philip, D. F. Pollard, B. Poulter, M. Remaud, A. Schuh, M. K. Sha, K. Shiomi, K. Strong, C. Sweeney, Y. Té, V. A. Velazco, M. Vrekoussis, T. Warneke, et al. National CO_2 budgets (2015–2020) inferred from atmospheric CO_2 observations in support of the Global Stocktake. *Earth System Science Data Discussions*, 2022:1–59, 2022. doi: 10.5194/essd-2022-213. URL https://essd.copernicus.org/preprints/essd-2022-213/.

K. Caldeira and M. E. Wickett. Anthropogenic carbon and ocean pH. *Nature*, 425(6956):365–365, 2003.

E. Commission, J. R. Centre, F. Monforti-Ferrario, G. Oreggioni, E. Schaaf, D. Guizzardi, J. Olivier, E. Solazzo, E. Lo Vullo, M. Crippa, M. Muntean, and E. Vignati. *Fossil CO_2 and GHG emissions of all world countries : 2019 report*. Publications Office, 2019. doi: doi/10.2760/687800. URL https://data.jrc.ec.europa.eu/collection/EDGAR.

L. Giglio, G. R. van der Werf, J. T. Randerson, G. J. Collatz, and P. Kasibhatla. Global estimation of burned area using MODIS active fire observations. *Atmospheric Chemistry and Physics*, 6:957–974, 2006.

L. Giglio, J. T. Randerson, and G. R. van der Werf. Analysis of daily, monthly, and annual burned area using the fourth-generation global fire emissions database (GFED4). *Journal of Geophysical Research: Biogeosciences*, 118(1):317–328, 2013. doi: 10.1002/jgrg.20042. URL https://agupubs.onlinelibrary.wiley.com/doi/abs/10.1002/jgrg.20042.

D. Gilfillan and G. Marland. CDIAC-FF: global and national CO_2 emissions from fossil fuel combustion and cement manufacture: 1751–2017. *Earth System Science Data*, 13(4):1667–1680, 2021. doi: 10.5194/essd-13-1667-2021. URL https://essd.copernicus.org/articles/13/1667/2021/.

M. Gloor, N. Gruber, J. Sarmiento, C. L. Sabine, R. A. Feely, and C. Rödenbeck. A first estimate of present and preindustrial air-sea CO_2 flux patterns based on ocean interior carbon measurements and models. *Geophysical Research Letters*, 30(1):10.1029/2002GL015594, 2003.

N. Gruber, J. L. Sarmiento, and T. F. Stocker. An improved method for detecting anthropogenic CO_2 in the oceans. *Global Biogeochemical Cycles*, 10(4):809–837, 1996.

K. R. Gurney, R. M. Law, A. S. Denning, P. J. Rayner, D. Baker, P. Bousquet, L. Bruhwiler, Y.-H. Chen, P. Ciais, S. Fan, I. Y. Fung, M. Gloor, M. Heimann, K. Higuchi, J. John, T. Maki, S. Maksyutov, K. Masarie, P. Peylin, M. Prather, B. Pak, J. Randerson, J. L. Sarmiento, S. Taguchi, T. Takahashi, P. Tans, and C.-W. Yuen. Towards robust regional estimates of CO_2 sources and sinks using atmospheric transport models. *Nature*, 415, 2002.

P. C. Hansen. *Rank-deficient and discrete ill-posed problems: numerical aspects of linear inversion*. SIAM, 1998.

P. L. Houtekamer and H. L. Mitchell. Data assimilation using an ensemble Kalman filter technique. *Monthly Weather Review*, 126(3):796–811, 1998. doi: 10.1175/1520-0493(1998)126⟨0796:DAUAEK⟩2.0.CO;2. URL https://doi.org/10.1175/1520-0493(1998)126<0796:DAUAEK>2.0.CO;2.

A. R. Jacobson, N. Gruber, J. L. Sarmiento, M. Gloor, and S. E. M. Fletcher. A joint atmosphere-ocean inversion for surface fluxes of carbon dioxide: I. methods and global-scale fluxes. *Global Biogeochemical Cycles*, 21(GB1019), 2007.

A. R. Jacobson, K. N. Schuldt, P. Tans, A. Andrews, J. B. Miller, T. Oda, S. Basu, J. Mund, B. Weir, L. Ott, T. Aalto, J. B. Abshire, K. Aikin, S. Aoki, F. Apadula, S. Arnold, B. Baier, J. Bartyzel, A. Beyersdorf, T. Biermann, S. C. Biraud, H. Boenisch, G. Brailsford, W. A. Brand, G. Chen, H. Chen, L. Chmura, S. Clark, A. Colomb, et al. CarbonTracker CT20222. Model published by NOAA Global Monitoring Laboratory, 2023. URL https://gml.noaa.gov/ccgg/carbontracker/CT2022/.

T. Kaminski, P. J. Rayner, M. Heimann, and I. G. Enting. On aggregation errors in atmospheric transport inversions. *Journal of Geophysical Research-Atmospheres*, 106(D5):4703–4715, 2001.

M. Krol, S. Houweling, B. Bregman, M. van den Broek, A. Segers, P. van Velthoven, W. Peters, F. Dentener, and P. Bergamaschi. The two-way nested global chemistry-transport zoom model TM5: algorithm and applications. *Atmospheric Chemistry and Physics*, 5:417–432, 2005. URL http://www.atmos-chem-phys.net/5/417/2005/acp-5-417-2005.html.

S. Levitus, R. A. Locarnini, T. P. Boyer, A. V. Mishonov, J. I. Antonov, H. E. Garcia, O. K. Baranova, M. M. Zweng, D. R. Johnson, and D. Seidov. World Ocean Atlas 2009. 2010.

G. Marland. Uncertainties in accounting for CO_2 from fossil fuels. *Journal of Industrial Ecology*, 12 (2):136–139, 2008. doi: 10.1111/j.1530-9290.2008.00014.x. URL https://onlinelibrary.wiley.com/doi/abs/10.1111/j.1530-9290.2008.00014.x.

M. Mu, J. Randerson, G. Van der Werf, L. Giglio, P. Kasibhatla, D. Morton, G. Collatz, R. DeFries, E. Hyer, E. Prins, et al. Daily and 3-hourly variability in global fire emissions and consequences for atmospheric model predictions of carbon monoxide. *Journal of Geophysical Research: Atmospheres*, 116(D24), 2011.

R. Nassar, L. Napier-Linton, K. R. Gurney, R. J. Andres, T. Oda, F. R. Vogel, and F. Deng. Improving the temporal and spatial distribution of CO_2 emissions from global fossil fuel emission data sets. *Journal of Geophysical Research: Atmospheres*, 118(2):917–933, 2013. doi: 10.1029/2012JD018196. URL https://agupubs.onlinelibrary.wiley.com/doi/abs/10.1029/2012JD018196.

T. Oda and S. Maksyutov. A very high-resolution (1 km x 1 km) global fossil fuel CO_2 emission inventory derived using a point source database and satellite observations of nighttime lights. *Atmospheric Chemistry and Physics*, 11(2):543–556, 2011. doi: 10.5194/acp-11-543-2011. URL https://www.atmos-chem-phys.net/11/543/2011/.

T. Oda and S. Maksyutov. ODIAC fossil fuel CO_2 emissions dataset. doi:10.17595/20170411.001, 2015.

T. Oda, S. Maksyutov, and R. J. Andres. The open-source data inventory for anthropogenic CO_2, version 2016 (ODIAC2016): a global monthly fossil fuel CO_2 gridded emissions data product for tracer transport simulations and surface flux inversions. *Earth System Science Data*, 10(1):87–107, 2018. doi: 10.5194/essd-10-87-2018. URL https://www.earth-syst-sci-data.net/10/87/2018/.

S. C. Olsen and J. T. Randerson. Differences between surface and column atmospheric CO_2 and implications for carbon cycle research. *Journal of Geophysical Research-Atmospheres*, 109(D2), 2004.

J. Olson, J. Watts, and L. Allsion. Major world ecosystem complexes ranked by carbon in live vegetation: A database. Technical Report ORNL/CDIAC-134, NDP-017, 1992. URL http://cdiac.ornl.gov/epubs/ndp/ndp017/carbonbig.html.

R. C. Pacanowski and A. Gnanadesikan. Transient response in a z-level ocean model that resolves topography with partial cells. *Monthly Weather Review*, 126:3248–3270, 1998.

P. K. Patra, S. Houweling, M. Krol, P. Bousquet, D. Belikov, D. Bergmann, H. Bian, P. Cameron-Smith, M. P. Chipperfield, K. Corbin, et al. TransCom model simulations of CH_4 and related species: linking transport, surface flux and chemical loss with CH_4 variability in the troposphere and lower stratosphere. *Atmospheric Chemistry and Physics*, 11(24):12813–12837, 2011.

W. Peters, M. C. Krol, E. J. Dlugokencky, F. J. Dentener, P. Bergamaschi, G. Dutton, P. von Velthoven, J. B. Miller, L. Bruhwiler, and P. P. Tans. Toward regional-scale modeling using the two-way nested global model TM5: Characterization of transport using SF_6. *Journal of Geophysical Research-Atmospheres*, 109(D19), 2004. D19314.

W. Peters, J. Miller, J. Whitaker, A. Denning, A. Hirsch, M. Krol, D. Zupanski, L. Bruhwiler, and P. Tans. An ensemble data assimilation system to estimate CO_2 surface fluxes from atmospheric trace gas observations. *Journal of Geophysical Research-Atmospheres*, 110:D24304, Jan 2005. doi: 10.1029/2005JD006157. D24304.

C. S. Potter, J. T. Randerson, C. B. Field, P. A. Matson, P. M. Vitousek, H. A. Mooney, and S. A. Klooster. Terrestrial ecosystem production - a process model-based on global satellite and surface data. *Global Biogeochemical Cycles*, 7(4):811–841, 1993.

L. Rasmussen. Piecewise integral splines of low degree. *Computers & Geosciences*, 17(9):1255–1263, 1991.

C. L. Sabine, R. A. Feely, N. Gruber, R. M. Key, K. Lee, J. L. Bullister, R. Wanninkhof, C. S. Wong, D. W. R. Wallace, B. Tilbrook, F. J. Millero, T. H. Peng, A. Kozyr, T. Ono, and A. F. Rios. The oceanic sink for anthropogenic CO_2. *Science*, 305(5682):367–371, 2004.

A. E. Schuh, A. R. Jacobson, S. Basu, B. Weir, D. Baker, K. Bowman, F. Chevallier, S. Crowell, K. J. Davis, F. Deng, et al. Quantifying the impact of atmospheric transport uncertainty on CO_2 surface flux estimates. *Global Biogeochemical Cycles*, 33(4):484–500, 2019.

T. Takahashi, S. C. Sutherland, C. Sweeney, A. P. N. Metzl, B. Tilbrook, N. Bates, R. Wanninkhof, R. A. Feely, C. Sabine, J. Olafsson, and Y. Nojiri. Global air-sea CO_2 flux based on climatological surface ocean pCO_2, and seasonal biological and temperature effects. *Deep-Sea Research II*, 49:1601–1622, 2002.

T. Takahashi, S. C. Sutherland, R. Wanninkhof, C. Sweeney, R. A. Feely, D. W. Chipman, B. Hales, G. Friederich, F. Chavez, C. Sabine, et al. Climatological mean and decadal change in surface ocean pCO_2, and net sea-air CO_2 flux over the global oceans. *Deep Sea Research Part II: Topical Studies in Oceanography*, 56(8-10):554–577, 2009.

K. W. Thoning, P. P. Tans, and W. D. Komhyr. Atmospheric carbon dioxide at Mauna Loa observatory. 2. Analysis of the NOAA GMCC data, 1974-1985. *Journal of Geophysical Research-Atmospheres*, 94: 8549–8565, Jan 1989.

G. van der Werf, J. Randerson, G. Collatz, and L. Giglio. Carbon emissions from fires in tropical and subtropical ecosystems. *Global Change Biology*, 9:547–562, Jan 2003.

G. R. van der Werf, J. T. Randerson, L. Giglio, G. J. Collatz, P. S. Kasibhatla, and A. F. Arellano. Interannual variability in global biomass burning emissions from 1997 to 2004. *Atmospheric Chemistry and Physics*, 6:3423–3441, Jan 2006.

G. R. van der Werf, J. T. Randerson, L. Giglio, T. T. van Leeuwen, Y. Chen, B. M. Rogers, M. Mu, M. J. E. van Marle, D. C. Morton, G. J. Collatz, R. J. Yokelson, and P. S. Kasibhatla. Global fire emissions estimates during 1997–2016. *Earth System Science Data*, 9(2):697–720, 2017. doi: 10.5194/essd-9-697-2017. URL https://www.earth-syst-sci-data.net/9/697/2017/.

R. Wanninkhof. Relationship between wind-speed and gas-exchange over the ocean. *Journal of Geophysical Research-Oceans*, 97:7373–7382, Jan 1992.

J. S. Whitaker and T. M. Hamill. Ensemble data assimilation without perturbed observations. *Monthly Weather Review*, 130(7):1913–1924, 2002.